NREL/TP-214-4453 • UC Category: 271 • DE92001197

NREL/TP--214-4453

DE92 001197

Research on Stable, High-Efficiency Amorphous Silicon Multijunction Modules

Semiannual Subcontract Report 1 January 1990 - 30 June 1991

S. Guha
United Solar Systems Corporation
Troy, Michigan

NREL technical monitor: W. Luft

National Renewable Energy Laboratory
(formerly the Solar Energy Research Institute)
1617 Cole Boulevard
Golden, Colorado 80401-3393
A Division of Midwest Research Institute
Operated for the U.S. Department of Energy
under Contract No. DE-AC02-83CH10093

Prepared under Subcontract No. ZM-1-19033-2

December 1991

On September 16, 1991, the Solar Energy Research Institute was designated a national laboratory, and its name was changed to the National Renewable Energy Laboratory.

NOTICE

Printed in the United States of America
Available from:
National Technical Information Service
U.S. Department of Commerce
5285 Port Royal Road
Springfield, VA 22161

Price: Microfiche A01
Printed Copy A05

Codes are used for pricing all publications. The code is determined by the number of pages in the publication. Information pertaining to the pricing codes can be found in the current issue of the following publications which are generally available in most libraries: *Energy Research Abstracts (ERA)*; *Government Reports Announcements* and Index (*GRA* and I); *Scientific and Technical Abstract Reports (STAR)*; and publication NTIS-PR-360 available from NTIS at the above address.

PREFACE

This Semi-Annual Technical Progress Report covers the work performed by United Solar Systems Corp. for the period 1 January 1991 to 30 June 1991 under DOE/SERI Subcontract Number ZM-1-19033-2. The following personnel participated in the research program:

A. Banerjee, E. Chen, T. Glatfelter, S. Guha (Principal Investigator), G. Hammond, M. Hopson, N. Jackett, M. Lycette, T. Palmer, A. Pawlikiewicz, I. Rosenstein, R. Ross, D. Wolf, J. Yang, and K. Younan.

We would like to thank V. Trudeau for preparation of this report.

TABLE OF CONTENTS

LIST OF FIGURES

LIST OF TABLES

EXECUTIVE SUMMARY

OBJECTIVES

The primary objective of this research program is to improve our understanding of amorphous silicon alloys and other relevant non-semiconductor materials for use in high-efficiency, large-area multijunction modules. The goal of the Phase I effort is to demonstrate by the end of 1991 a multijunction module with a stabilized efficiency of larger than 8%.

DISCUSSIONS

The program is divided into three tasks. In Task I, the focus is on improvement of materials and cell structures deposited over 900 cm^2 area. Task 2 involves the optimization of back reflectors and antireflection coatings over large area. Task 3 is directed toward fabrication of modules which involves patterning of grids, cell isolation and interconnects and module encapsulation.

In Tasks I and II, we have concentrated on deposition of a-Si alloys and same-bandgap, dual-junction cells over large area (> 900 cm^2). The optimum back reflector to obtain high short-circuit current density is ZnO/Ag. However, since our sputtering machine for deposition of ZnO/Ag over large area is not yet ready, we have used ZnO/AlSi back reflector for studying performance of 900 cm^2 panels; optimization of cells using ZnO/Ag back reflector has been carried out using 2″ x 2″ substrates. We have obtained an average initial efficiency of 8.8% over 900 cm^2 area using same-bandgap, dual-junction cells deposited on ZnO/AlSi back reflector. The averaging was done by measuring the efficiencies of 80 subcells (active area of 7.4 cm^2) deposited over the entire area. The dispersion in the value of subcell efficiency over the entire area is ± 2%, which demonstrates the uniformity of the a-Si alloy layer thicknesses and also the uniformity of the top antireflection coating. The corresponding initial efficiency on ZnO/Ag back reflector is 9.6% (active area of 0.25 cm^2). Development of multi-bandgap cells deposited over large-area ZnO/Ag substrates would be the major thrust of our program in the next few months.

Since the focus of the program is on stabilized efficiency after prolonged light exposure under one-sun condition at 50°C, we decided to investigate if we could get the same information in a much shorter time using intense illumination. Using a setup where light soaking can be done at temperatures between 25 and 225°C and at intensities between one to one hundred suns, we demonstrated that by measuring the degradation behavior at two different intensities and two different temperatures, it is possible to generate a series of curves that will give the degradation of the cell at any intensity or temperature. We used this technique to investigate the stability of single-junction cells as a function of cell thickness. When cells are deposited on ZnO/Ag back reflector, we found that the highest stabilized efficiency is obtained for cells with the intrinsic layer thickness of about 2000 Å. We also investigated the substrate temperature dependence of the stabilized cell efficiency. In the range of 250 to 350°C, both the initial and final efficiencies were found to be not very sensitive to temperature, with the maximum values obtained at around 300°C. Using our numerical model for solar cells, we find that the experimental results for the thick cells, both in the undegraded and degraded states, can be explained by assuming that the only effect of prolonged light illumination is an increase in gap state density. In order to obtain quantitative agreement with the data for cells with different thicknesses, we had to assume that the optical path (or number of reflections) increases with cell thickness. The problem is being further investigated.

We have investigated the electrical and optical losses associated with the grids and bus bars in the module. Using a sensitivity analysis of the effect of ITO sheet resistivity, grid resistivity, grid separation and the number of bus bars per square foot, we find that with our current state of technology a power loss of about 6% is achievable. Assuming an encapsulation loss of about 3 to 4%, we calculate a decrease of about 10% as we go from active-area cell efficiency to module aperture-area efficiency. Preliminary experiments showed a decrease of about 11%, which is in good agreement with our expectations. Further experiments are in progress to lower the loss.

CONCLUSION

We have achieved an average subcell initial efficiency of 8.8% over one-square-foot area using same-bandgap, dual-junction cells deposited over ZnO/AlSi back reflector. An initial efficiency of 9.6% was achieved using ZnO/Ag back reflector over smaller substrates. We are building a sputtering machine to deposit ZnO/Ag back reflector over one-square-foot area so that higher efficiency can be obtained on larger substrates as well.

Calculations have been done to optimize the grid pattern, bus bars and cell interconnects on modules. With our present state of technology, we expect a difference of about 6% between aperture-area and active-area efficiency of modules. Preliminary experiments show a difference of about 8%.

We have established a procedure by which we can predict the performance of single-junction cells after long-term light exposure at 50°C by exposing cells to short-term intense light at different temperatures. We find that single-junction cells deposited on ZnO/Ag back reflector show the highest stabilized efficiency when the thickness of the intrinsic layers is about 2000 Å.

SECTION 1
INTRODUCTION

The research program is directed toward advancing our understanding of amorphous silicon alloys and other relevant non-semiconductor materials for use in large-area multijunction modules. An important thrust of the program is on performance of modules after long-time light exposure; therefore, study of light-induced degradation therefore forms an important part of the program. The final goal of the program is to demonstrate a stable, aperture-area efficiency of 12% for a two-terminal, multi-bandgap, multijunction module of aperture area of at least 900 cm^2.

The program is divided into three tasks. Task 1, semiconductor materials research, is directed toward depositing, optimizing, and characterizing of suitable amorphous silicon alloy materials and cell structures over 900 cm^2 area. Task 2, non-semiconductor materials research, involves investigating suitable back reflectors and antireflection coatings and also encapsulants for the modules. Task 3, module research, is directed toward fabricating modules involving grid patterning, cell isolation and interconnect, and encapsulation.

In this report, we outline the progress made toward the program goal in the different task areas. In Section 2, we discuss the experimental results on characteristics of a-Si alloy cells using a large-area deposition chamber. Results on back reflectors and antireflection coatings are also discussed. Same-bandgap dual-junction subcells with active area of 7.4 cm^2 have shown an average initial efficiency of 8.8% over 1 sq. ft. area. These cells were made using ZnO/Al-Si back reflector. Small-area (0.25 cm^2) subcell initial efficiency of 9.6% has been achieved using ZnO/Ag back reflector. In Section 3, the module design procedure is outlined. The losses associated with grid lines, cell isolation, and encapsulation are evaluated and optimized. With our current grid design and encapsulation procedure, the difference between active-area subcell efficiency and module aperture-area efficiency is about 10%. In Section 4, we discuss accelerated light-soaking results in cells. A new method has been developed to obtain cell performance after prolonged one-sun light soaking using high-intensity short-time illumination at different temperatures. Finally, in Section 5, we discuss our numerical simulation results to explain the performance of cells of different thicknesses after intense light exposure.

SECTION 2
LARGE-AREA SEMICONDUCTOR AND NON-SEMICONDUCTOR DEPOSITION

2.1 Selection of Feedstock Materials

During the period under review, the emphasis has been toward the optimization of single-junction and dual-junction a-Si:H alloy cells using a large-area batch deposition system. The dual-junction configuration employs similar bandgap a-Si:H i-layers for both the top and bottom cells. We shall begin work on triple-junction cells and dual-junction cells using narrow bandgap a-Si:Ge:H *i* layers in the next part of the project. Thus all results presented in this report have been obtained on ~ 1.75-1.8 eV bandgap materials. The schematic of a dual-junction cell structure is shown in Fig. 1. All the semiconductor layers have been deposited in the IIB machine (described below) by the conventional rf glow-discharge method. We have used microcrystalline *p* layers in order to obtain both higher V_{oc} and higher blue response.

The structural, electrical, and optical properties of the semiconductor layers have been measured before the commencement of the present subcontract. We reported these results[1] in an earlier SERI subcontract, No. ZB-7-06003-4. No significant changes have been made in the recent past.

The feedstock materials (gases) selected for depositing the films in the IIB machine are the same as those used in an earlier SERI subcontract. The gases are silane, disilane, hydrogen, and silicon tetrafluoride for the intrinsic layers. Phosphine and boron trifluoride are used for the doped layers. Germane will be used for the a-Si:Ge:H narrow-bandgap intrinsic layers. The relevant information regarding the feedstock gases, including purity, are given in Table I.

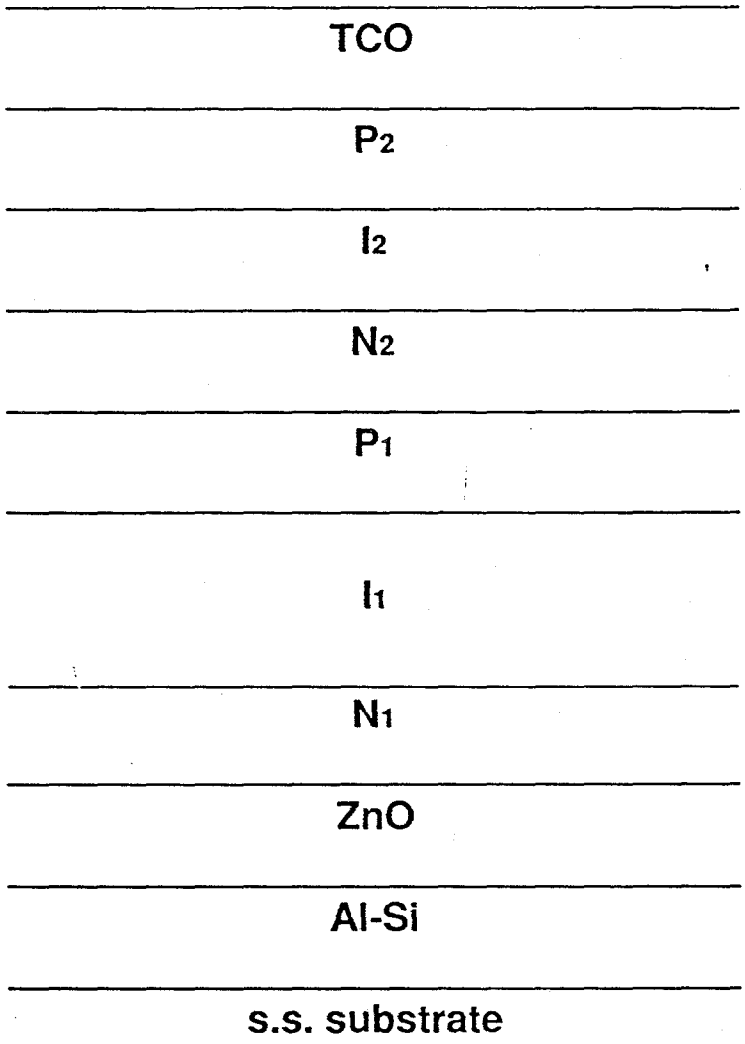

Fig. 1. Schematic of dual-junction cell structure.

Table I. Impurity content in the process gases.

GAS	IMPURITY (ppm)			
	O_2	N_2	CO/CO_2	H_2O
Silane	< 1	< 5	< 2	< 1
Disilane	< 1	< 5	< 2	-
Germane	< 1	< 2	< 2	-
Silicon Tetrafluoride	< 4	< 4	< 2	-
Phosphine	< 1	< 1	< 2	< 1
Boron Trifluoride			99.5% pure	

2.2 Large-Area Deposition System

We have been using a multichamber system (IIB) with gate valves isolating the different chambers dedicated for the deposition of *p, i,* and *n* layers for the large-area cell research. The system is computer-controlled and has the capability of handling 1 sq. ft. stainless steel substrates. Although the system has been operational for several years, it was shifted only recently to the present location of USSC, and significant changes in the plumbing of vacuum and gas lines have been made.

In view of the above, we have evaluated the quality and uniformity of individual layers by measuring the actual device performance over an area of 1 sq. ft. Two types of substrate sizes and corresponding substrate holders have been used for this purpose. One incorporates a large frame that yields 1 sq. ft. area devices. The second type uses a substrate holder that holds six 2″ x 2″ substrates, the positions of which are dispersed over an area of 1 sq. ft. along both dimensions. The second configuration has allowed us to deposit cells on back reflectors such as ZnO/Ag, which can presently be prepared only on small-area (2″ x 2″) substrates. Also, the small-area work on single-junction *n-i-p* cells helps to optimize parameters to be used for dual-junction cells on large substrates. In this report, the individual cell area for the small-area substrates is 0.25 cm^2.

2.3 a-Si:H Single-junction and Dual-junction Results

The highest initial single-junction cell efficiency obtained on a small-area substrate for a ZnO/Al-Si back reflector is 8.8%. The J-V characteristics are shown in Fig. 2. The cell area is 0.25 cm^2. From the quantum efficiency Q versus wavelength curve (shown in Fig. 3), the calculated J_{sc} is 15.14 mA/cm^2. The initial efficiency of 8.8% has been arrived at using the corrected value of J_{sc} obtained from the Q measurement. We should mention that unless the active area is measured with great precision, there could be some uncertainty in the measured value of J_{sc}. Measurement of J_{sc} from Q measurement is independent of cell area and is therefore more reliable.

We have fabricated dual-junction cells on small-area ZnO/Al-Si back reflectors. The J-V characteristics and Q curve of such a cell are shown in Figs. 4 and 5, respectively. The initial efficiency of the dual-junction cell is 9.4%. The current density contributions from the top and bottom cells are 7.48 mA/cm^2 and 7.39 mA/cm^2, respectively, and therefore the structure is bottom-cell limited. For optimum performance, the dual-junction cell should be top-cell limited. Thus further optimization is necessary.

We should point out that the open-circuit voltage (V_{oc}) of a single-junction cell depends on cell thickness, and thinner cells have higher V_{oc}. Thus, even though the V_{oc} for single-junction cell in Fig. 2 is 0.897 V, that for the top cell of the dual-junction cell is higher. This accounts for the observed V_{oc} of 1.797 V that is reported for the dual-junction cell in Fig. 4.

Single-junction cells and dual-junction cells have been fabricated on small-area ZnO/Ag back reflector substrates. The J-V characteristics and Q curve of a single-junction cell are shown in Figs. 6 and 7, respectively. Using the value of J_{sc} = 16.62 mA/cm^2 obtained from the Q curve, the corrected initial cell efficiency is 9.5%. Comparing the value of J_{sc} obtained from the Q curves shown in Figs. 3 and 7, we find that the use of ZnO/Ag back reflector results in an enhancement of approximately 1-1.5 mA/cm^2 in the value of J_{sc}. The J-V characteristics and Q curve of a dual-junction cell on a small-area ZnO/Ag substrate are shown in Figs. 8 and 9, respectively. The initial efficiency of the device is 9.6%. We have not yet made any optimization in cell deposition parameters for the dual-junction cell.

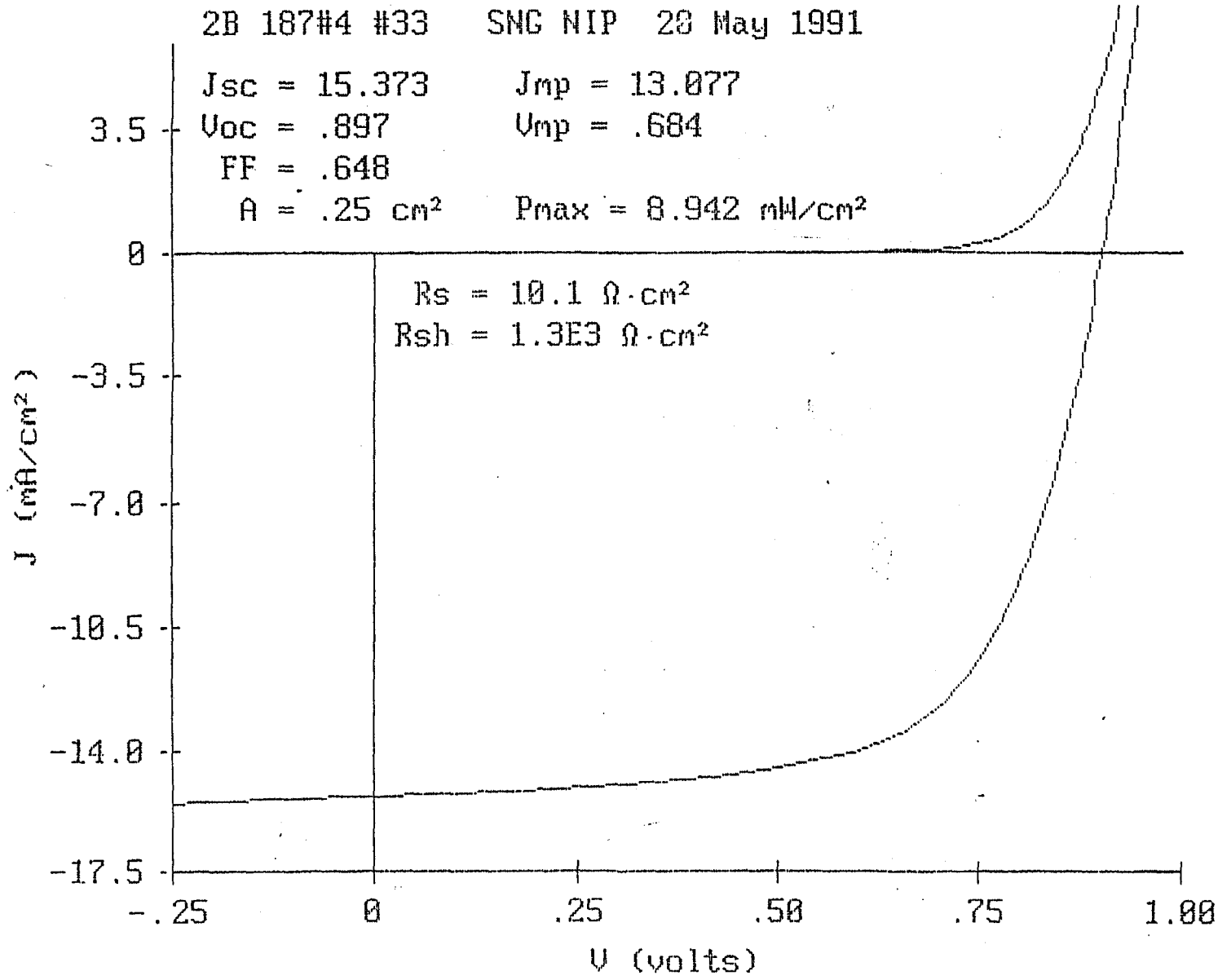

Fig. 2. J-V characteristics of single-junction cell on small-area ZnO/Al-Si back reflector.

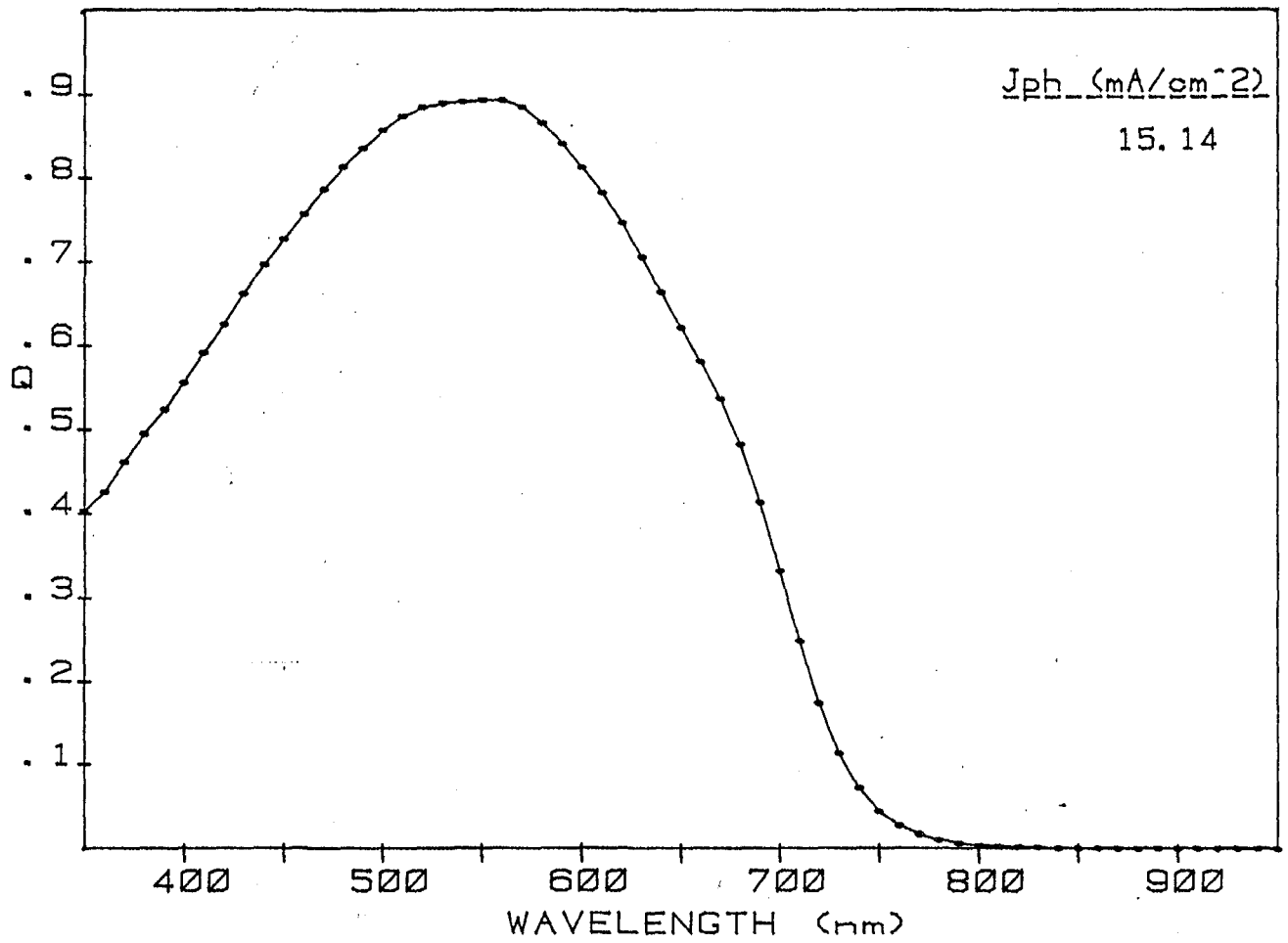

Fig. 3. Q curve of single-junction cell on small-area ZnO/Al-Si back reflector.

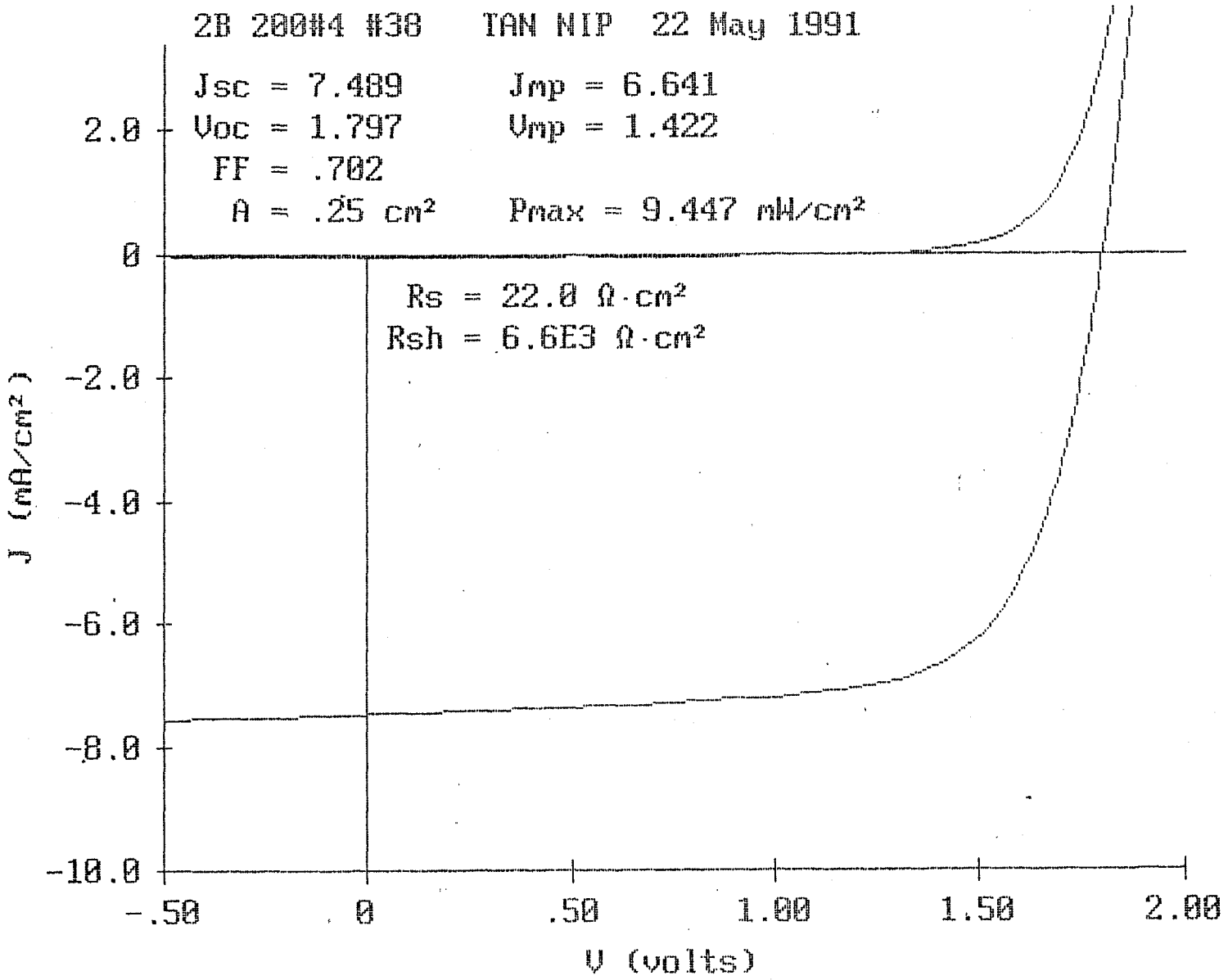

Fig. 4. J-V characteristics of dual-junction cell on small-area ZnO/Al-Si back reflector.

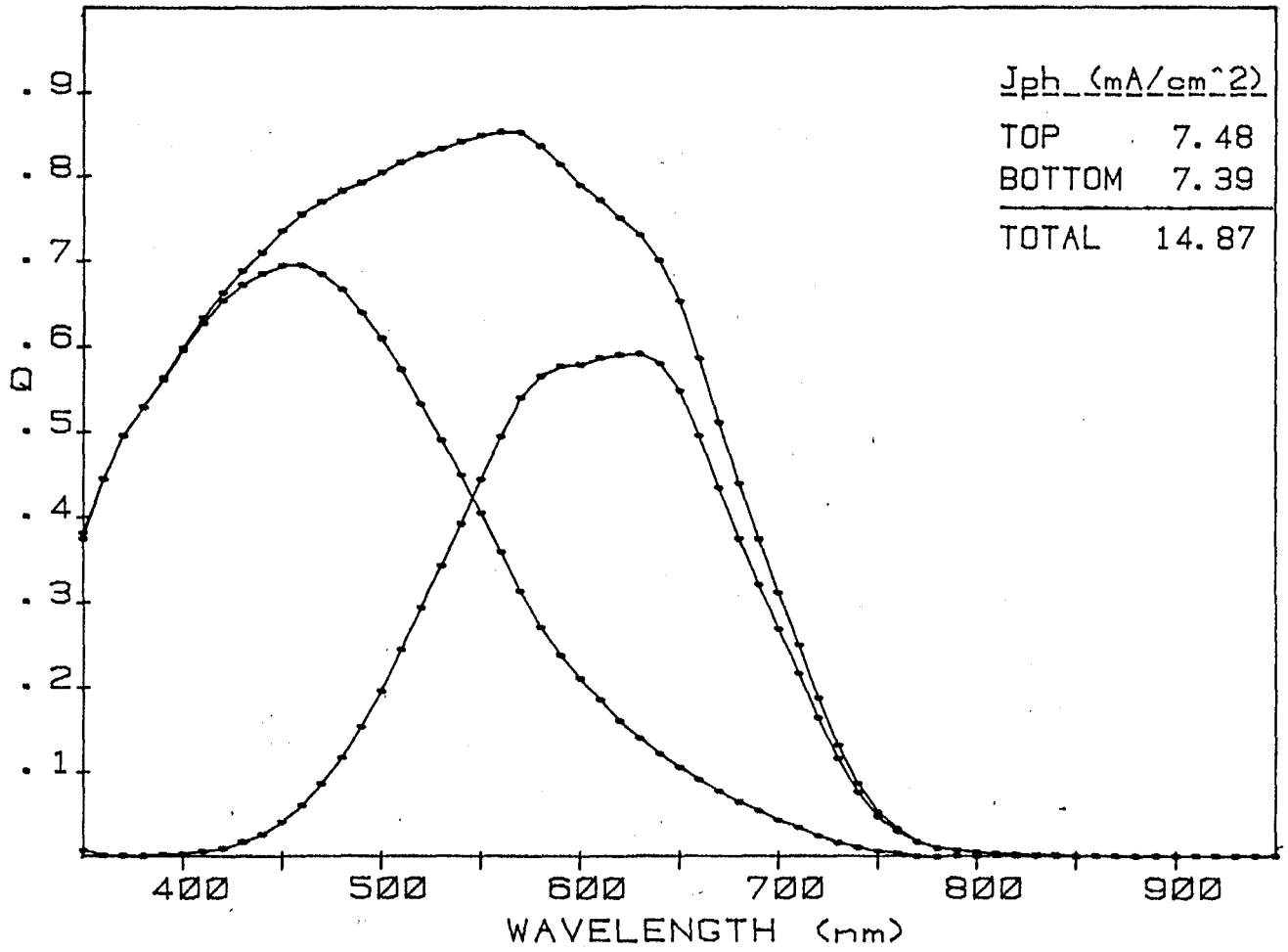

Fig. 5. Q curve of dual-junction cell on small-area ZnO/Al-Si back reflector.

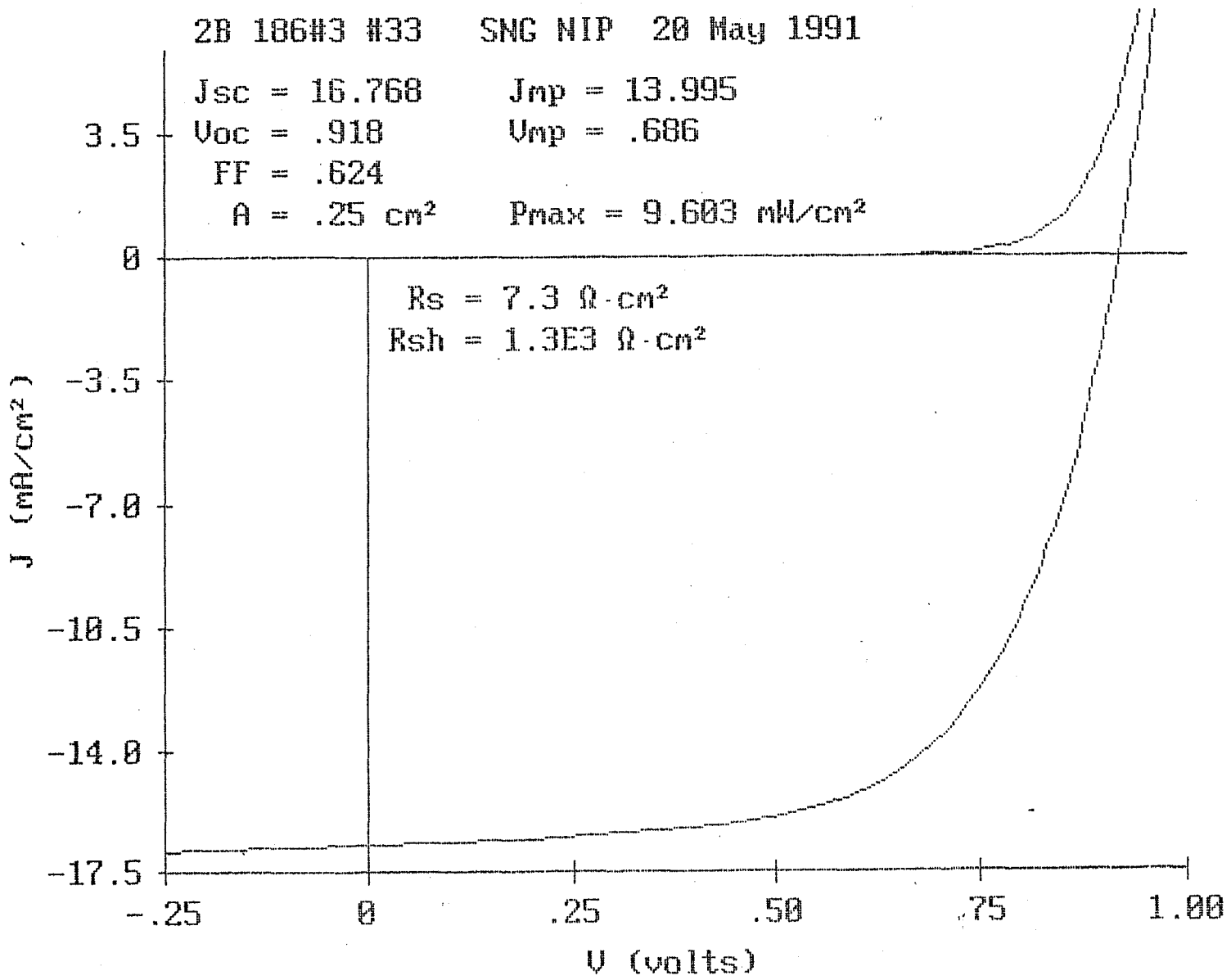

Fig. 6. J-V characteristics of single-junction cell on small-area ZnO/Ag back reflector.

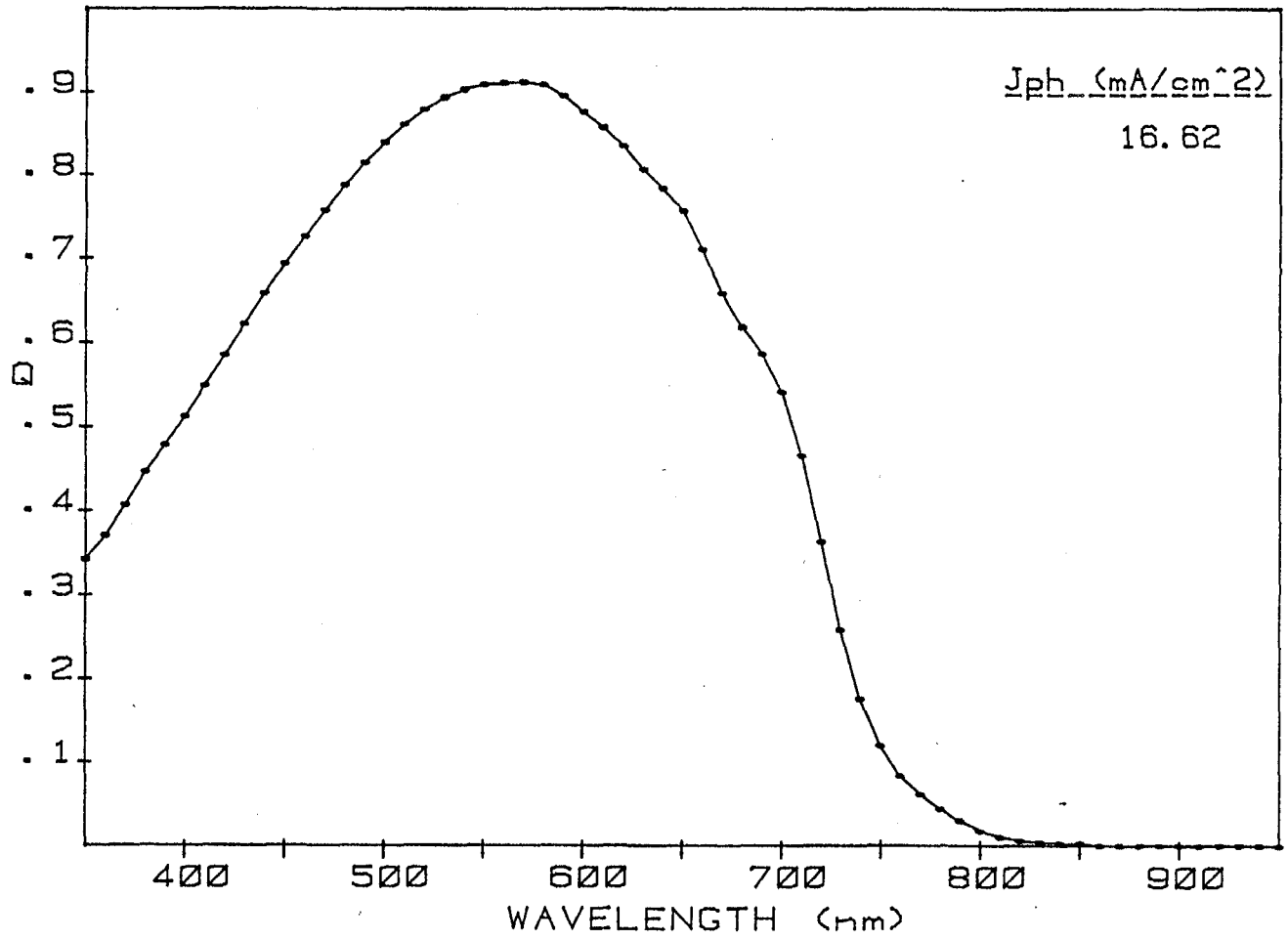

Fig. 7. Q curve of single-junction cell on small-area ZnO/Ag back reflector.

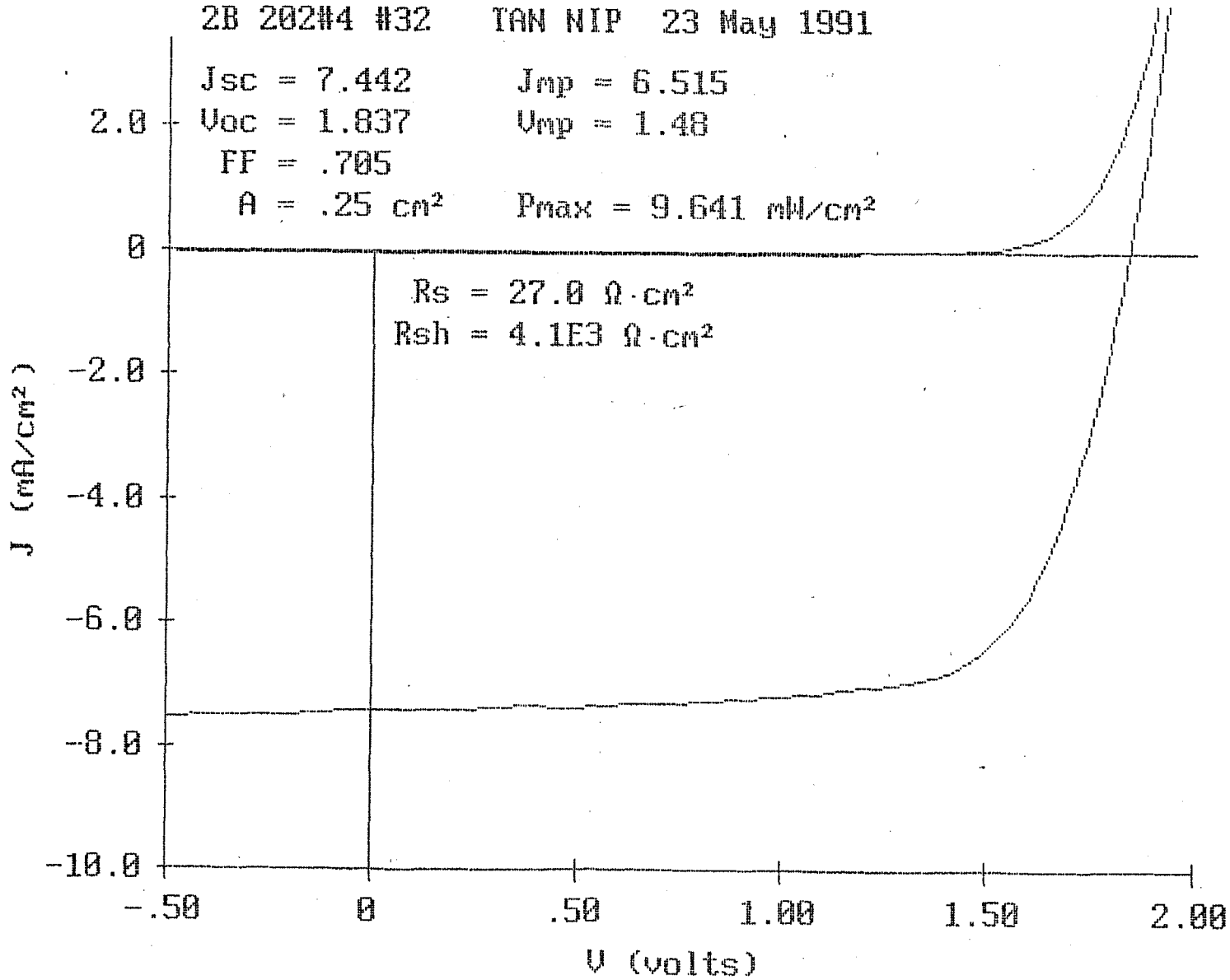

Fig. 8. J-V characteristics of dual-junction cell on small-area ZnO/Ag back reflector.

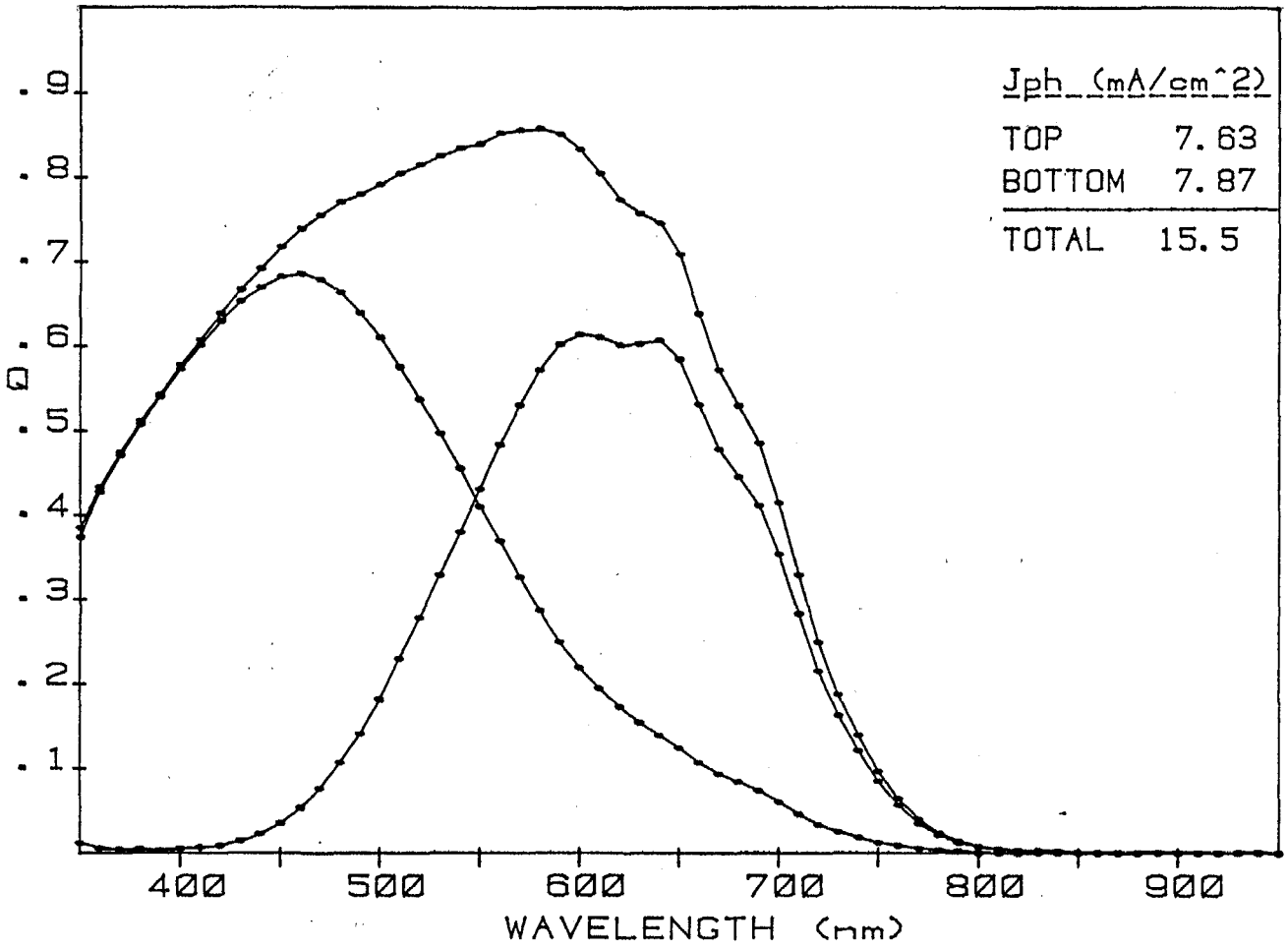

Fig. 9. Q curve of dual-junction cell on small-area ZnO/Ag back reflector.

The results of a same bandgap dual-junction cell initial efficiency and its uniformity and yield over an area of 1 sq. ft. are shown in Fig. 10. The data have been obtained on 80 individually scribed cells, each of area 7.36 cm^2 and spread over an array of 16 x 5. The criterion used to measure the yield is fill factor, FF $\geq$ 0.45. This criterion was chosen to determine the occurrence of shorts and shunts in large-area cells. As shown in the figure, the yield is 100%. The values of V_{oc}, J_{sc}, FF, and initial efficiency averaged over all the 80 cells covering the 1 sq. ft. area are 1.81 V, 7.2 mA/cm^2, 0.68, and 8.8%, respectively. The average initial efficiency of the 10 best cells is 9.1%. Thus, comparing the average values of efficiency for the 10 best cells and all the 80 cells, the uniformity in cell performance over an area of 1 sq. ft. is presently within ~ 3-4%. The *Q* curve for one cell located near the center of the 1 sq. ft. substrate is shown in Fig. 11. The total current density (sum of the J_{sc} of the top and bottom cell) is 15.34 mA/cm^2. The J_{sc} of the top and bottom cells are 8.17 and 7.17 mA/cm^2, respectively. Since the structure is bottom-cell limited, optimization of the thicknesses of the *i* layers of the top and bottom cells should lead to higher efficiency.

2.4 Non-Semiconductor Materials and Deposition

We have used stainless steel substrates for all the work. The back reflector material used for the 1 sq. ft. devices is ZnO/Al-Si, which was deposited using our production roll-to-roll machine. The superior back reflector ZnO/Ag has been used only for the small-area work because we have presently no machine to deposit the same over larger areas. A system to prepare ZnO/Ag back reflector over an area of > 1 sq. ft. by sputtering technique is under construction and should be ready soon. After initial qualification tests, only ZnO/Ag back reflectors will be used for the remainder of the project.

We have prepared the ZnO/Al-Si back reflector by an all-sputtering process. Typical deposition parameters for the ZnO and Al-Si films are pressure ~ 1-10 Torr and substrate temperature ~ 300-400°C. The deposition rate of the ZnO film is ~ 30 Å/s. The top transparent conducting contact (Indium Tin Oxide) has been prepared by reactive evaporation. The substrate temperature is ~ 175-225°C. The thin ITO layer also acts as the

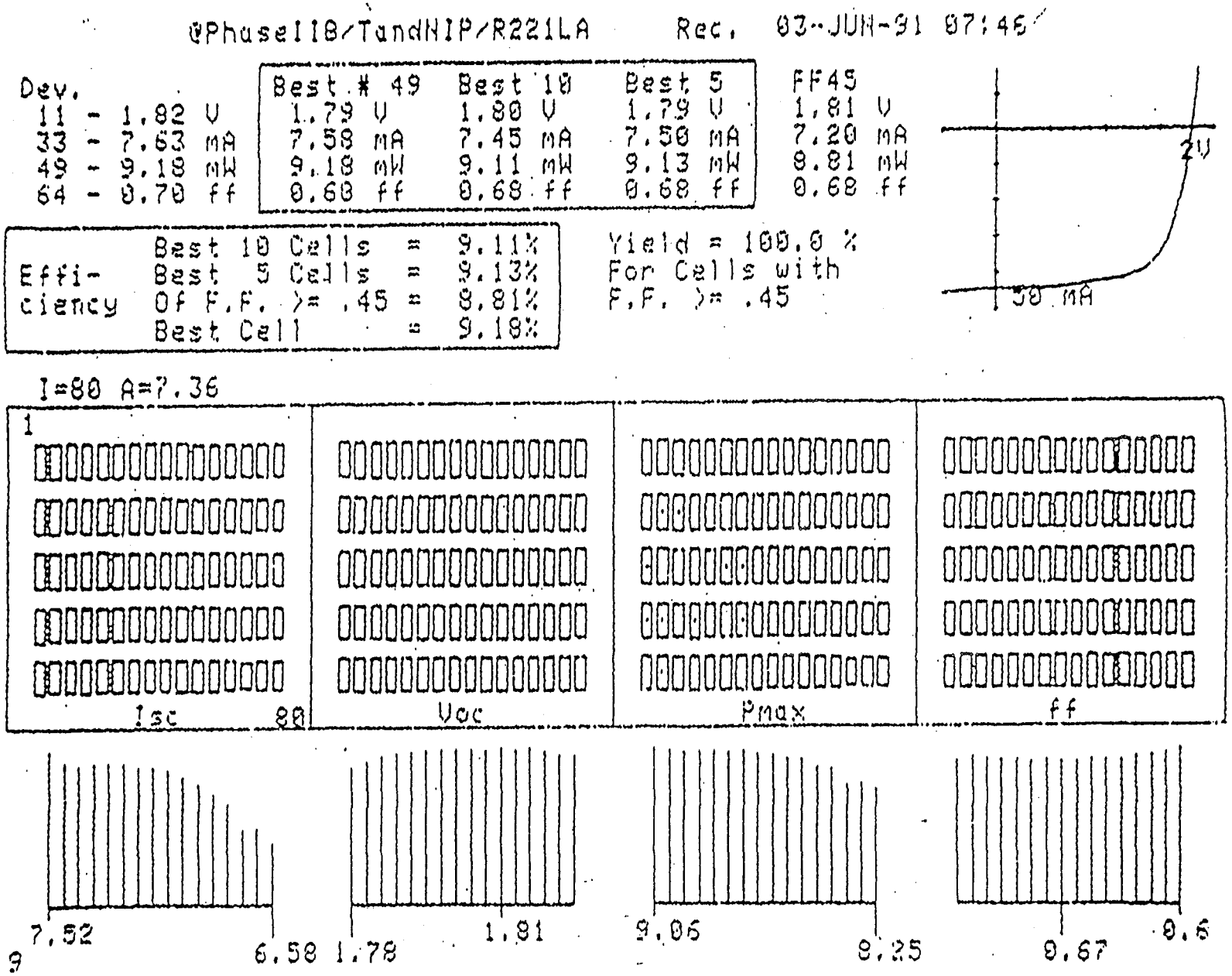

Fig. 10. Data on large-area dual junction cell panel on ZnO/Al-Si Back reflector.

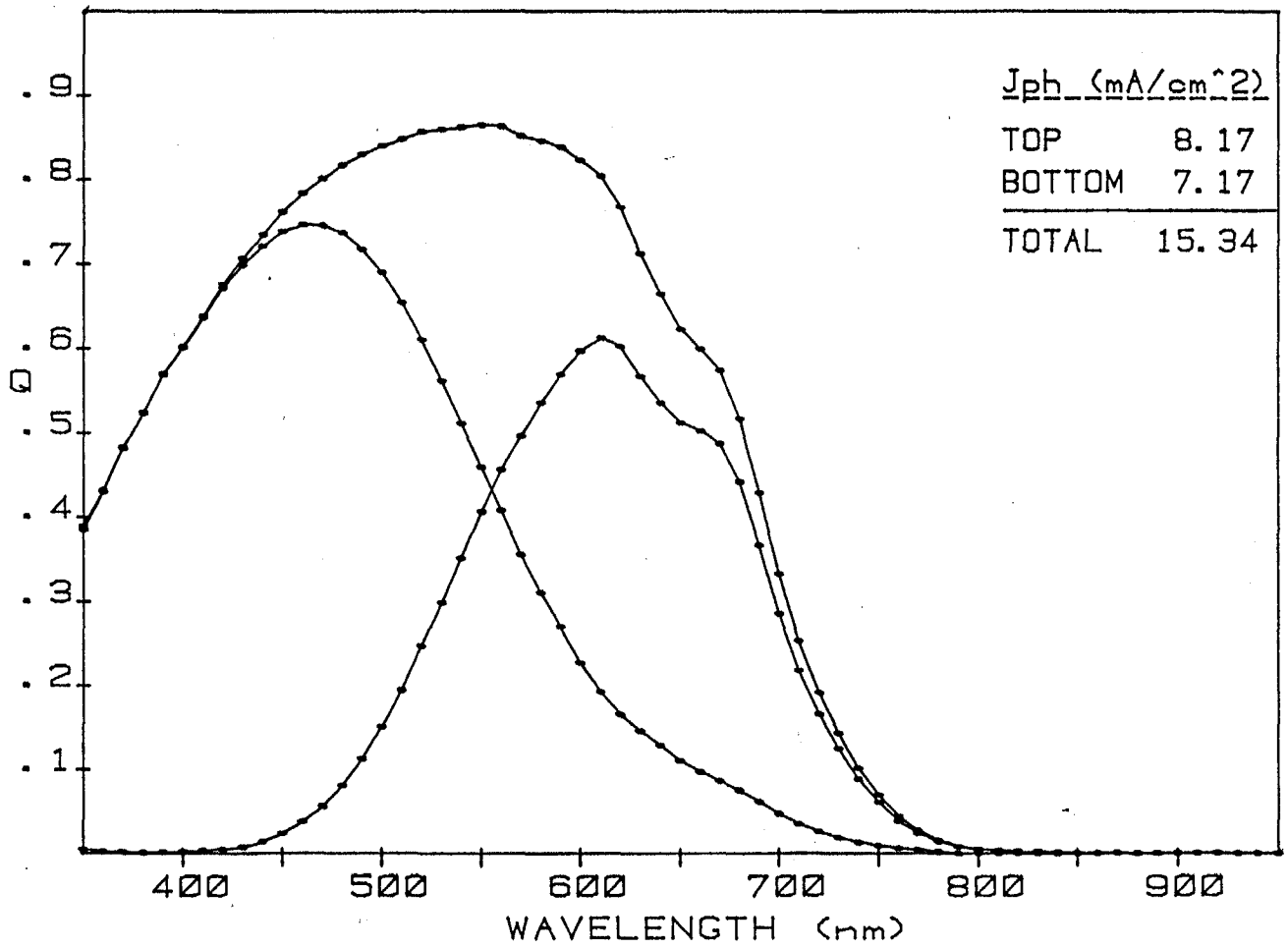

Fig. 11. Q curve of the large-area dual-junction cell panel on ZnO/Al-Si back reflector.

antireflection coating. The optical absorption of this layer is < 2%, and the sheet resistance is ~ 75-100 ohm/square. The uniformity of the combined back reflector, semiconductor layers, and TCO coating over a 1 sq. ft. area can be evaluated from the 1 sq. ft. device performance shown in Fig. 10, where we find that the difference between the best device efficiency and the average efficiency is less than 4%.

The replacement of the ZnO/Al-Si back reflector with the ZnO/Ag one is expected[2] to produce enhanced optical performance by virtue of the superior optical reflectance of Ag over Al-Si. The optical reflectance of a textured Ag and textured Al-Si surface is shown in Fig. 12. The value of reflectance is calibrated with respect to specular Al film as 100%. Our past experience on small-area single-junction cells has shown that the ZnO/Ag back reflector produces a J_{sc} that is ~ 1.0-1.5 mA/cm^2 more than the corresponding value obtained from a ZnO/Al-Si back reflector. This enhancement in J_{sc} should correspond to a 5-10% improvement in the efficiency of the 1 sq. ft. devices.

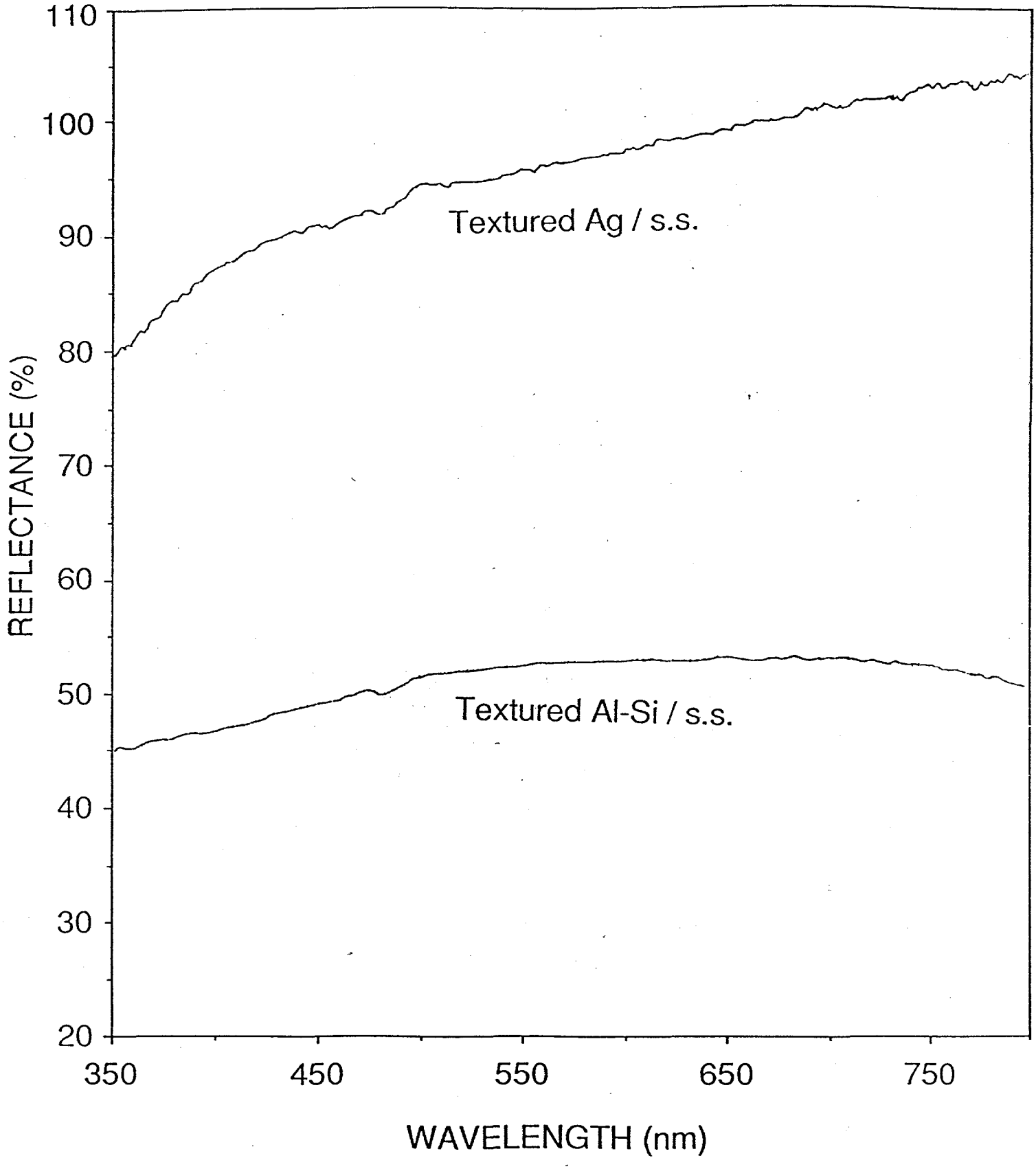

Fig. 12. Optical reflectance of a textured Ag and textured Al-Si surface on a stainless steel substrate.

SECTION 3
MODULE DESIGN AND CHARACTERIZATION

3.1 Grid Design Calculations

The first step in the module design was to develop a model to calculate the optimal grid coverage for either a series-connected or monolithic-type module. This model solves for a minimum in the power loss equation. This equation is comprised of two terms. The first term involves the addition of all shadowing losses. These are the finger loss, bus loss, etch-line loss, and bus-to-finger connector loss. The second term involves the functional dependencies of all the electrical losses. The total electrical loss will depend primarily on six variables. These variables are the length and width of the grid fingers, the distance from the tip of each finger to the etch line, the distance between fingers, and the conductivity of the ITO and metalization. This may be seen schematically in Fig. 13.

To find an exact solution to this problem for a module by some numerical method was not achieved. The approach we did choose was to find an exact solution to a unit cell that has all the relevant variables associated with it as seen in Fig. 13. The maximum area that could be solved readily is about 10 cm^2. The exact method used to solve this smaller area problem (< 10 cm^2) has been described in a previous SERI subcontractor's semiannual report.[3] Briefly, this program calculates potential profiles across the device by dividing the device in small mathematical elements. These elements may be either ITO elements or grid elements at any position depending on the geometry of the device. Each element mathematically becomes a single-node equation. The program then alters the operating voltages in order to minimize the residual currents in each node. Once the residual currents of each element become sufficiently small, we may calculate the power output and evaluate the electrical loss of this geometry.

We varied each parameter (L_{grid}, L_{edge}, W_{grid}, W_{ito}, P_{grid}, P_{ito}) independently to evaluate the effect a change in that parameter had on the unit cell power output. What we were then left with was the unit cell power loss versus these six independent variables.

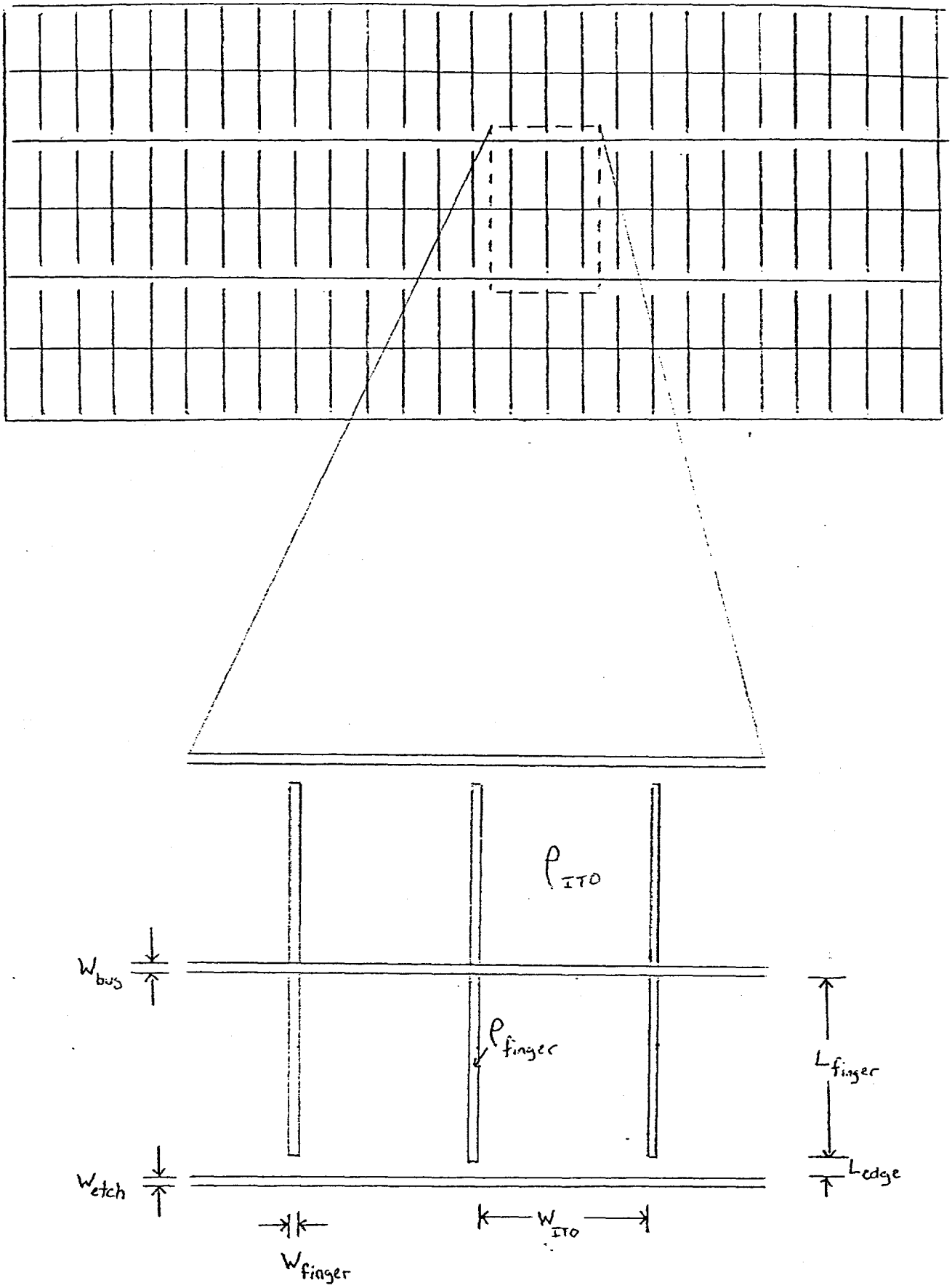

Fig. 13. Schematic of the unit cell and the associated variables used in the grid design optimization.

3.2 Loss Analysis

The next step was to empirically find the functional form in which these parameters described the power loss. Several functional forms were tested using an error minimization routine that matched the losses that were calculated using the empirical formula with those calculated from the exact solution. The functional form that matched best was the product of power law functions of each parameter such as $m_1 x^{\gamma}$ where γ_1 is the power for parameter one (e.g., L_{grid}), m_1 is the coefficient for parameter one, and x is the actual distance in cm. The reason for this approach was that the exact solution for each unit cell requires several hours to calculate and the functional form milliseconds. We may therefore try many more cases using this method.

Once we have obtained all the coefficients and powers for each parameter, we plug this formulation in for the electrical losses and add the shadowing losses. These losses are then minimized using an error minimization routine to find the physical dimensions of the module. We have assumed that parameters such as interstrip etch thickness and bus bar widths are fixed by present technology and total module dimensions by definition.

In Fig. 14 we show a plot of the total power loss, shadowing plus electrical, for a 1 ft^2 monolithic module versus the number of bus bars and the finger spacing. The ITO and grid resistance in this case were 250 ohm and 0.02 ohm, respectively. The minimum total power loss was 7.6% using 8 bus bars and 0.84 cm finger spacing. The two components of loss (shadowing and electrical) for this module case are broken down in Figs. 15 and 16. Note from Fig. 15 that the shadow loss rises quickly as the finger spacing is reduced, and the shadow loss rises slowly with an increase in the number of bus bars. In Fig. 16 we have the opposite trends, i.e., the electrical loss increases with increasing finger spacing and decreased number of bus bars. At the minimum in total loss, the shadow loss comprises approximately 2/3 of the total and the electrical loss 1/3.

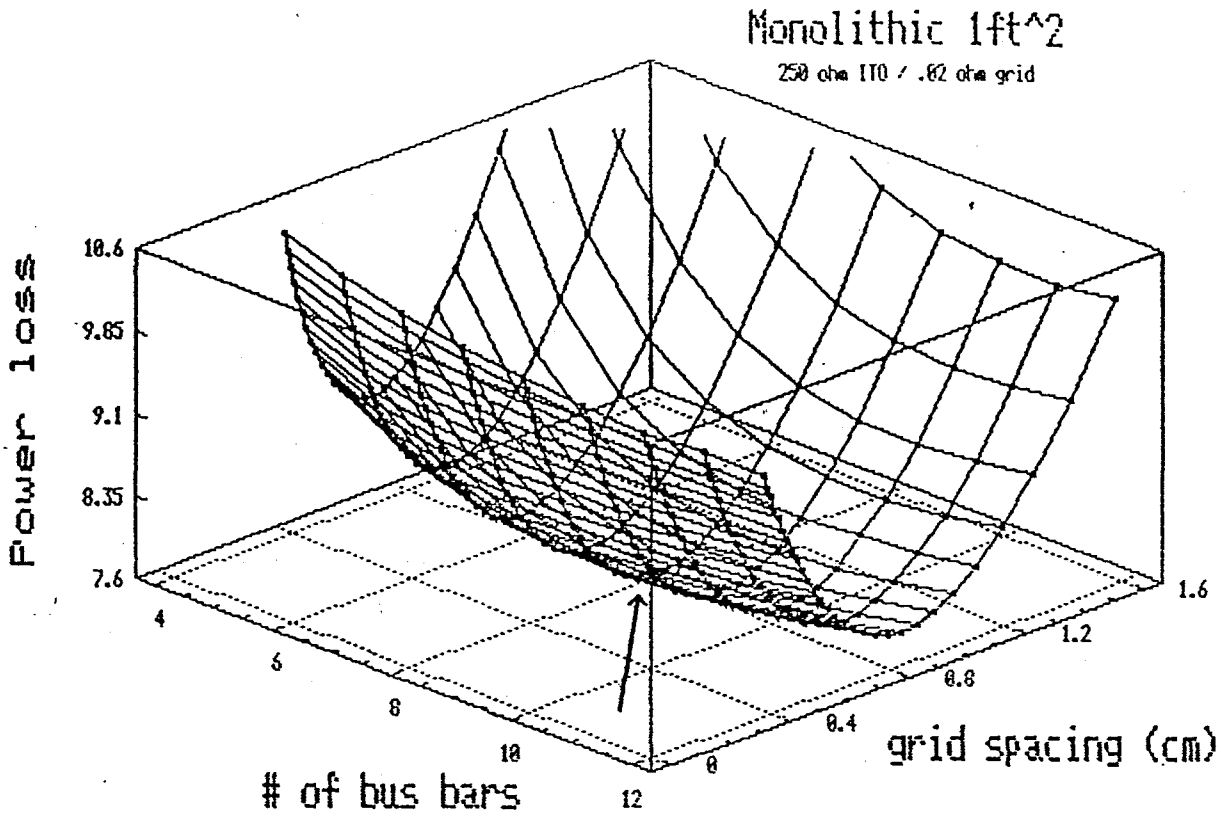

Fig. 14. Total power loss, electrical plus shadowing, for a 1 ft^2 monolithic-type module versus number of bus bars and finger spacing. The minimum value of power loss was found to be 7.6% using 8 bus bars and 0.84 cm spacing.

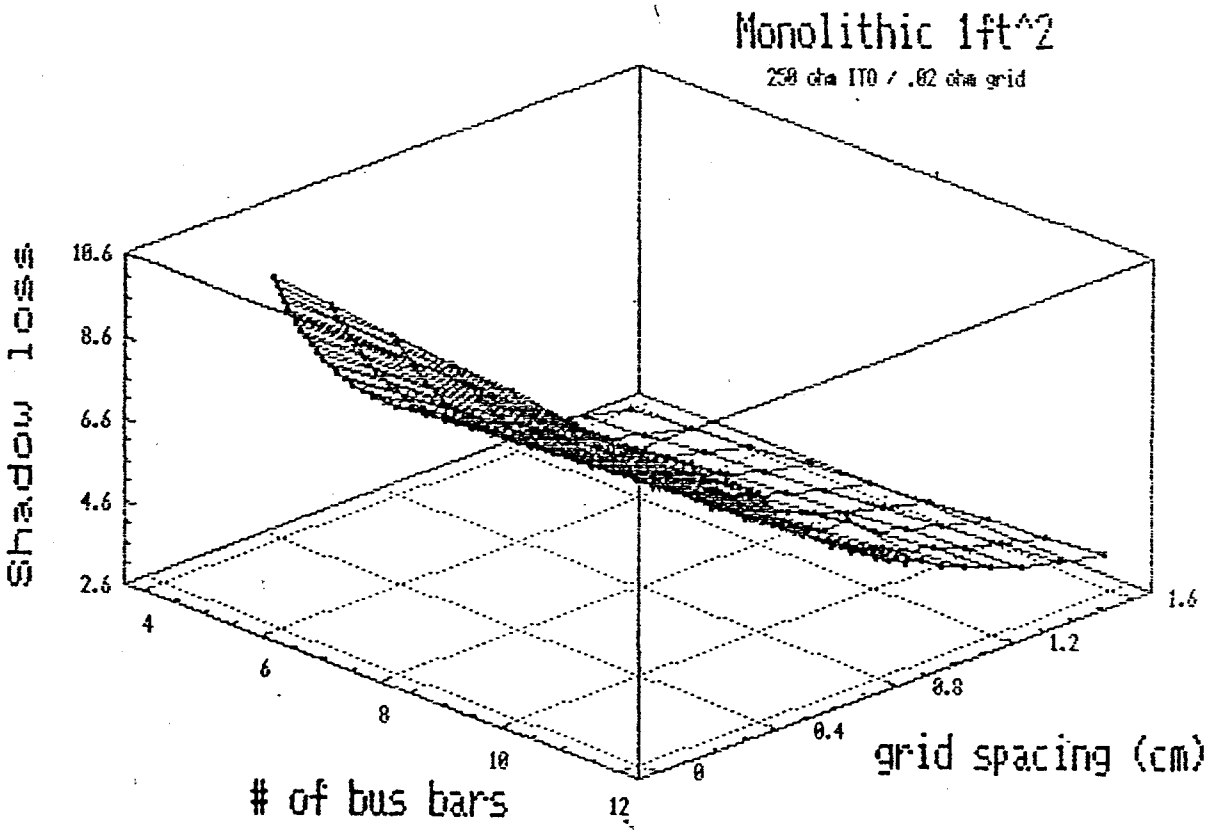

Fig. 15. Shadow loss component of the total power loss function in Fig. 14.

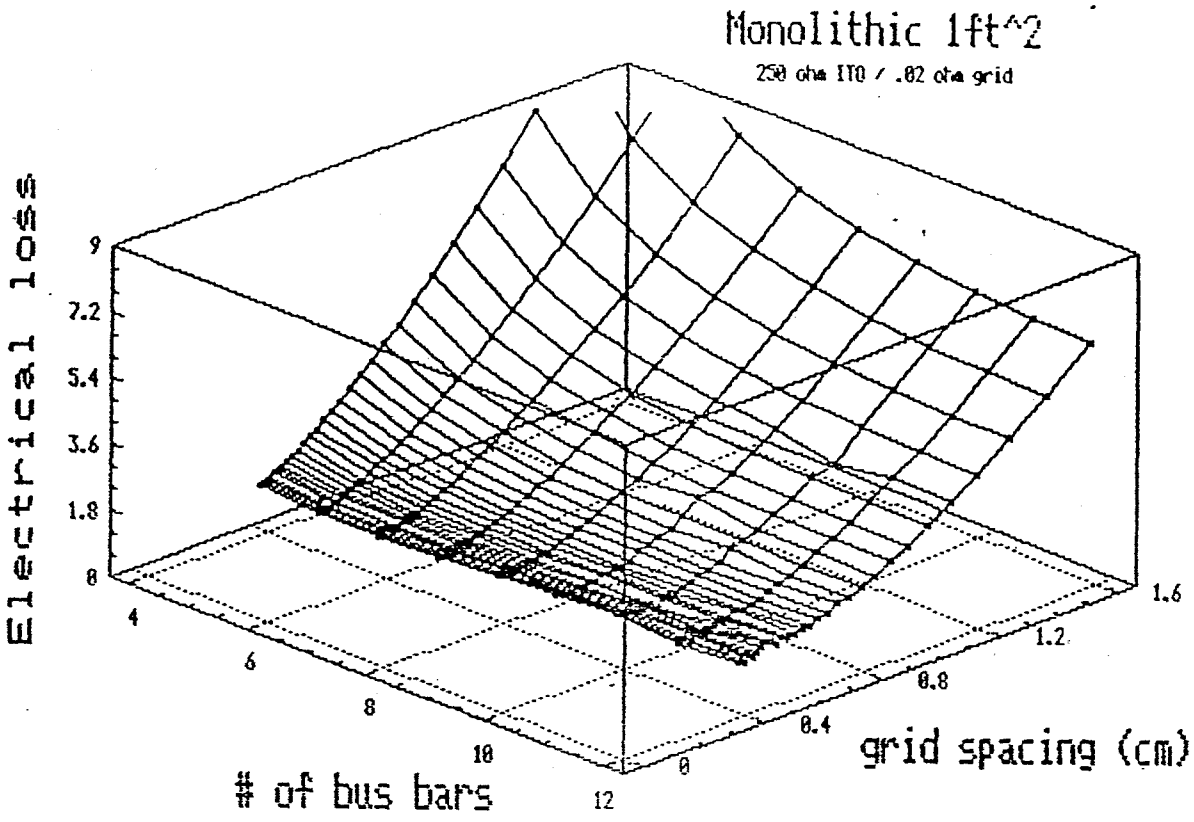

Fig. 16. Electrical loss component of the total loss power function in Fig. 14.

A summary of power loss minimum for the two module cases, monolithic and series connected, for several values of ITO and grid sheet resistance are tabulated in Table II. There are several points of interest in this table. First, there is about a 1% power loss difference between the two types of modules for one value of ITO and grid resistance due to the strip interconnect distance in the series-connected module. There is also an approximately 0.5% difference in power loss for every 50 ohm reduction in ITO resistance. There was a relationship assumed between grid resistance and grid width. The grid width for a grid resistance of 0.02 ohm was about 0.35 mm, while the grid width for a 0.2 ohm grid resistance was about 0.15 mm. It was decided that the current state of technology would dictate an ITO resistance of 100 ohm and a grid resistance of 0.028 ohm and 0.25 mm grid width. This module will give a total power loss of 6.6% for the series-connected case and 5.7% for the monolithic case.

Table II. Summary of power loss minimum for the monolithic-type and series-connected module.

Resistances (ohm per square)		Power Loss (%)	
		Series Connected	Monolithic
ITO	Grid		
50	0.02	6.4	5.5
50	0.2	5.3	4.5
100	0.02	7.3	6.3
150	0.02	7.9	6.8
250	0.02	8.7	7.6
250	0.2	7.2	6.3
100	0.028	6.6	5.7

3.3 Encapsulation

Specifications for a superstrate encapsulant structure are extremely demanding. All these materials must have very high transmission throughout the visible spectrum, be extremely ultraviolet resistant, have low water-permeability coefficients, and must be resistant to embrittlement and cracking for at least a twenty-year period. They must also have good adhesion properties, under extreme temperature and humidity conditions, to the underlying solar cell as well as to the other materials in the stack. They must be economical, easy to apply into large, uniform areas, and provide good coverage over all surface irregularities.

To meet these requirements, we use a multilayer structure of EVA and Tefzel. The EVA has high transmission, excellent adhesion properties, as well as being economically viable. The Tefzel, along with high transmission properties, has one of the lowest water permeability coefficients of any plastic and excellent ultraviolet protection for all the underlying layers.

These layers are applied onto the solar cell by laying them flat to the surface and curing under vacuum to remove any air trapped between layers. The curing temperatures that provide maximum properties are between 130 and 160°C.

Figure 17 shows the quantum efficiency of a cell before and after encapsulation. It can be seen that most of the difference is in the deep blue due to absorption and in the central region due to an increase in reflection resulting from the encapsulant altering the antireflection properties of the AR coating. Figure 18 shows the quantum efficiency of the cells shown in Fig. 17, normalized by their reflection. The difference in the two curves is approximately equal to the spectral absorption of the encapsulation materials.

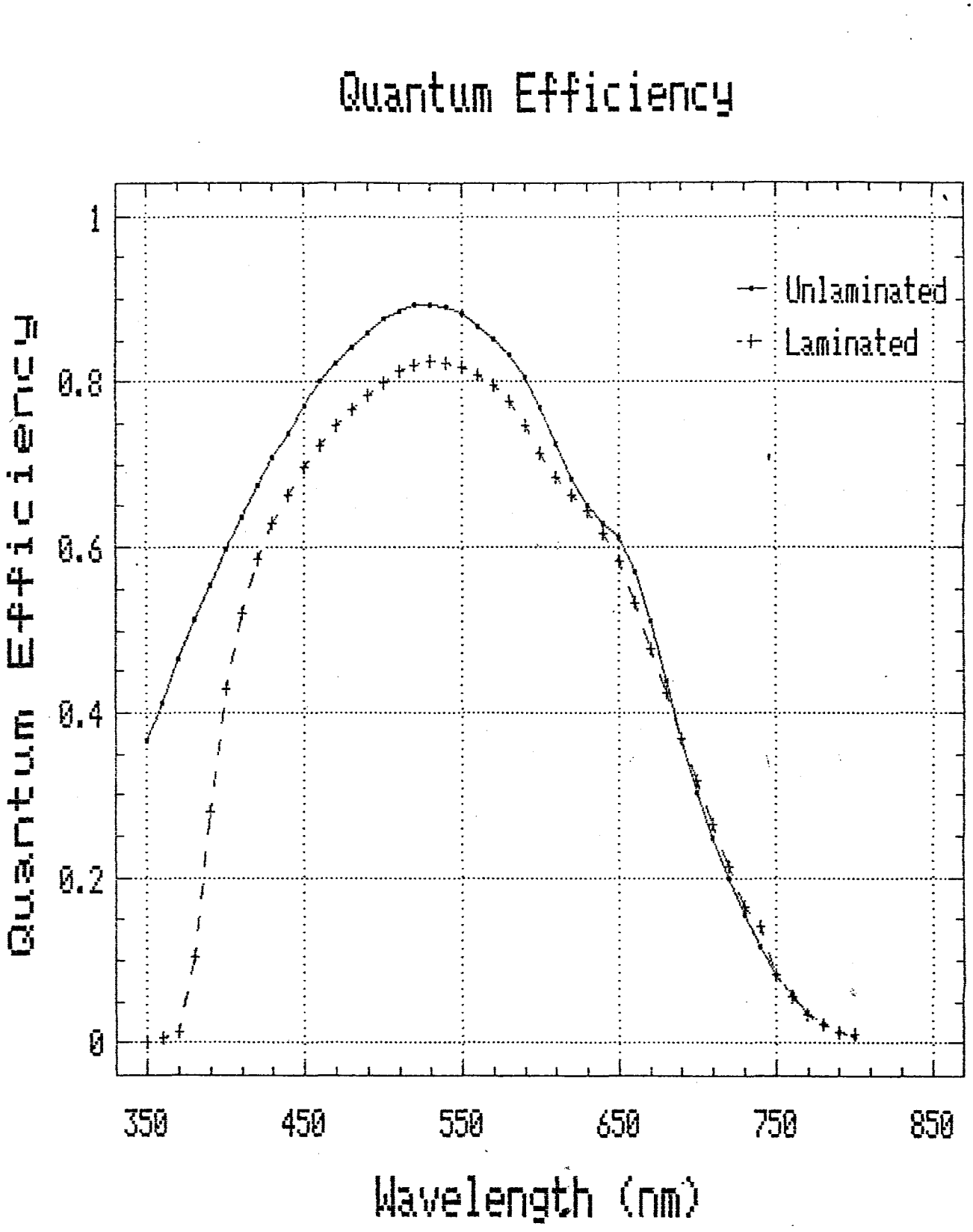

Fig. 17. Quantum efficiency of a single-junction a-Si:H device before and after lamination.

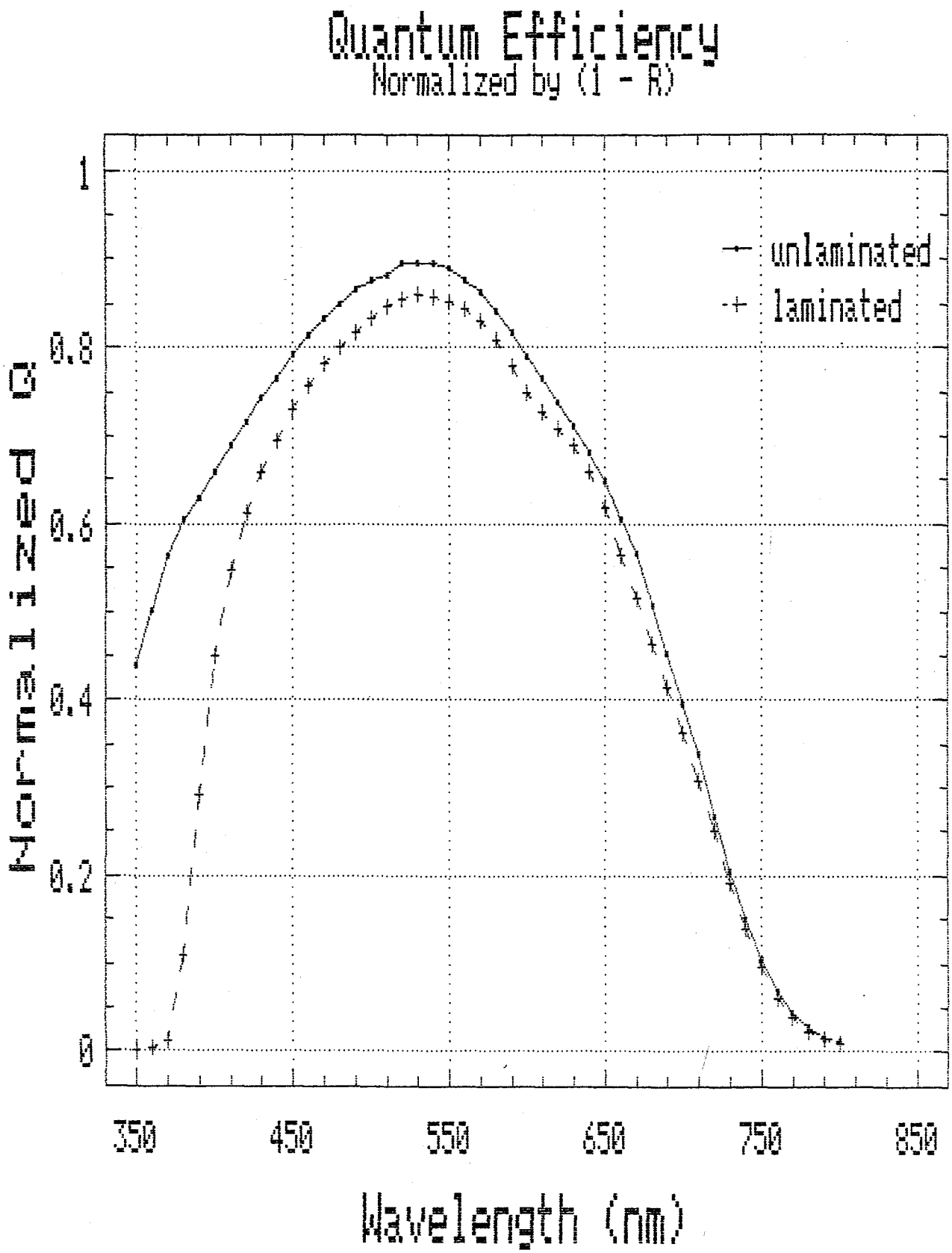

Fig. 18. Quantum efficiency shown in Fig. 17 normalized by one minus the front surface reflection (Q/(1-R)).

3.4 Interconnect Schemes

Figures 19a and 19b show the present interconnect scheme for the monolithic-type module and the series-connected module, respectively. After the BR/a-Si/ITO deposition, the module aperture area is then defined by ITO isolation with an etchant. In the case of the series-connected module, the strips are also isolated (to prevent ITO to ground contact when slabbing strips) using this etchant. The edge isolation line is 0.060″, while the strip isolation line is 0.030″. The isolation resistance is about 5 kohm. Next, the fingers are applied using a silver epoxy, screen printed onto the ITO surface, and cured. These lines are 250 μm wide by 4.7 cm with a conductivity of approximately 0.02 ohm/sq. The wire bus (26 AWG) is connected to each finger with silver epoxy and cured. The approximate diameter of each connecting dot is 2 mm.

The module, in the series-connected case, is next slabbed into six strips. Interconnection between strips is made by spot welding 1/8″ copper foil to ground, and the foil is soldered to wire bus bar of the neighboring strip. All isolation of copper and wire bus from ground is done with a 0.005″ polyester tape. In the monolithic-type module, wire bus bars are connected to 3/8″ copper foil. Modules are finally encapsulated in an EVA/Tefzel structure.

In Table III we show the loss analysis for the present module design. The major loss mechanisms are shadowing losses due to fingers, wire bus bars and connecting dots, electrical losses due to ITO, fingers and wire bus bars, interconnect resistance and inactive interconnect areas, and encapsulation transmission.

To experimentally determine the module losses, we measured the active area efficiency (overgridded to minimize electrical losses) for a small area cell and compared that to the aperture area efficiency of a completed module. The active area efficiency was determined to be 7.98%, while the module had an aperture area efficiency of 7.10%. This represents an 11% decrease from the active area efficiency, which is in good agreement with the total losses for the monolithic type module shown in Table III.

MONOLITHIC

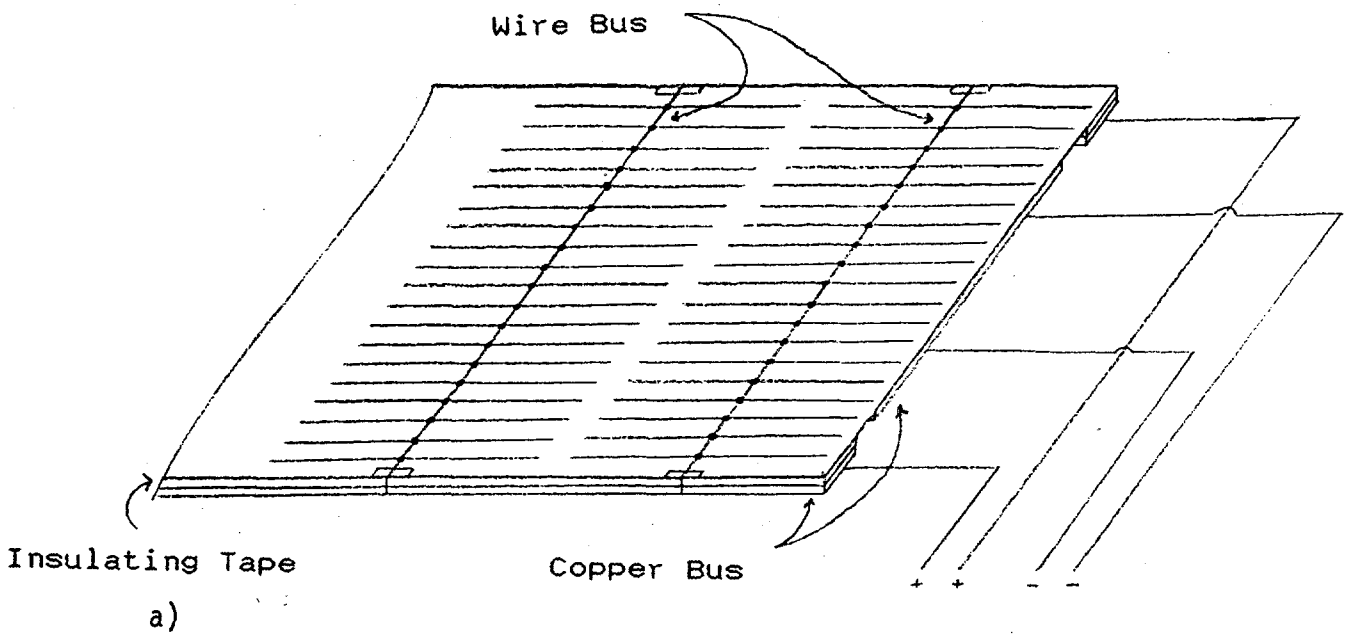

a)

SERIES CONNECTED

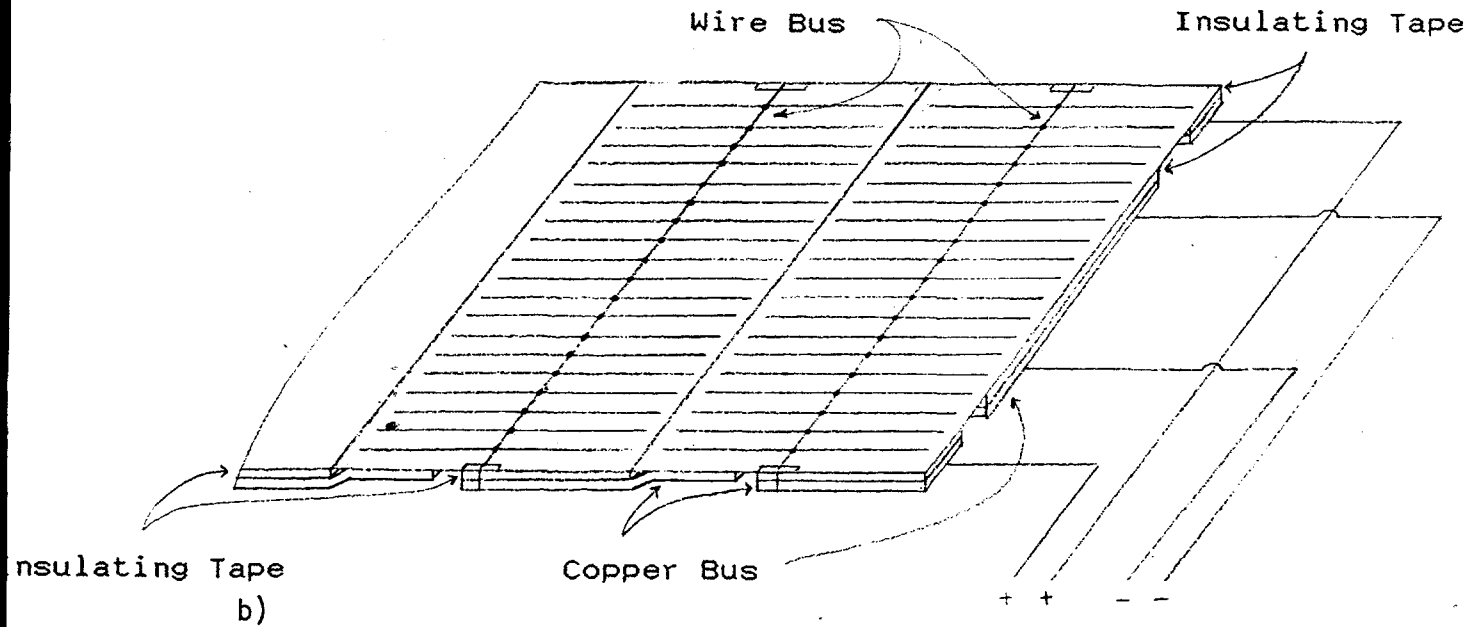

b)

Fig. 19. Schematic of the interconnect scheme for the a) monolithic-type module and b) series-connected module.

Table III. Module loss analysis of the monolithic-type and series-connected type modules.

Loss Mechanism	Monolithic Type (%)	Series Type (%)
Encapsulation[1]	3.0	3.0
Electrical[2]	2.7	2.8
ITO + Fingers	1.9	2.0
Wire Bus	0.8	0.8
Shadow	4.4	5.2
Fingers	3.8	3.8
Wire Bus	0.6	0.6
Interconnect	---	0.8
Total	10.1	11.0

[1] Determined by solar simulator measurements. Encapsulation loss as determined by Q.E. measurements is 7%. The source of the difference is being investigated.

[2] Calculated.

3.5 Characterization

To evaluate module efficiency, we use a Spire pulsed solar simulator, model Spi-Sun 240. This solar simulator is calibrated using a SERI calibrated AM1.5 global reference cell. The solar simulator is adjusted to the reference cell AM1.5 global calibration number and corrected for spectral mismatch between the Spire simulator, AM1.5 global, the reference cell spectral response, and the cumulative response of the individual junctions of the multijunction module. The quantum efficiency of the module is determined from the subcell quantum efficiency measurements.

3.6 Reliability Testing

We have developed or acquired equipment to perform the entire SERI interim qualification testing procedures. These include an environmental chamber capable of thermal cycling, or humidity freeze cycling, from -40 to 90°C as specified, mechanical loading, hail-impact, surface cut, wet and dry high potential, ground continuity, and electrical performance tests. Table IV shows a detailed list of tests available and the pertinent specifications.

Table IV. SERI interim qualification tests and their specifications and/or equipment.

Test	Specifications or Equipment
Electrical Performance	Spire Spi-Sun 240 solar simulator
Wet High-Pot	Immersed 0 - 2000 V
Environmental Chamber	-40 to +90°C 0 to 85% RH
Mechanical Loading	0 - 100 lbs / sq ft
Hail Test	1″ dia. 0 - 50 mph
Surface Cut	2 lbs load

We are presently in the design phase of constructing a large-area light-soaking facility. This facility will enable us to light soak modules at an intensity up to one sun at a specified temperature on a twenty-four-hour-a-day basis. This will be accomplished with an array of high pressure sodium and/or metal halide lamps capable of uniformly illuminating a large surface. The temperature will be controlled and maintained at a specified temperature by the use of air circulating fans.

SECTION 4
ACCELERATED STAEBLER-WRONSKI TESTING

4.1 Introduction

As we strive to reduce the gap between initial active area efficiency and the stabilized final total area efficiency, we must focus on reducing Staebler-Wronski (S-W) degradation. Despite considerable effort expended on this subject, the S-W effect remains the highest single derating factor when projecting final module output from the initial active area efficiency of the solar cell. Whether attempting to understand the physical mechanisms or engineering an optimal material or design, one of the biggest obstacles to evaluating the magnitude of this effect is the very large amount of time it takes to determine the maximum degradation under normal outdoor conditions.

The use of indoor simulated light at an intensity of one sun decreases the time required by only about a factor of five. This still leaves an evaluation period of at least several months. This is far too long of a period to perform any reasonable studies. In view of these facts, many labs have now resorted to some kind of accelerated testing.[4] This typically involves intensity levels well in excess of one sun and temperature ranges far exceeding those experienced under field conditions.

4.2 Experimental Setup

To achieve this accelerated testing and reasonable turn-around time on S-W results, we have designed and built a completely automated data acquisition system capable of such testing (see Fig. 20 for schematic). This apparatus enables us to light soak a given sample with an intensity range of dark to 100 times AM1.5 under ELH spectrum at any temperature between 15 and 225°C. We have incorporated a fast shutter to provide light soaking intervals resolved to tenths of seconds. There are also three separate temperature plates, each operating at an independent temperature. Any one of these plates may be engaged at any time to make intimate contact to the back of the stainless steel substrate. The interchange of any two plates of different temperature (e.g., 100°C to 25°C) and the

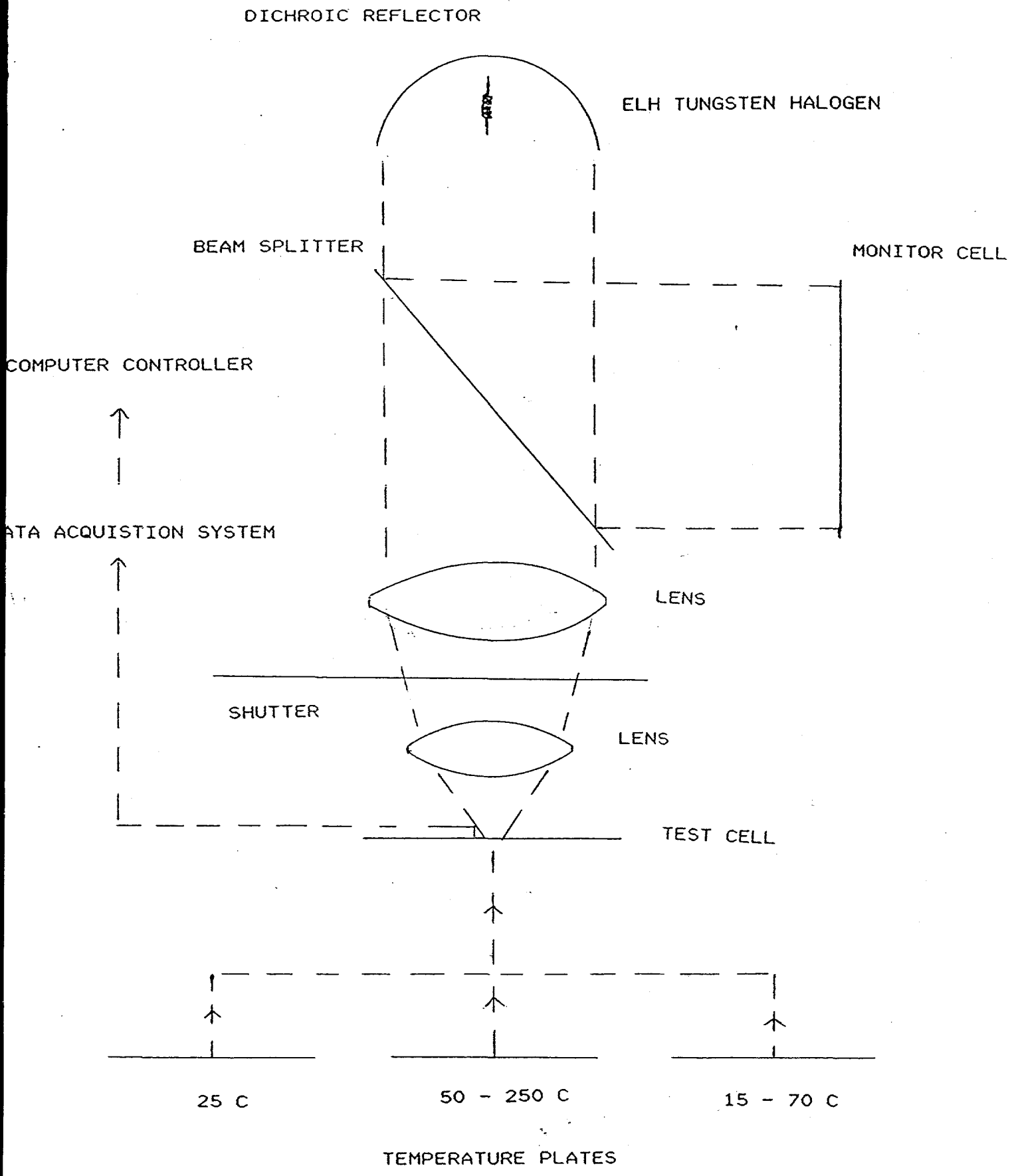

Fig. 20. Schematic of the accelerated Staebler-Wronski tester.

stabilization of device temperature to within 5°C is typically 4-7 seconds (in 1-3 seconds the device is within 10°C of equilibrium).

We are also able to measure the current-voltage characteristics of the device in situ. This is achieved by simply engaging the correct temperature plate, adjusting the ELH lamp to the desired intensity, and measuring the I-V characteristics. This allows us to determine the exact effect the light and/or temperature soaking has on the device. We are then able to determine the rates of degradation and/or annealing at any time between the initial measurement and the final saturation. (It is important to comment at this point that we believe that for optimization of single-junction cell devices, which will be used for the middle and bottom of a multijunction device, the reddish spectrum of the ELH is more appropriate than that of a Xenon source.)

4.3 Theory

In order to obtain stability data under normal operating conditions (one sun or less at temperatures of 50°C or less), we need a kinetics model that accurately describes the device stability. The model used to approximate the degradation of these devices as a function of intensity, temperature, and time was taken from a published model[5] and modified to more accurately describe our data. The rate equation for light induced degradation (LID) and thermal induced anneal (TIA) is

$$\frac{dN(E)}{dt} = \exp\left(\frac{-A_d(E)}{KT}\right) G^{X_1}\left(\frac{C_1(G)}{N(E)} + \frac{C_2(G)}{N(E)^2}\right)\left(N_g(E,G) - N(E)\right) - k\exp\left(\frac{-A_a(E)}{KT}\right) N(E)^{X_2} \qquad (1)$$

where G is the generation rate, N(E) is the number of metastable defects at energy E, N_g (E, G) is the maximum possible number of metastable states at energy E, which is a function of G, and X_1, X_2, $C_1(G)$, $C_2(G)$ are coefficients to be determined for each sample. The first is the LID term with a distributed activation energy $A_d(E)$, and the second term is the TIA term with a distributed activation energy $A_a(E)$. To convert solar cell power output to number of metastable defects, N, a standard collection length formula was used.[6] Fig. 21 shows, for a typical set of parameters, the relationship between normalized efficiency and normalized N for various thicknesses.

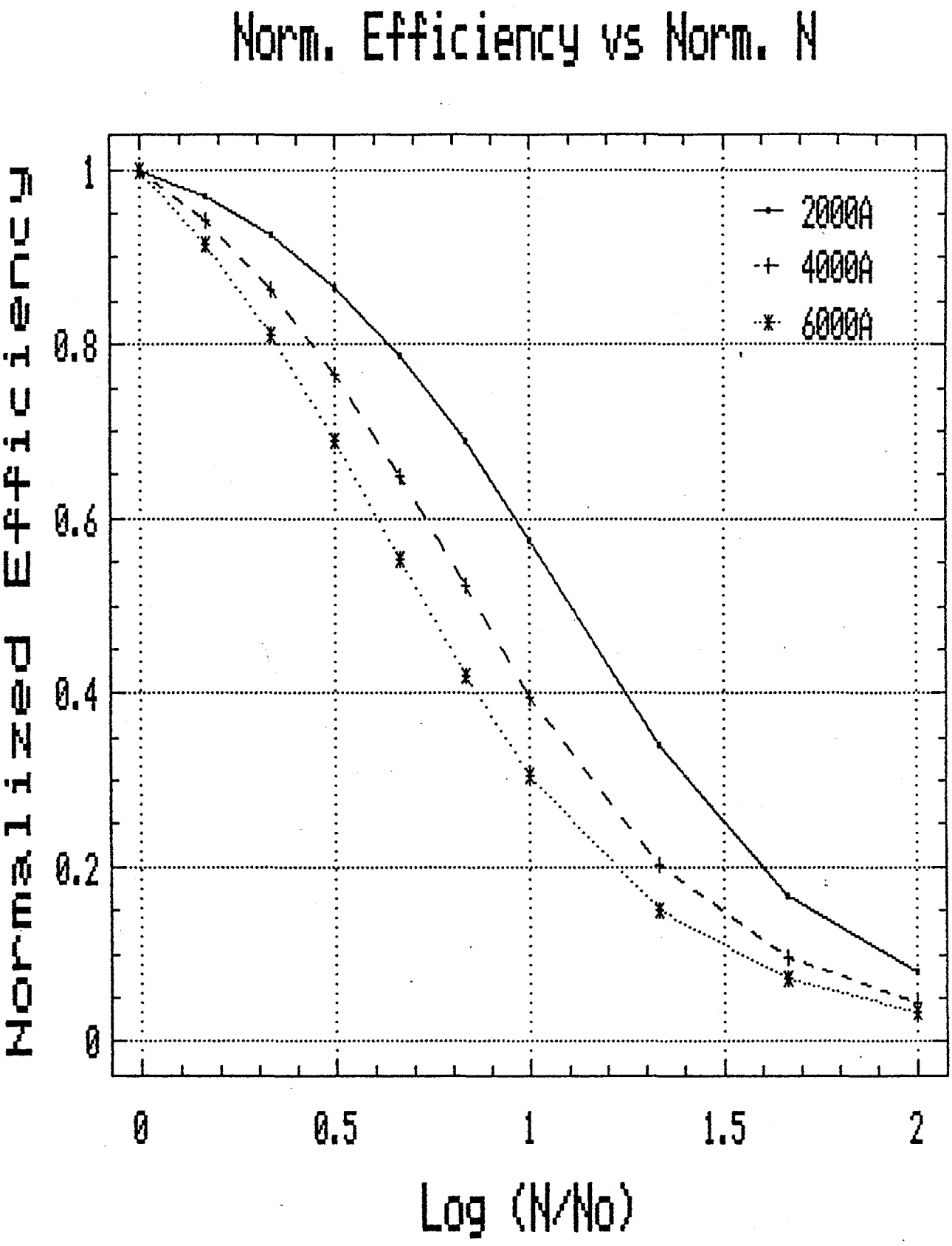

Fig. 21. Plot of normalized efficiency versus normalized N calculated for three different thicknesses.

The typical curve fitting parameters from Eq.1 are listed in Table V. It should be noted that not all of these parameters are strictly determined independent of one another. The intensity dependence of the constants C_1 and C_2 were determined empirically to be linear with intensity. The final saturation density N_{sat} is not determined absolutely (e.g., 2 x 10^{17}) but with respect to the initial density N_0; therefore, these ratios are given in Table V. The activation energies for LID and TIA are approximately 0.12 and 0.9 eV, respectively. The distributed activation energies were incorporated to provide a much improved data fit for the time regions around the onset of saturation at the various temperatures. This onset was much too gradual to be explained by a single activation energy. The distribution for both activation energies as well as N and N_0 were assumed to be gaussian in shape.

Table V. Typical curve fitting parameters for an a-Si:H single-junction cell used in Eq. 1 in text.

Activation Energy for TIA	0.9 ± 0.1 eV
Activation Energy for LID	0.15 ± .03 eV
N_{sat} / N_0	10 - 20
X_1	2
X_2	8 - 10
C_1 (m,b)	.01, .08
C_2 (m,b)	.03, .01

4.4 High Intensity/Temperature Studies

In Figs. 22a and 22b we show the energy distribution of the metastable defects versus time and temperature at an intensity of 55 suns. Note that at lower energies the saturated density rises to a value lower than $N_g(E)$. $N_g(E)$ is the maximum number of defects that can be generated at energy E. At the higher temperatures this difference becomes larger as well as shifting to higher energies. Note also that a central energy is not specified since the shape of the degradation curve is only dependent on the relative energy distribution.

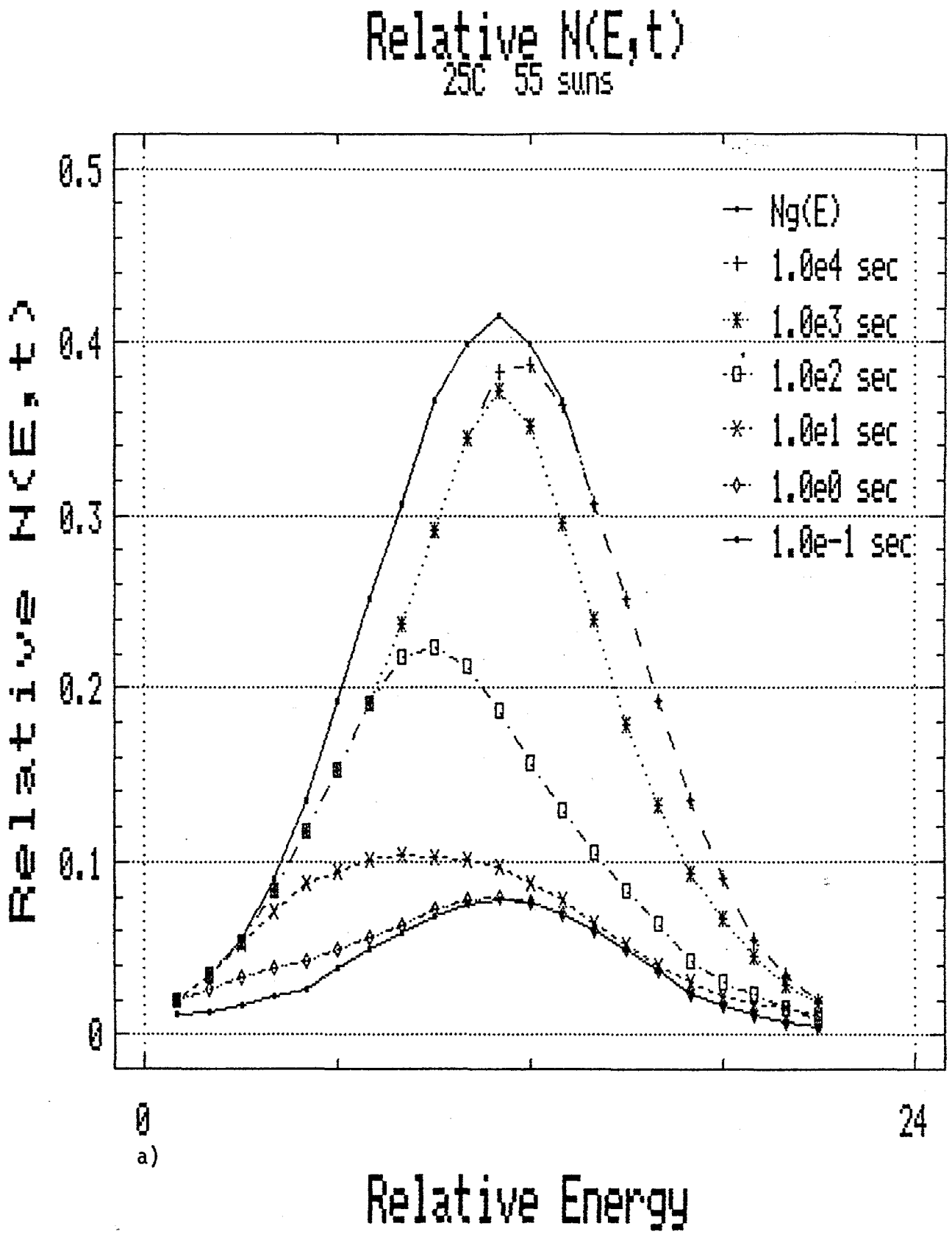

Fig. 22a. Relative N(E,t) for a device illuminated at 55 suns and a temperature of a) 25°C and b) 75°C.

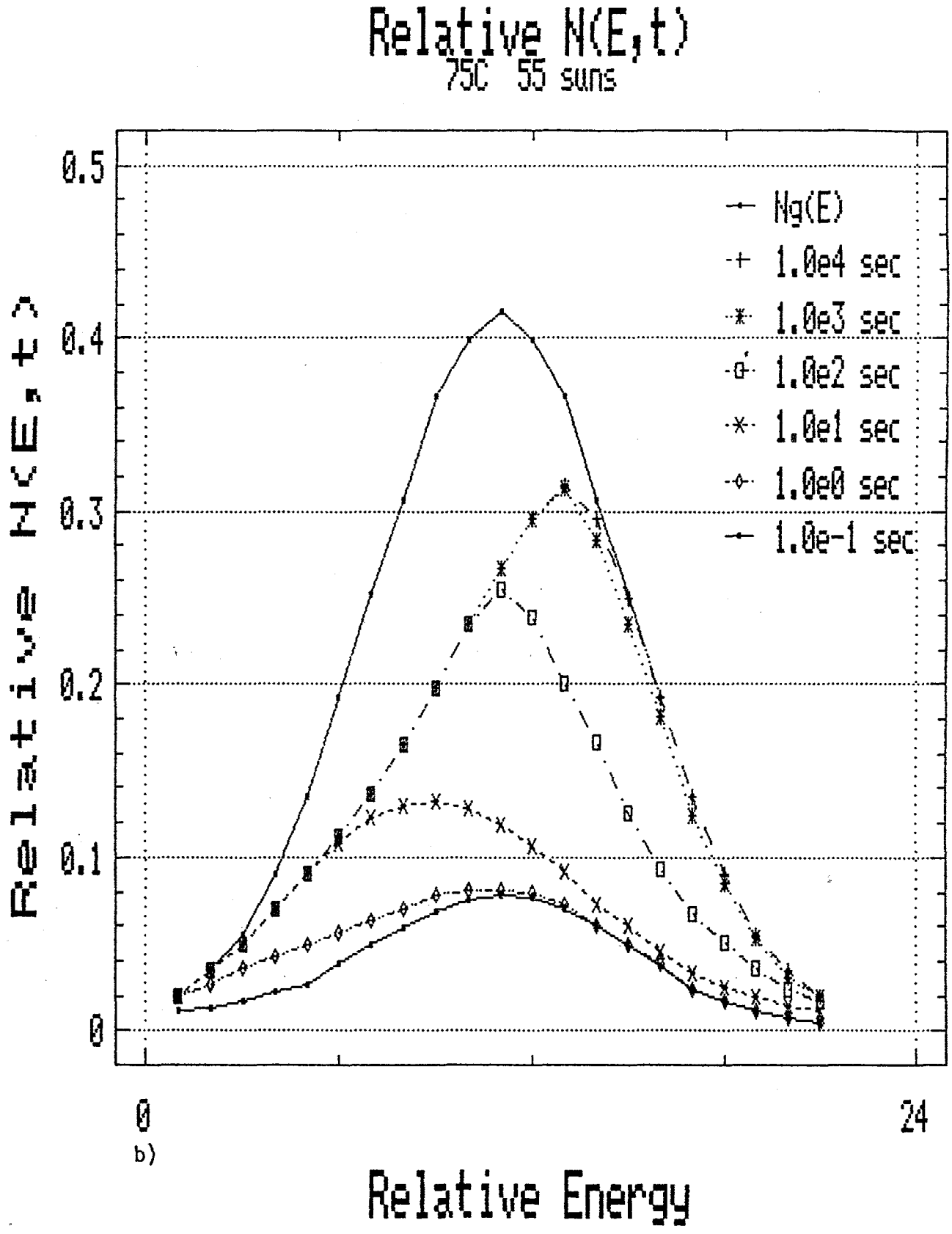

Fig. 22b. Relative N(E,t) for a device illuminated at 55 suns and a temperature of a) 25°C and b) 75°C.

Figure 23 shows that the final saturation at any given intensity is independent of the initial starting density N_o (in Eq. 1 N(E) at an arbitrary time zero). This figure shows the stability characteristics of a device degraded at 50 suns that was annealed to different levels but saturating to the same value. This data has been normalized in Fig. 24 to demonstrate the extreme danger in considering the normalized degradation. It can be seen here that the device history can play an important role in this quantity, thereby leading to possible erroneous conclusions. This will certainly depend on the light exposure and thermal history of the device such as AM1 characterization time and the time exposed to elevated temperatures after a-Si deposition such as during TCO and metalization deposition processes. We therefore would like to emphasize absolute efficiency in analyzing data.

4.5 Extrapolated One-Sun Studies

In order to arrive at the stability characteristics under normal operating conditions, we must first measure the device at various levels of high intensity light and a range of temperatures that will include the normal device operating temperatures. Once this has been evaluated, we may fit the model to this data by varying the coefficients to minimize the rms error. Using the coefficients obtained from the high intensity data, we then change only the intensity and temperature to evaluate the extrapolated one-sun conditions.

Figure 25 shows an example of a test procedure run on an a-Si single-junction cell. This device, which has an *i*-layer thickness of 4000 Å, was degraded at intensities ranging from 7 to 82 suns and temperatures from 25 to 75°C. In this example, the data at 52x, 65x and 82x at 25 and 75°C (six curves) was curve fit by the model to determine the coefficients for this particular sample. In between each degradation cycle, the cell was annealed at 175°C for 10^4 sec. Figures 26, 27, and 28 show the exactness of the curve fitting using Eq. 1. The rms error for this data fit was about .04 mW per point (0.6% per point), which is typical. Once the coefficients were obtained, we simply changed the intensity and temperature (while keeping all coefficients constant) to evaluate the ability of Eq. 1 to extrapolate the high intensity degradation to lower intensities at various temperatures. Figures 29, 30, and 31 compare the calculated (extrapolated) data to the actual measure data at the given intensities and temperatures. Figure 32 shows the one sun extrapolated and measured data for another sample.

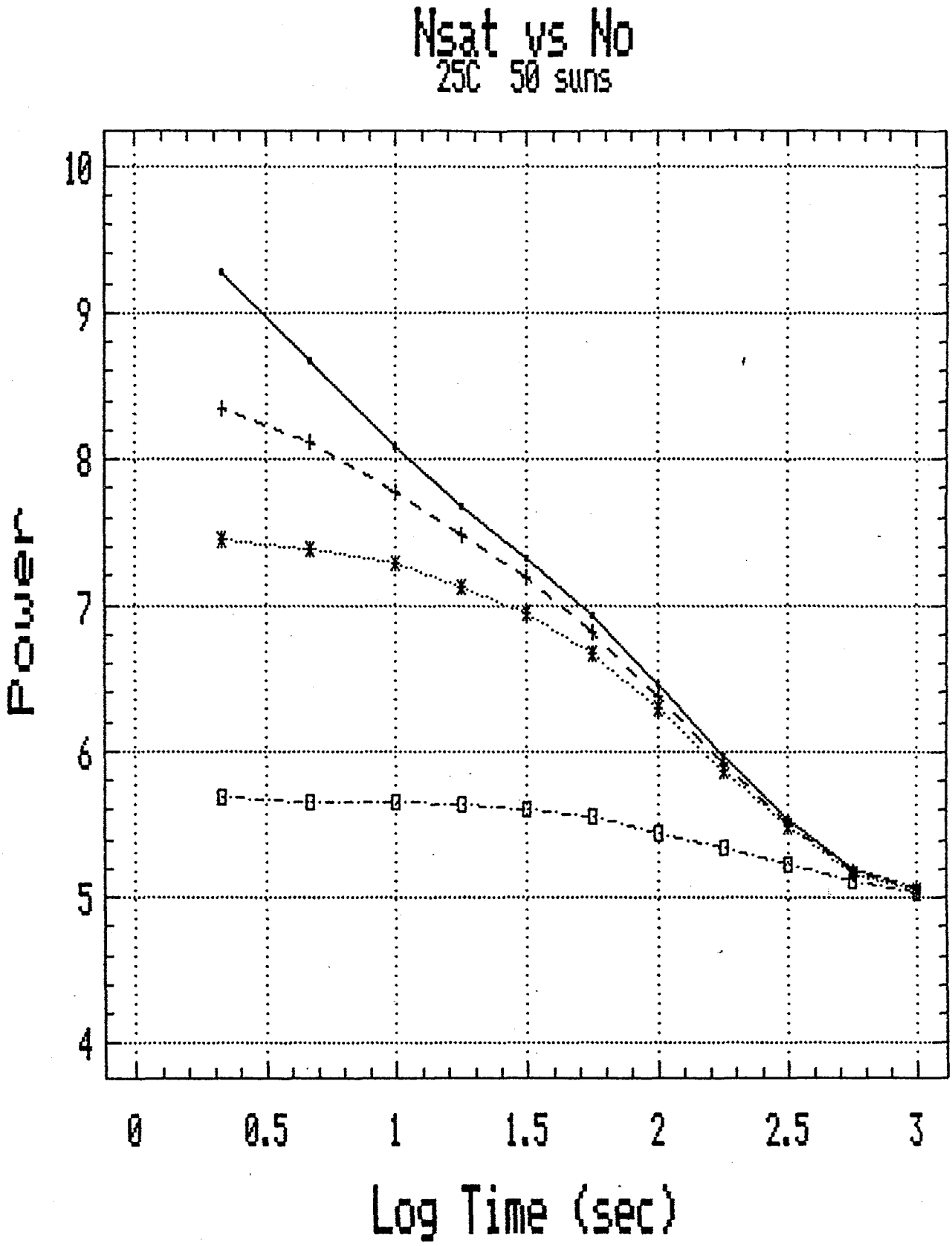

Fig. 23. Power versus time for an a-Si:H device illuminated at 50 suns and a temperature of 25°C for various levels of recovery.

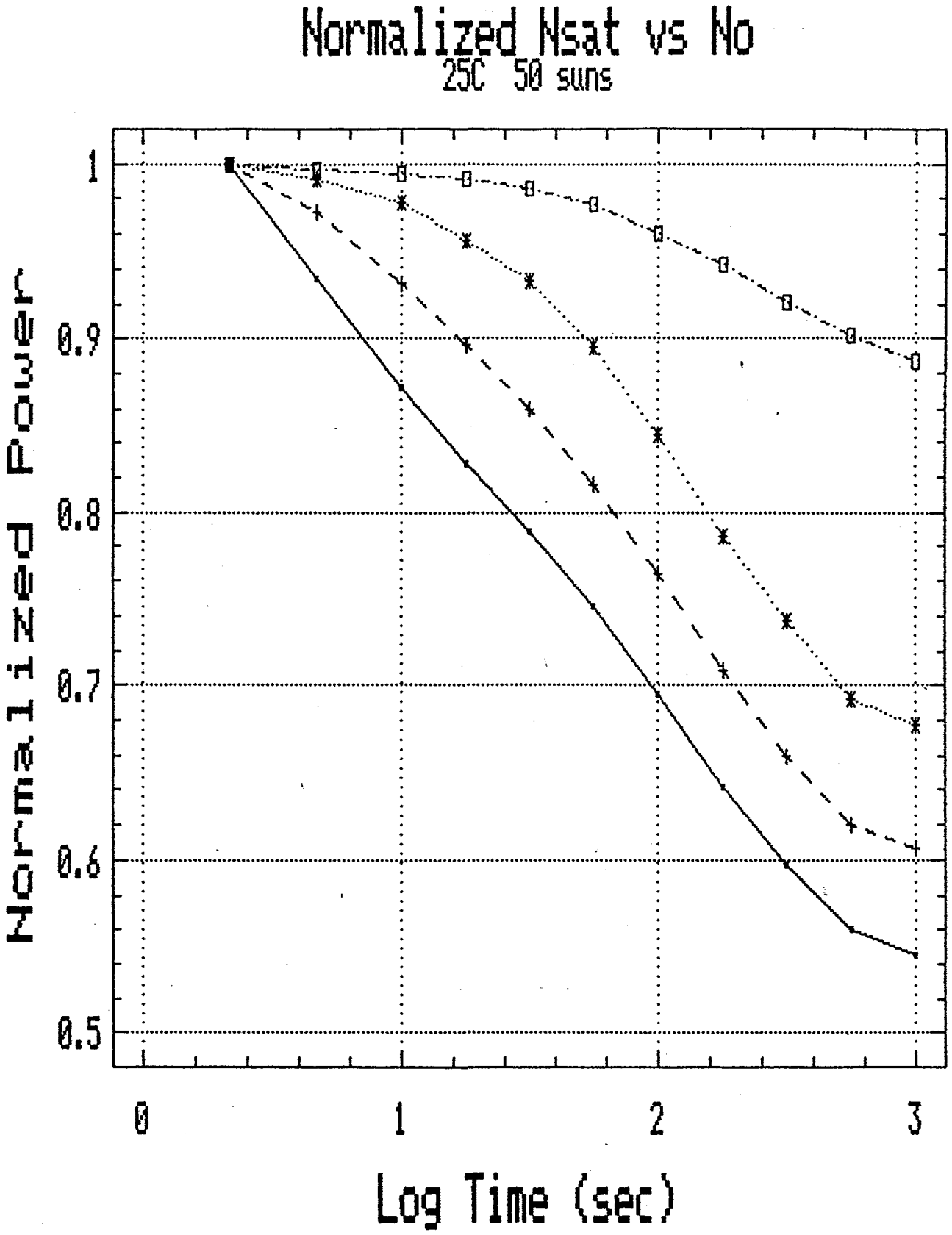

Fig. 24. Normalized initial power versus time for curves from Fig. 23.

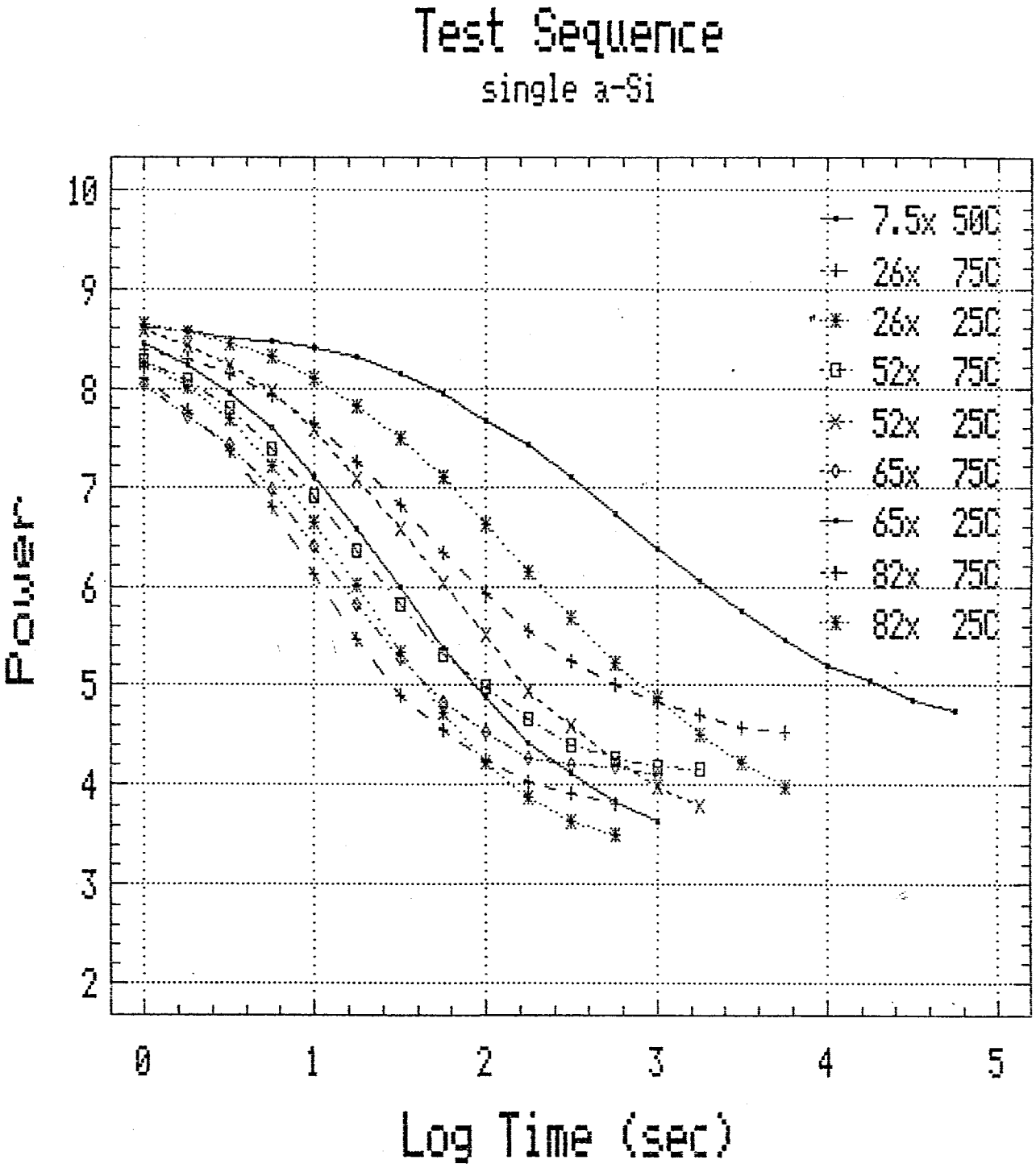

Fig. 25. Test sequence performed on an a-Si:H single-junction cell at various intensities and temperatures.

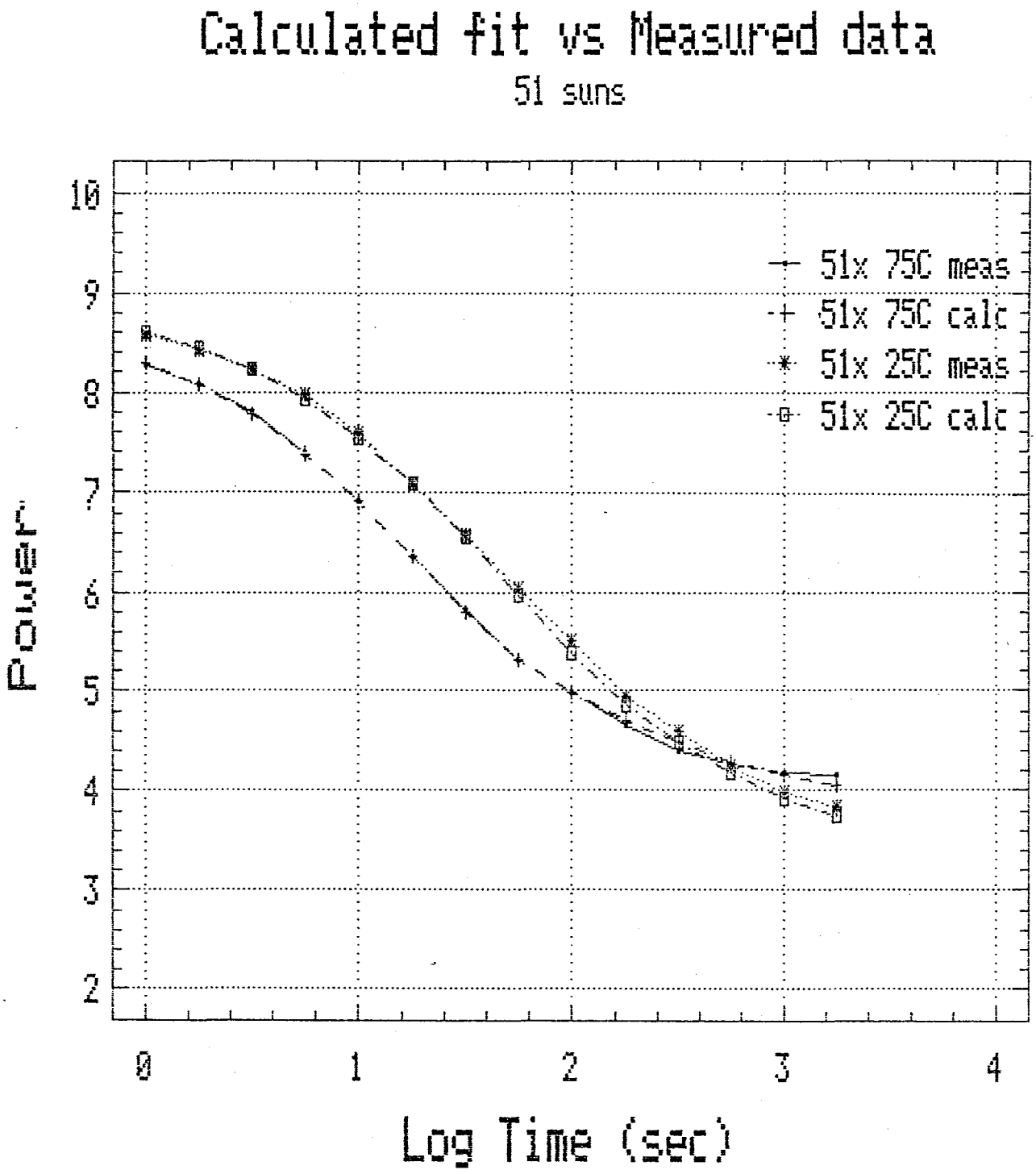

Fig. 26. Evaluation of the exactness of curve fitting from Eq. 1 for a device illuminated at 51 suns and 25 and 75°C.

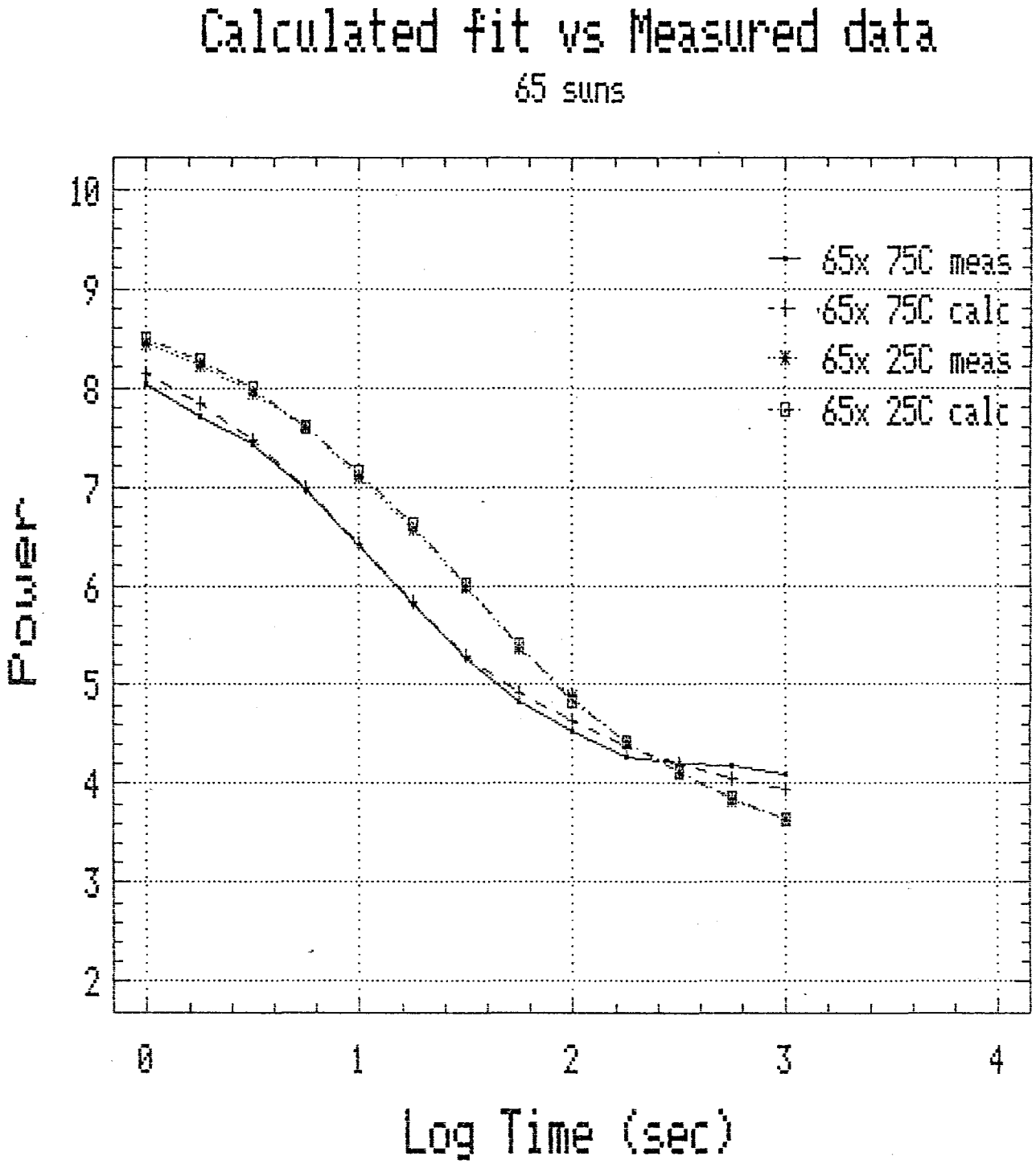

Fig. 27. Evaluation of the exactness of curve fitting from Eq. 1 for a device illuminated at 65 suns and 25 and 75°C.

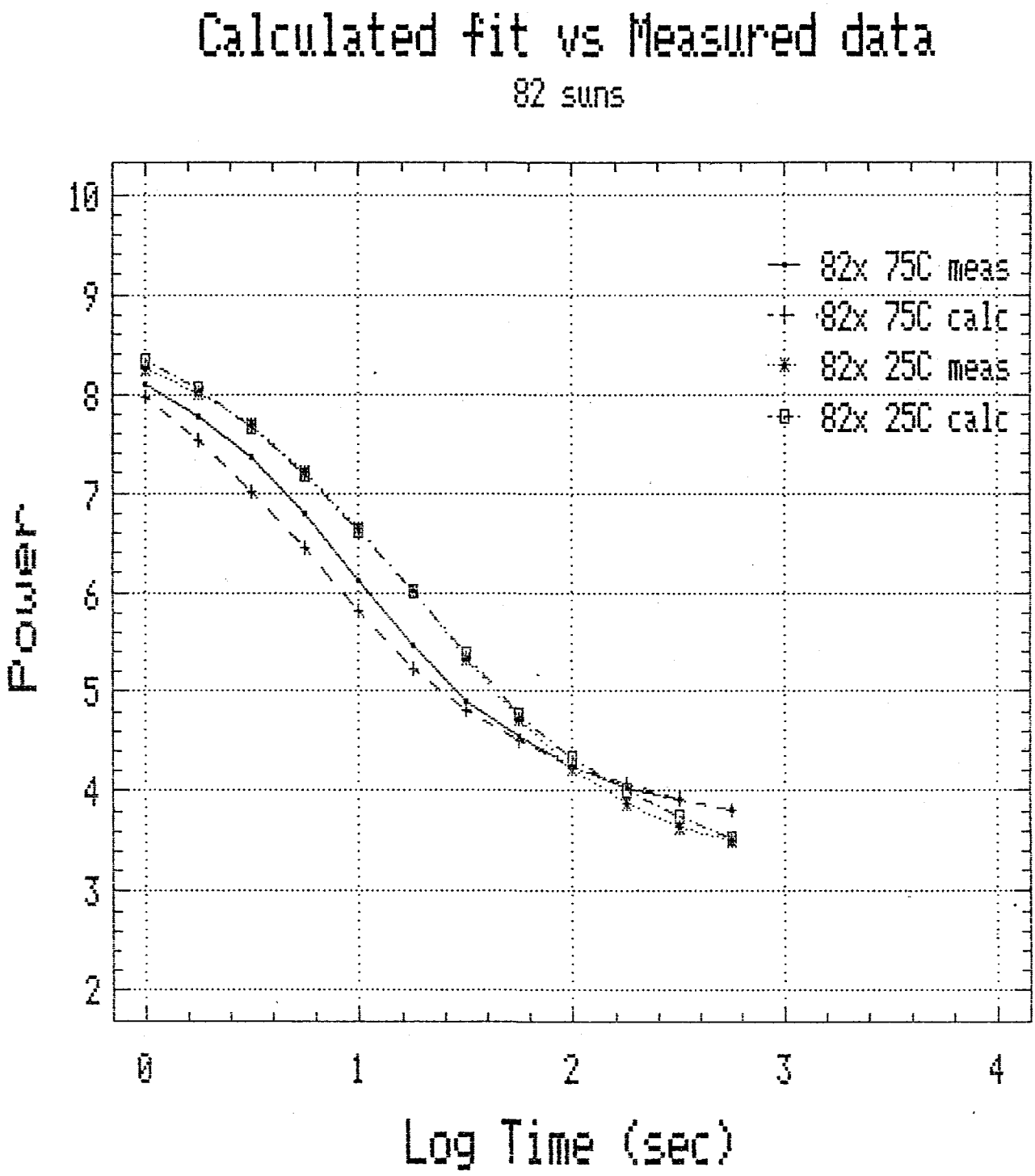

Fig. 28. Evaluation of the exactness of curve fitting from Eq. 1 for a device illuminated at 82 suns and 25 and 75°C.

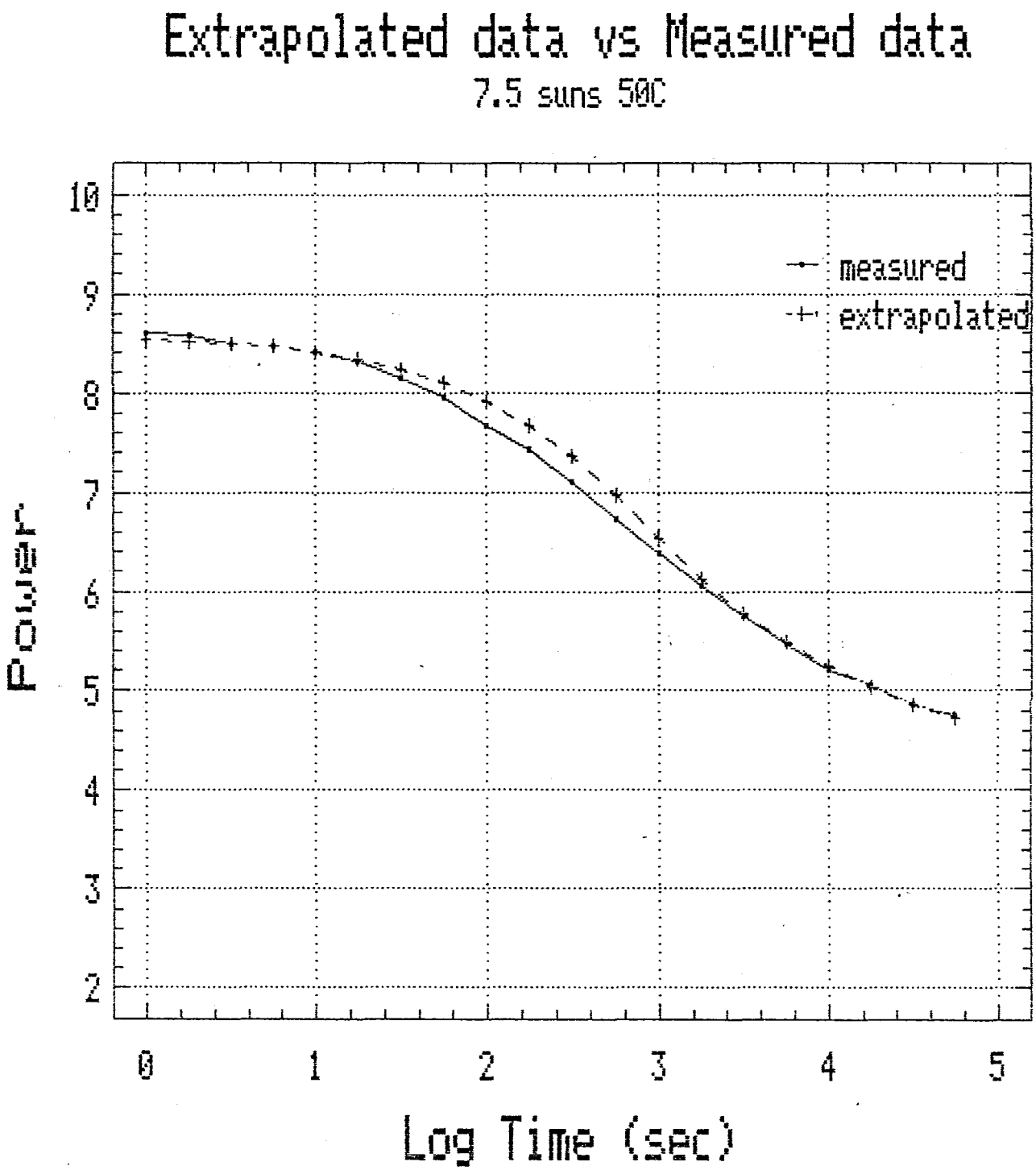

Fig. 29. Comparison of extrapolated data, determined from coefficients derived from data in Figs. 26-28 by Eq. 1, and measured data at 7.5 suns and 50°C.

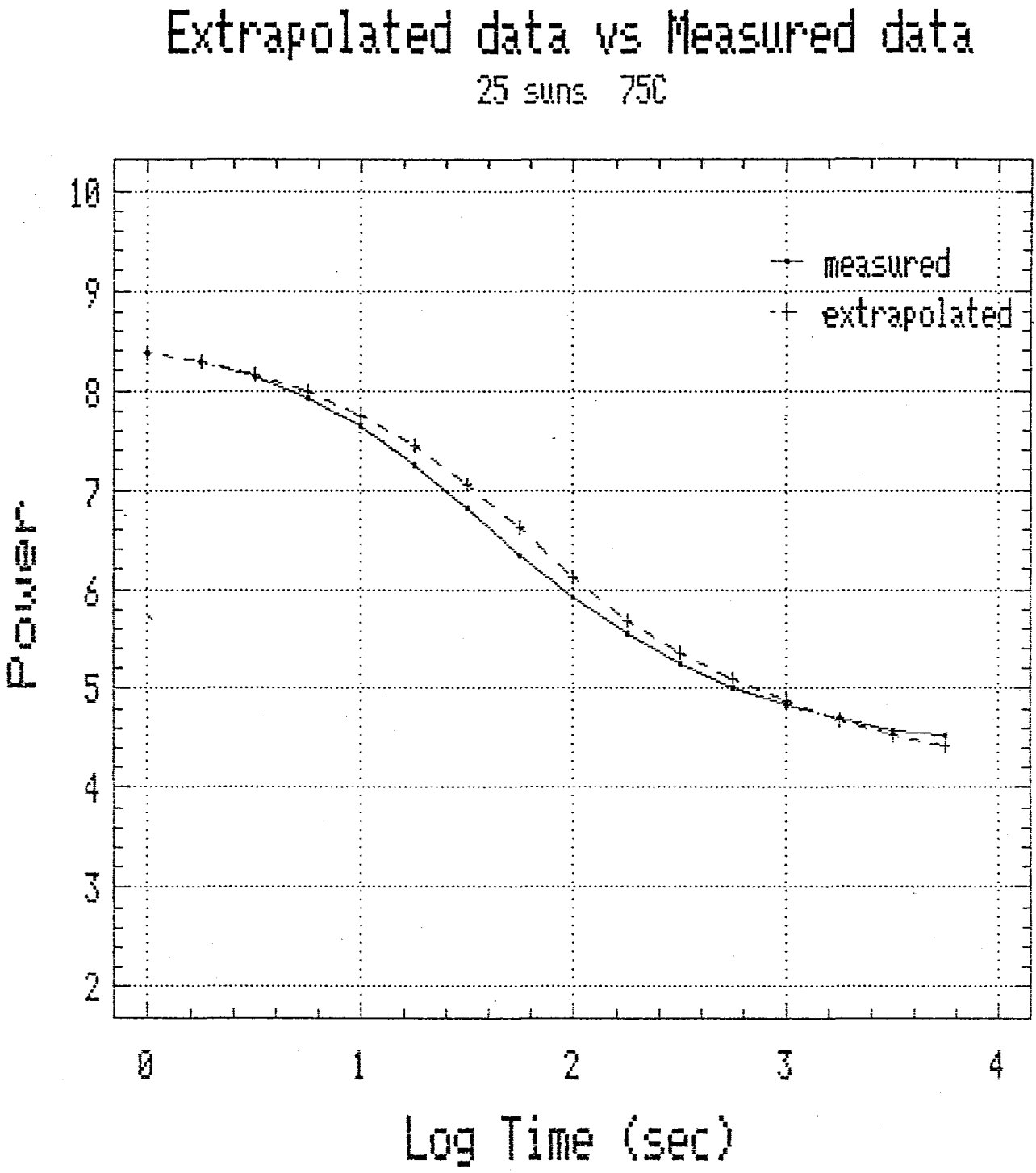

Fig. 30. Comparison of extrapolated data, determined from coefficients derived from data in Figs. 26-28 by Eq. 1, and measured data at 25 suns and 75°C.

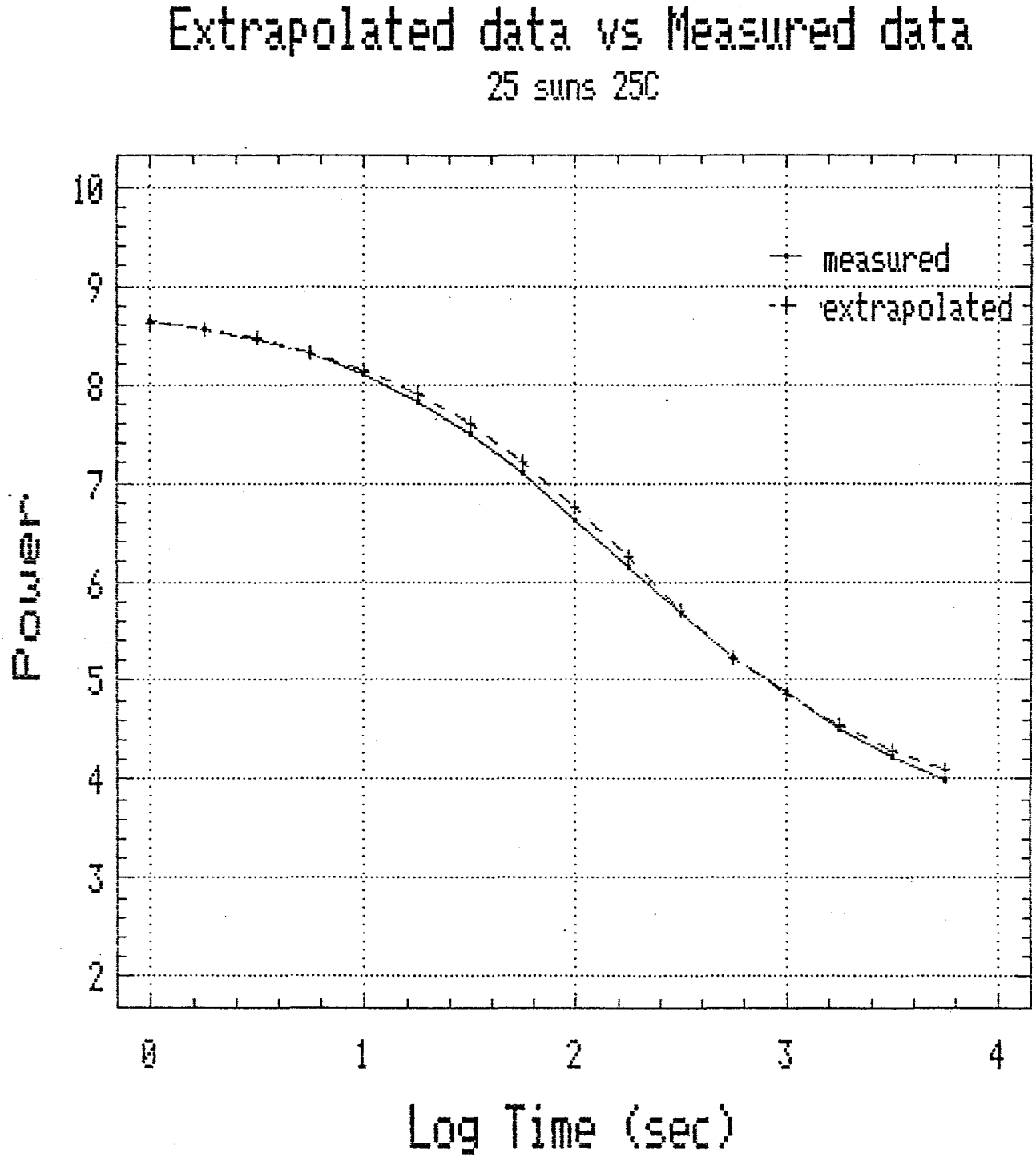

Fig. 31. Comparison of extrapolated data, determined from coefficients derived from data in Figs. 26-28 by Eq. 1, and measured data at 25 suns and 25°C.

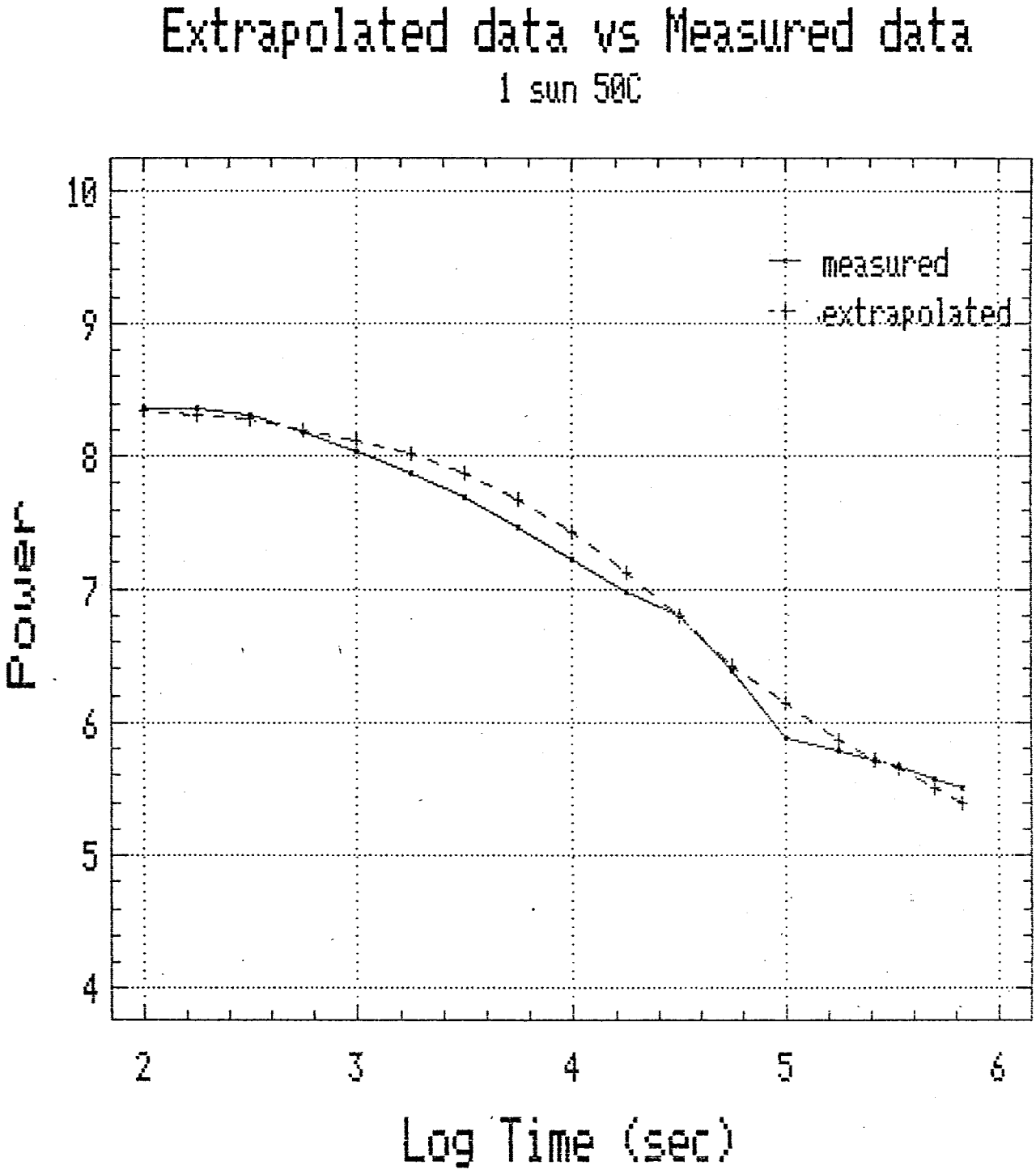

Fig. 32. Comparison of extrapolated data, determined from coefficients derived from high intensity data by Eq. 1, and measured data at one sun and 50°C.

We have now completed several one-sun (extrapolated) studies. The first two involve determining the role of device thickness on stabilized power for devices on specular stainless steel and specular Ag/ZnOx back reflector. These two sets of samples were prepared with *i* layer thicknesses ranging from 850 Å to 5100 Å (deposited at a rate of 85 Å/min). Then for each sample, the one sun 50°C results were extrapolated from the high intensity measurements.

In the stainless steel case, we find that the optimal thickness changes from about 4200 Å for the initial efficiency to about 3000 Å for the final stabilized efficiency (Figs. 33 and 34). For the back reflector case, we find a very dramatic change in optimal thickness from nearly 5100 Å to just 2100 Å (Figs. 35 and 36). It is quite amazing to find a sample of 850 Å thickness to have a higher stabilized power than that of a 5100 Å device.

It can be concluded that most of the shift in final efficiency peak from 3000 Å for the stainless steel to 2100 Å for the back reflector is seen in the features of the initial efficiency curves (Figs. 34 and 36). As the thickness of the device is increased from 850 Å, we see a much quicker rise in power in the back reflector case. Although there is some variation, the normalized change in efficiencies is similar for the stainless steel and back reflector cases for a given thickness.

It is also interesting to note the difference between the two cases in the one-sun degradation curves (Figs. 33 and 35). In the back reflector case, we see that we have a considerably quicker saturation time than for the stainless steel case, especially for the thicker samples. This is a result of the considerably higher current densities seen in the back reflector case (17 mA/cm^2 compared to 13 mA/cm^2). This allows a higher defect creation rate and more rapid approach toward its saturation density.

Figure 37 shows the effect deposition temperature has on S-W. All the a-Si single-junction cell devices in this study were approximately 4300 Å and deposited on bare stainless steel. We find the optimal temperature of these devices is the same before and after light soaking, that is, 300°C. Moreover, the final efficiency of cells deposited at 350°C is no better than that of cells deposited at 250°C or 300°C.

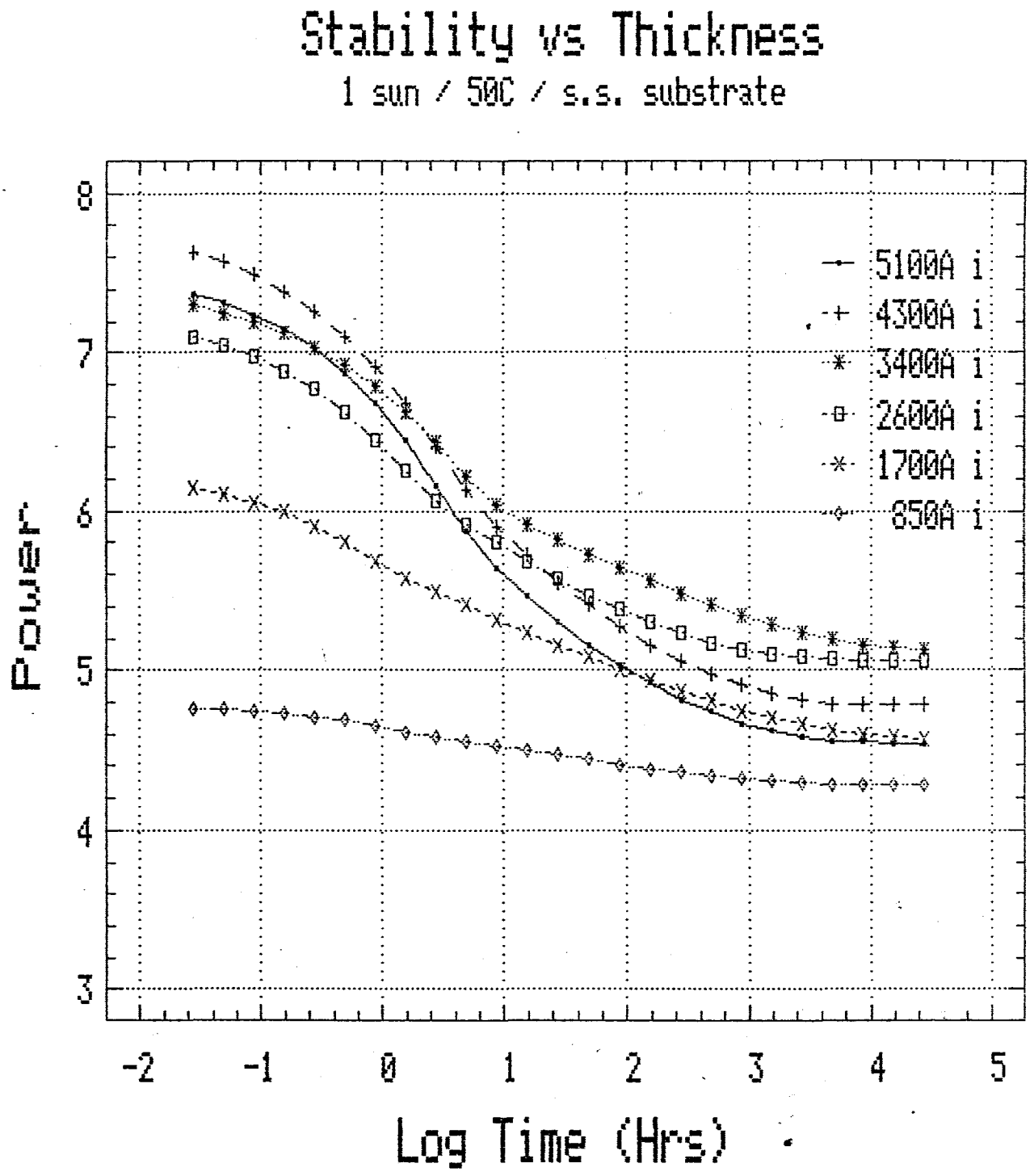

Fig. 33. Extrapolated power versus time for various thicknesses of a-Si:H single-junction cells, deposited on bare stainless steel substrates, for one sun and 50°C conditions.

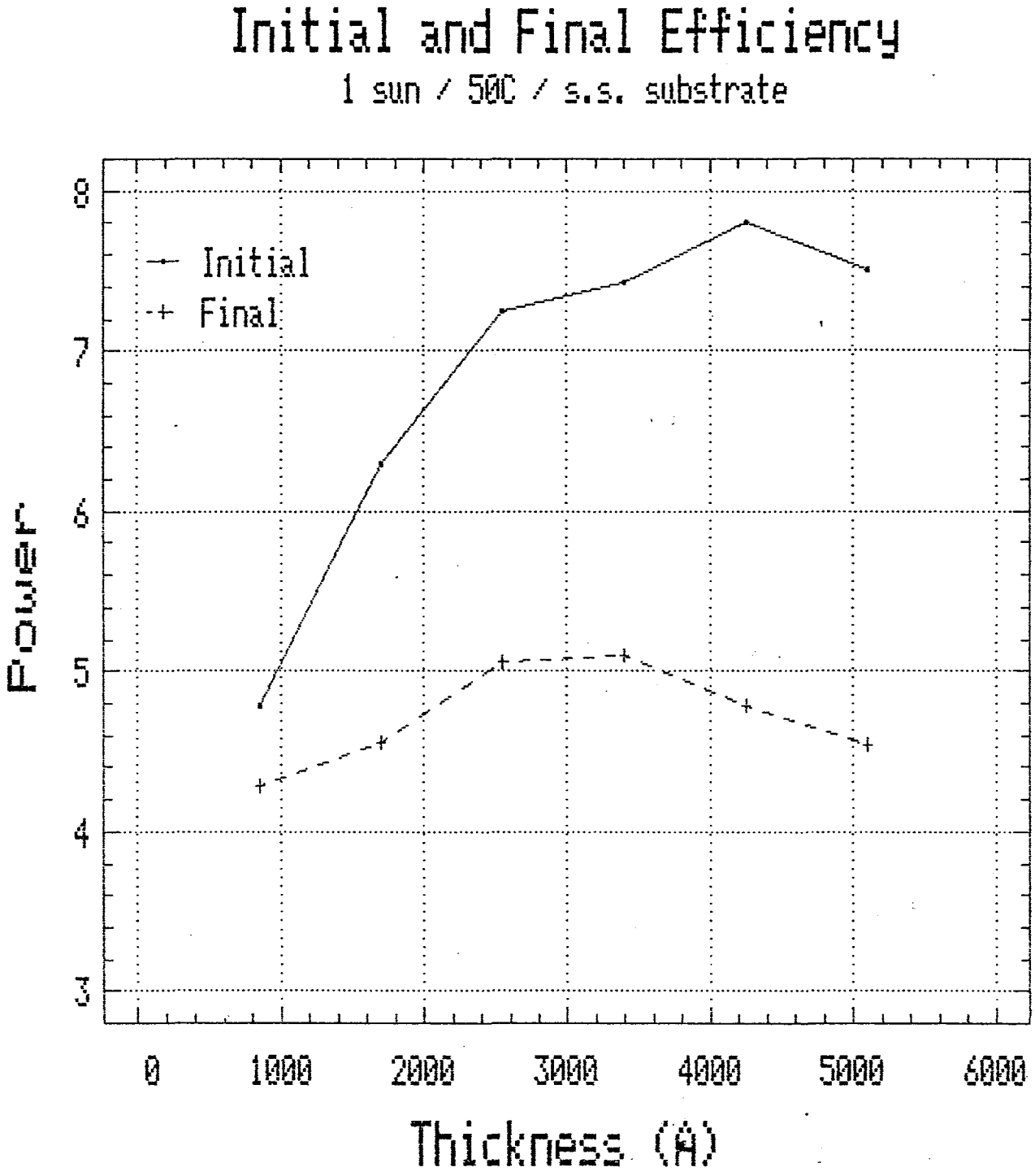

Fib. 34. Initial and final efficiencies for the extrapolated one sun data shown in Fig. 33.

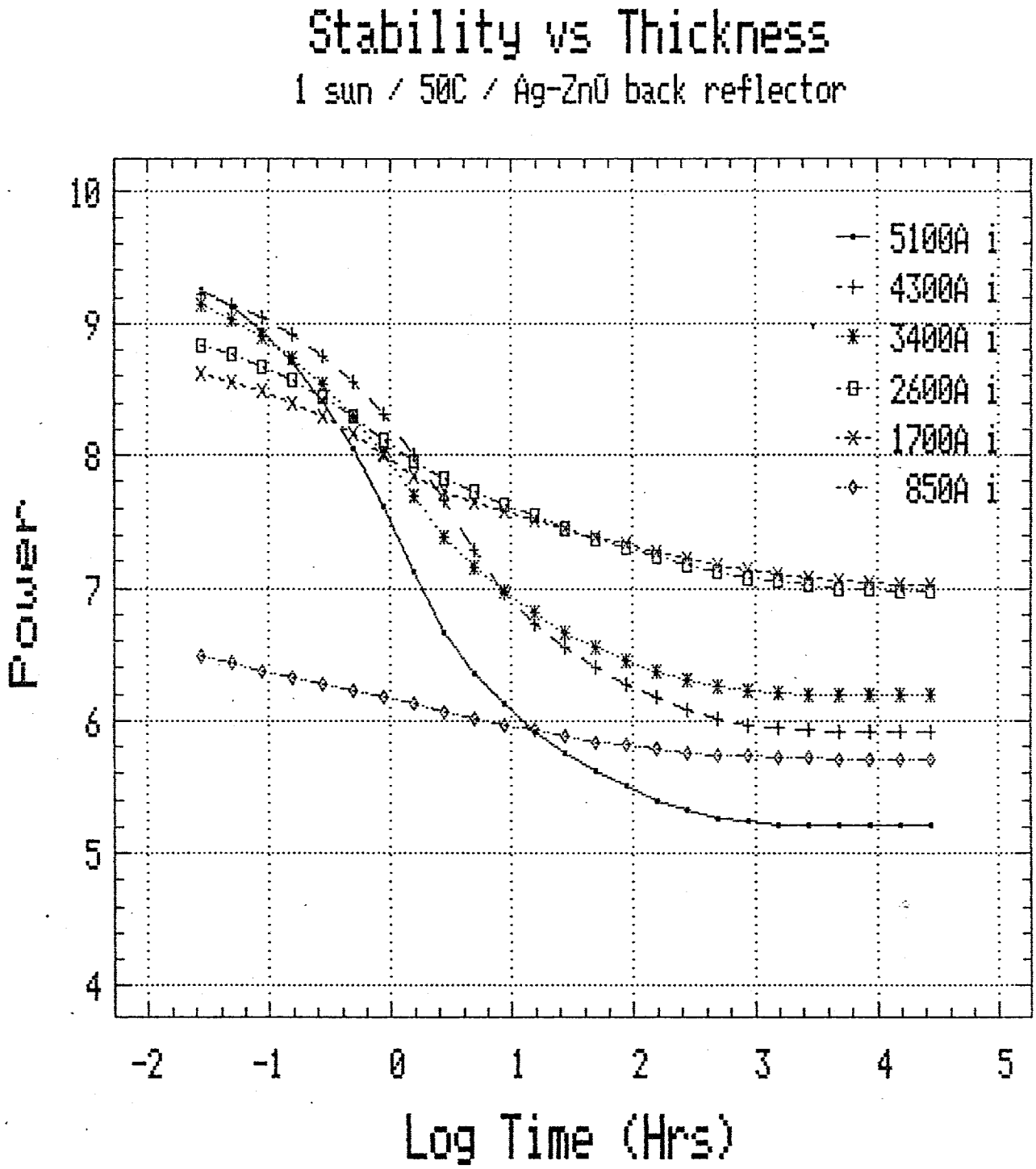

Fig. 35. Extrapolated power versus time for various thicknesses of a-Si:H single-junction cells, deposited on specular Ag/ZnO back reflectors, for one sun and 50°C.

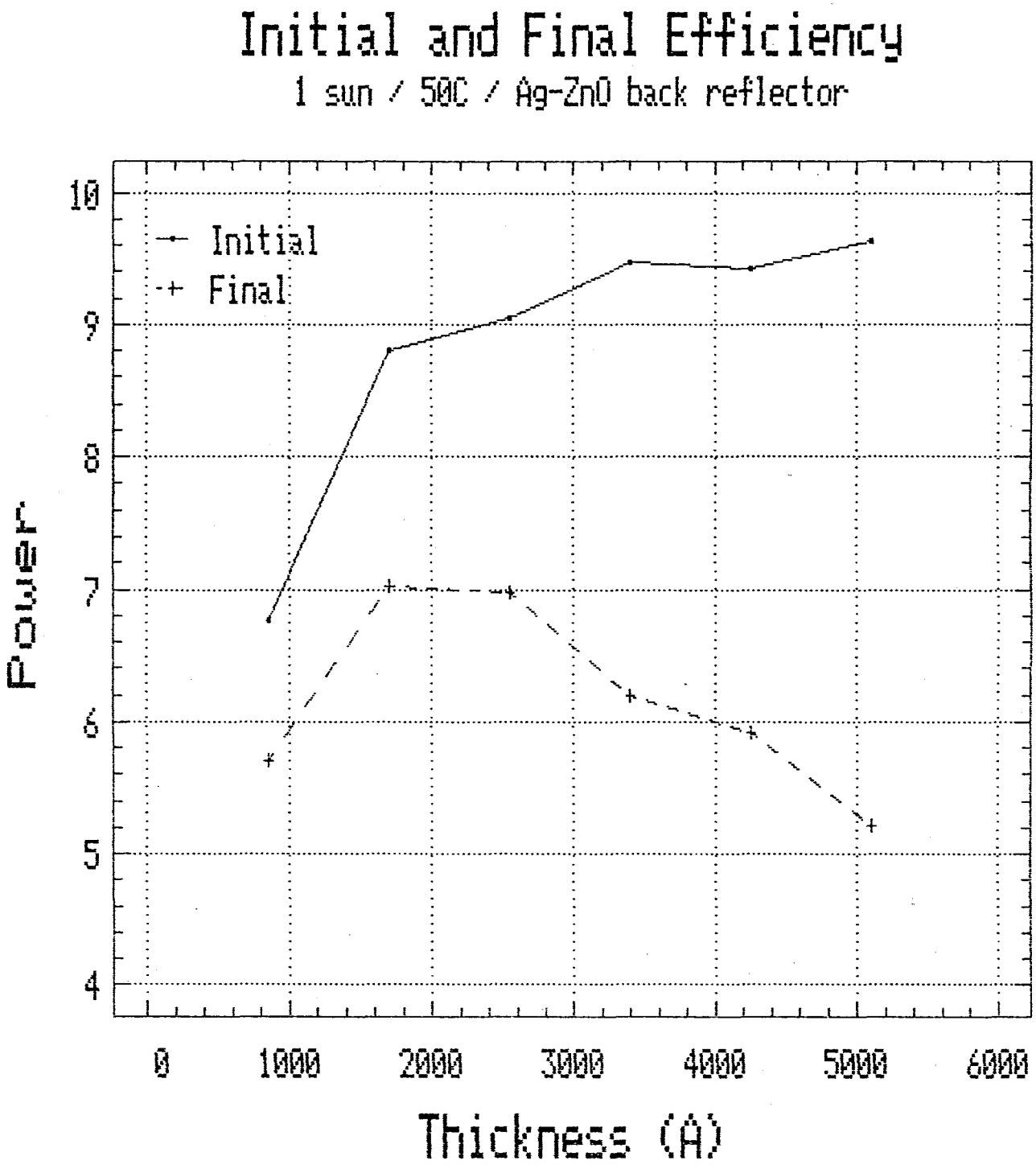

Fig. 36. Initial and final efficiencies for the extrapolated one sun data shown in Fig. 35.

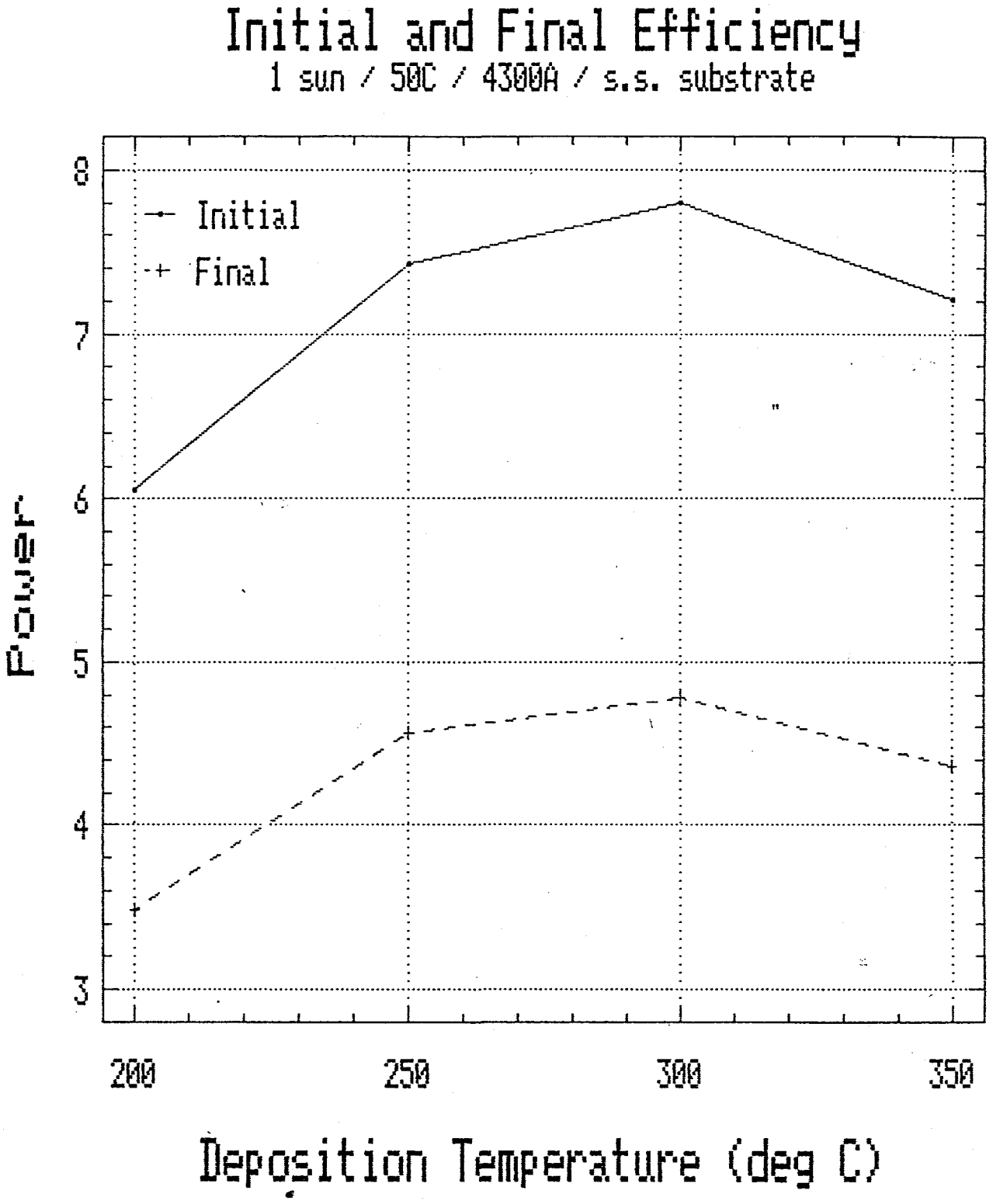

Fig. 37. Initial and final efficiencies for the extrapolated one sun data of a-Si:H single-junction cells, deposited at various temperatures at a thickness of 4000 angstroms.

SECTION 5
NUMERICAL ANALYSIS ON a-Si:H SINGLE-JUNCTION CELL STABILITY

5.1 Calculations of FF Under AM1.5 Blue and Red Illumination

Our earlier studies[7] of degradation under intense illumination showed that single-junction cells deposited at 200°C (LT-low temperature) had higher initial and final efficiencies than those deposited at 300°C (HT-high temperature). The deposition reactor used was different from the one used for the experiments described in Chapter 4, and the temperatures mentioned are nominal. The results indicate that in the narrow range of temperature investigated, higher substrate temperature (or lower hydrogen content) does not necessarily imply higher stabilized efficiency. This is in general agreement with the data presented in Section 4.

The experimental data have been complemented by theoretical calculations where we have used the a-Si:H solar cell model[8] to see if these results could be explained by appropriate changes in the fundamental properties of the material like density of localized states - N, carrier capture cross section - σ_s, and carrier mobilities. The device parameters were fitted such that the calculated J-V characteristics agreed with the measured ones. The shape of the density of states as well as the carrier capture cross sections responsible for recombination were assumed to be the same. The electron mobility μ_n of 15 cm^2/Vs was assumed to be identical for both cells. However, hole mobility μ_p was taken to be 4 cm^2/Vs for LT and 2 cm^2/Vs for HT samples to get a better fit with measured J-V characteristics.

Based on our calculated results, degradation in the device characteristics could be explained by an increase in the density of localized states alone. The LT sample had lower initial density of states N_0 than HT sample, but after 10^4 sec of low intensity illumination (LI~5 x AM1) or $\geq 10^2$ sec of high intensity (HI~50 x AM1) illumination, both cells reached saturation in FF's with corresponding N_{sat} values reported in literature. However, due to the higher hole mobilities, the final efficiency - η and FF's are higher for LT sample. The following Figs. 38 and 39 for LT and Figs. 40 and 41 for HT cells present the measured and calculated FF's. In Fig. 42 one can see the calculated increase in density of states N as a function of time under LI illumination.

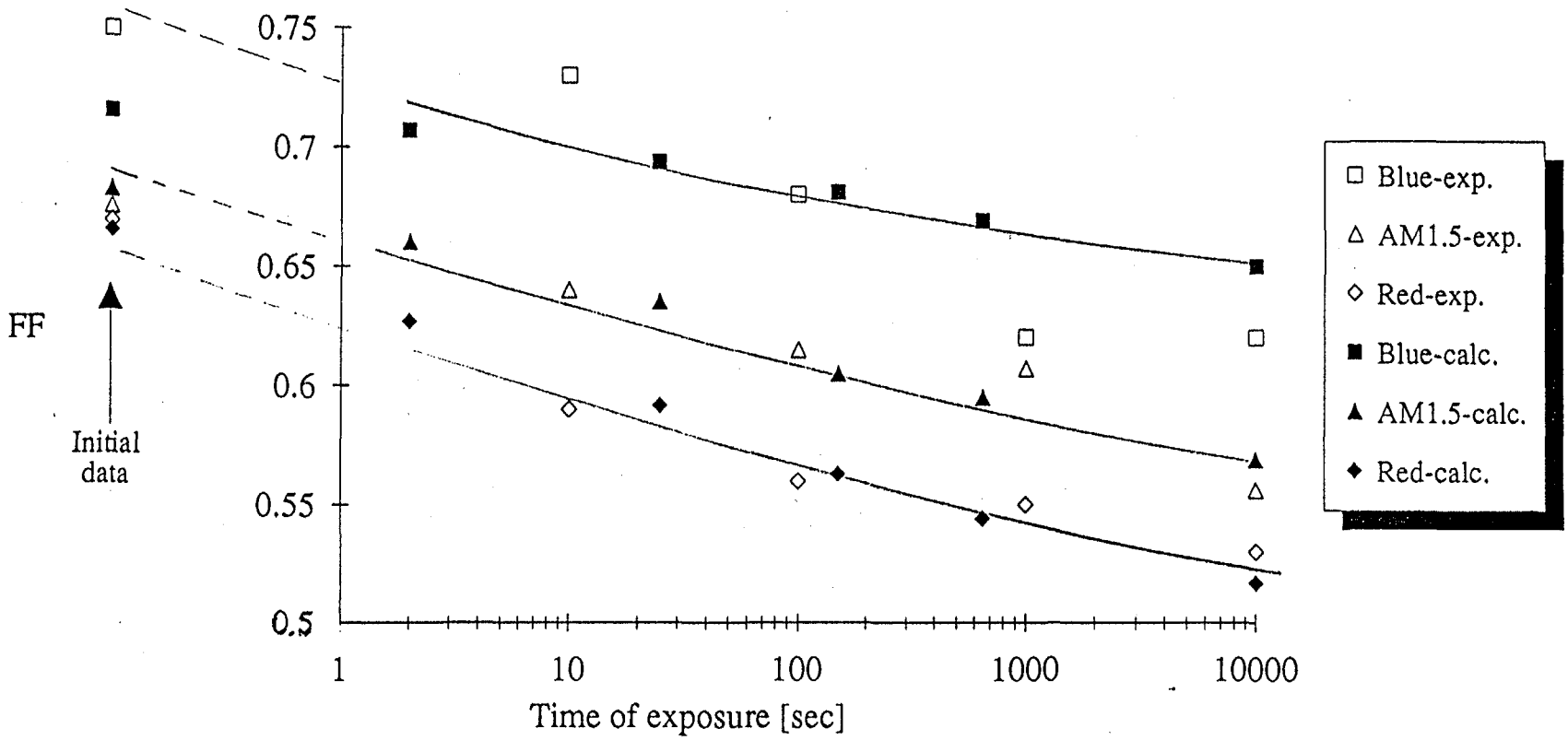

Fig. 38. Experimental and theoretical values of AM1.5, red, and blue FF as a function of exposure time for the LI case and LT sample.

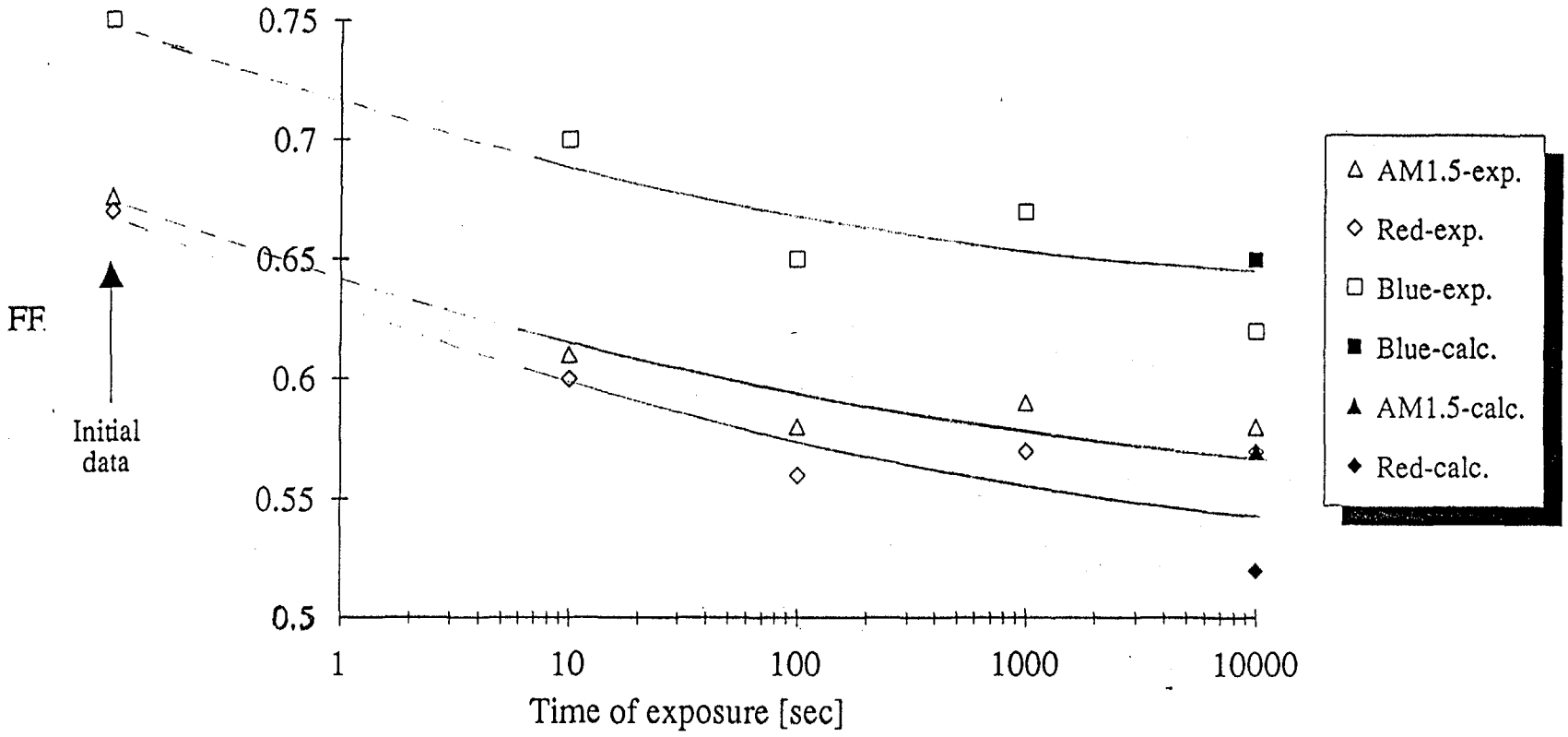

Fig. 39. Experimental and theoretical values of AM1.5, red, and blue FF as a function of exposure time for the HI case and LT sample.

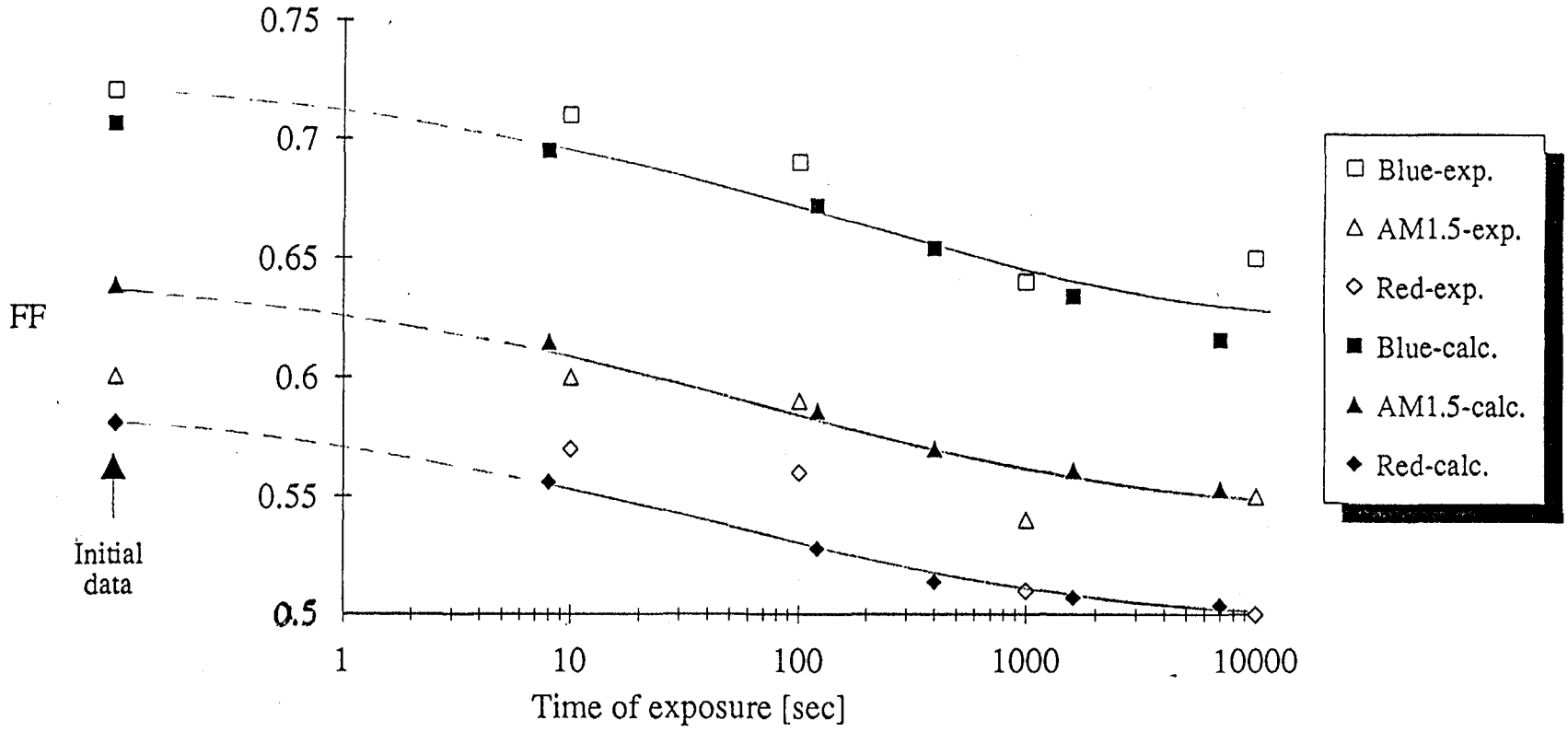

Fig. 40. Experimental and theoretical values of AM1.5, red, and blue FF as a function of exposure time for the LI case and HT sample.

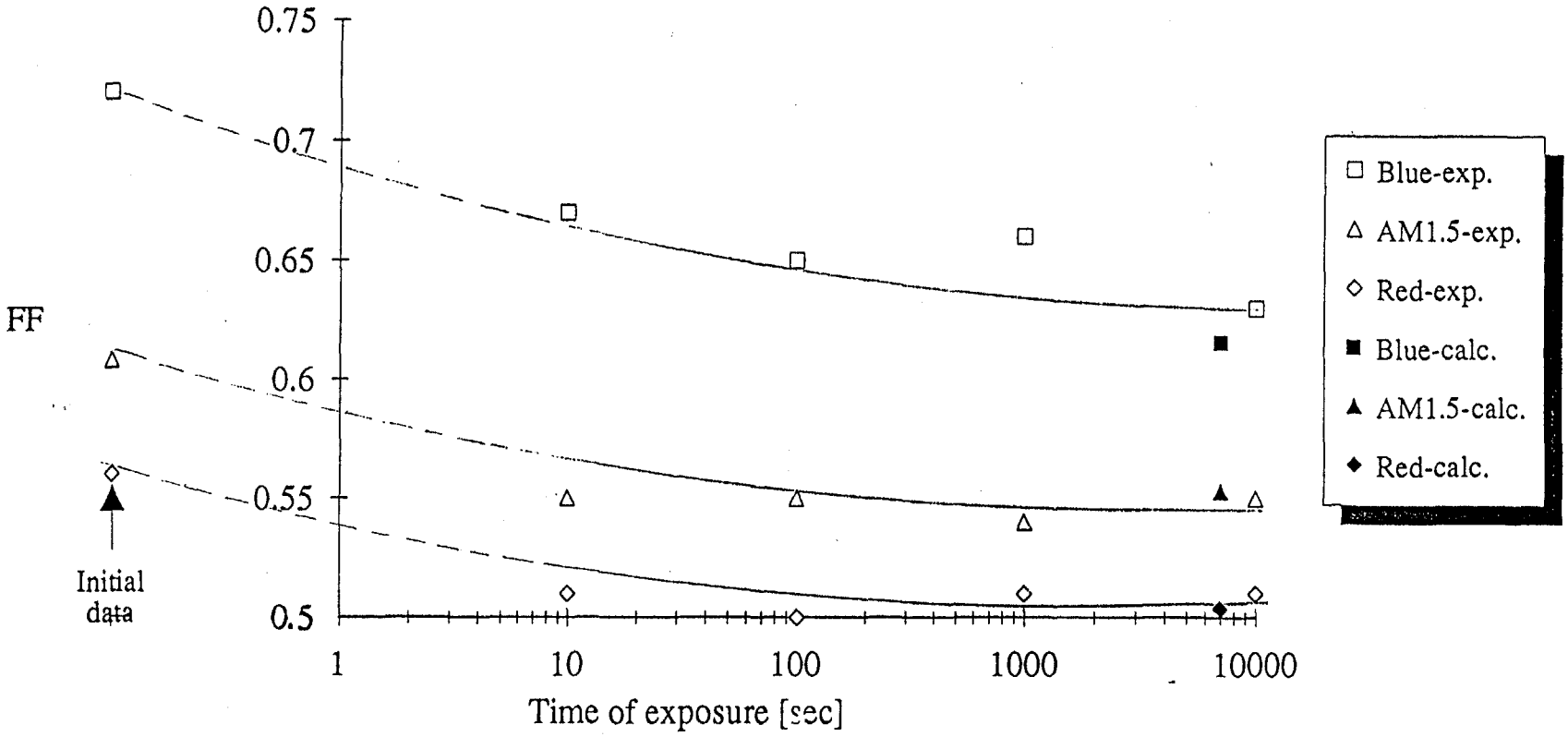

Fig. 41. Experimental and theoretical values of AM1.5, red, and blue FF as a function of exposure time for the HI case and HT sample.

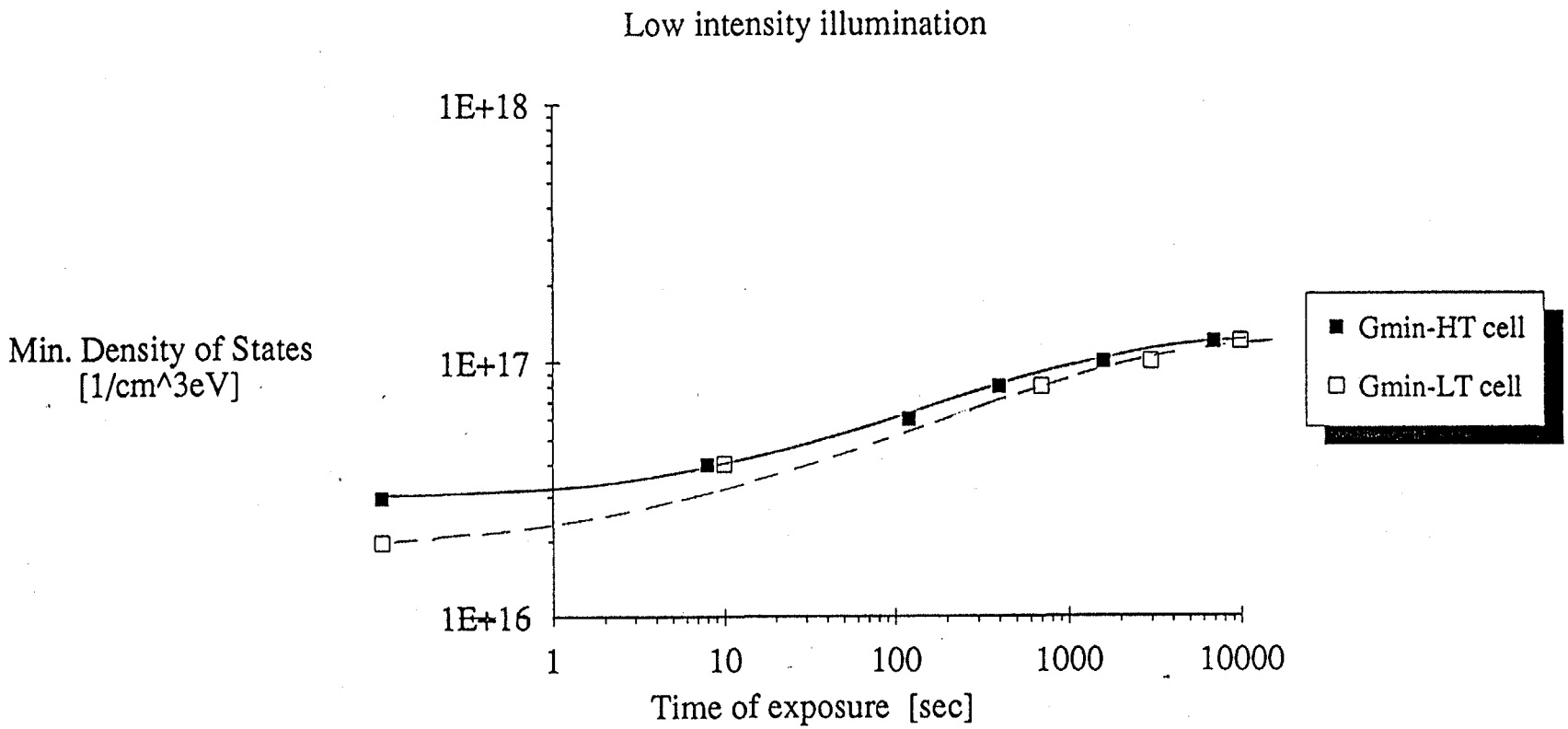

Fig. 42. Calculated minimum density of states as a function of light exposure for the two samples.

From the above study we see that both carriers suffer similarly due to the S-W degradation. The results not only elucidate that the dynamic changes in device transport properties could be represented by increase in the densities of states alone but also allowed us to use the saturation value of localized states N_{sat} for the optimized design of dual-junction solar cells with respect to the final efficiency rather than the initial efficiency.

5.2 Single-junction Cell Performance as a Function of Thickness in Undegraded and Degraded State

We have computed the performance of a-Si:H single-junction solar cell as a function of cell thickness both in undegraded and degraded state. The computed results showed the maximum stable efficiency to occur for cell thickness of about 1000 Å-1200 Å (cf. Fig. 43). Recently, experimental data have become available, and, as Fig. 44 shows, the efficiency of single-junction solar cell peaks for cells with 1700 Å of intrinsic silicon (20 minutes intrinsic deposition), which is in good agreement with the theoretical prediction. The original simulation assumed the same number of light reflections within the cell and the final saturation density of localized states to reach the same level of $g_{min} = 1.2 \times 10^{17}/cm^3$ eV, irrespective of cell thickness. The calculation was done for solar spectrum AM1.5.

Since the experimental data became available, we have recalculated J-V characteristics using two illumination spectra; one approximating solar AM1.5 and the other from incandescent lamp which has been used for accelerated testing (see Fig. 45). For the sake of convenience, we denote this spectrum as "red" due to the missing short wavelength component in it. The experimental J-V data used for this study was taken after 10^3 sec. of accelerated high-intensity red illumination (x 82) at 25°C. We might safely assume that cells reached saturation in degradation in view of the prevalent experimental data, which say that at this low temperature, a-Si samples reach saturation irrespectively of illumination intensity.

The measured initial and final J-V characteristics were obtained under low intensity red light after previously adjusting its intensity, such that the measured short-circuit currents of undegraded sample were approximately the same under AM1.5 and red spectra. Moreover, the intensity of the red spectrum used for J-V data acquisition was the same for undegraded and degraded cells at a given thickness.

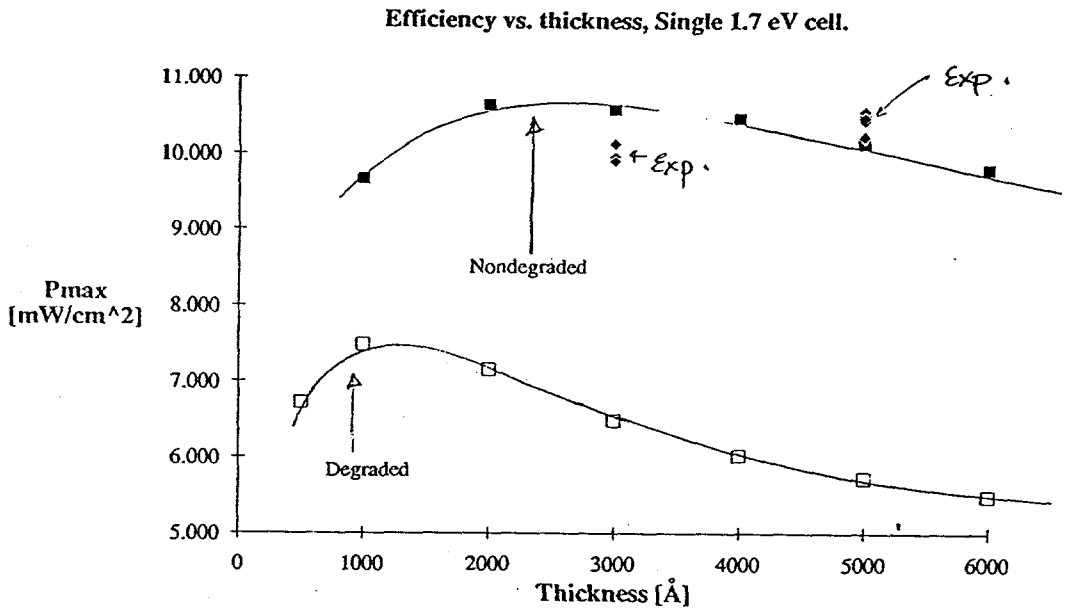

Fig. 43. Theoretically predicted results of maximum single-junction cell efficiency as a function of thickness in undegraded and degraded state.

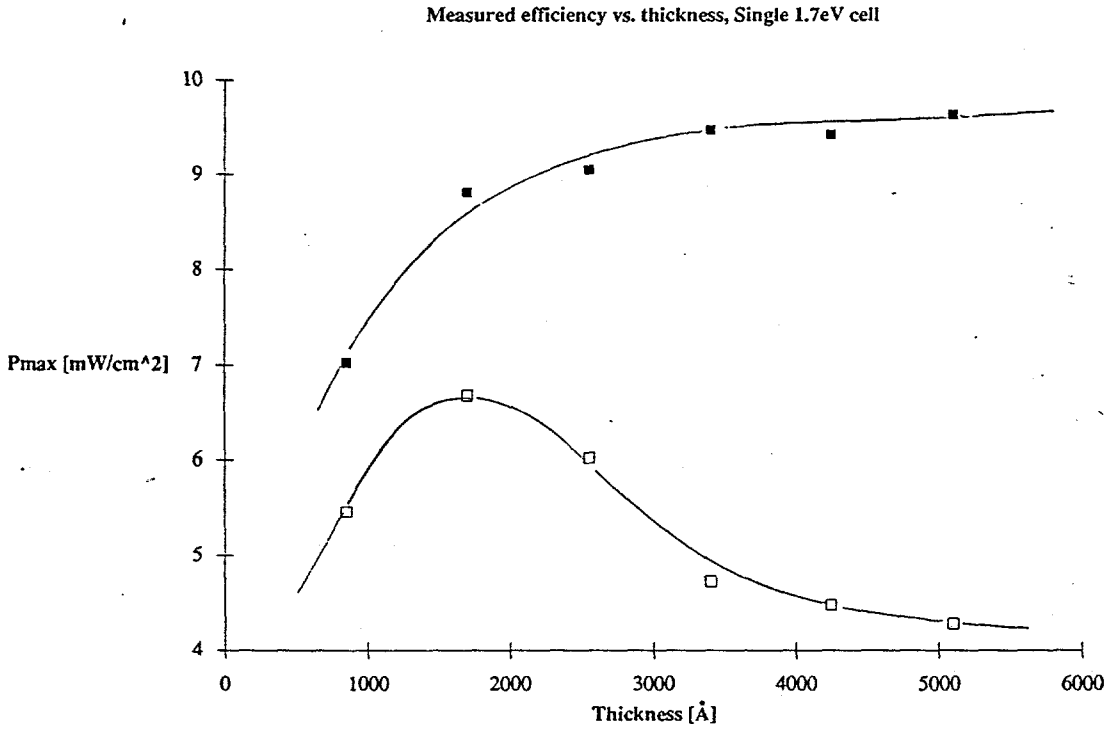

Fig. 44. Measured efficiency versus single-junction cell thickness before and after degradation.

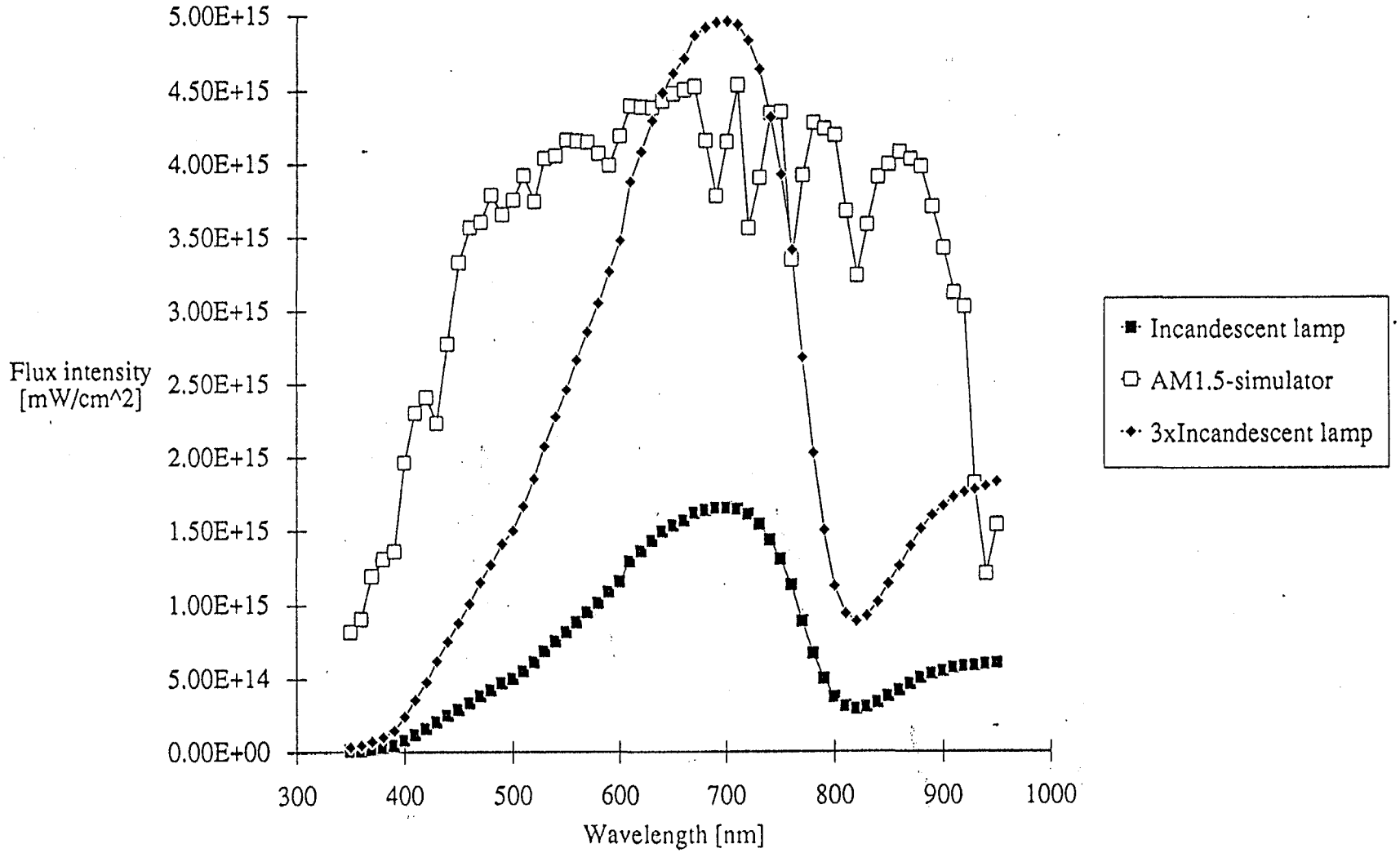

Fig. 45. Flux intensities of AM1.5 Xenon lamp's spectrum compared with "red" spectrum of incandescent lamp. 3xIncandescent lamp indicates the flux intensity amplified 3 times at every wavelength.

As far as calculations were concerned, we had to modify the number of reflections in order to get better fit of short-circuit currents with experimental data. Hence, for 10-minute deposition sample we assumed 1 reflection, for 20 minutes deposition 2 reflections, for 30 minutes deposition 3 reflections, and so forth. We also had to increase the saturated density of states in degraded samples from g_{sat} = 1.2 x $10^{17}/cm^3$ eV for thin cells (up to 30 min. deposition) to g_{sat} = 2 x $10^{17}/cm^3$ eV for thicker cells to account for the significant drop in efficiency above 3000 Å. Note that deposition rate for the *i* layers is ~ 85 Å/min. The electron band mobility μ_n was assumed to be 15 cm^2/Vs, and free hole mobility μ_p was assumed to be 1 cm^2/Vs regardless of device thickness. It was also assumed that the mobilities do not change upon light exposure. The other internal device parameters remained unchanged from that used for the calculations in the previous chapter.

Figure 46 shows the comparison between the measured and recalculated J_{sc} and P_{max} and Fig. 47 shows that for V_{oc} and FF in the single-junction, undegraded a-Si:H solar cell for different cell thicknesses. Similar comparison is presented for the fully degraded solar cell in Figs. 48 and 49. One can see higher performance by cells illuminated by AM1.5. This is due to the missing blue component in the red spectrum. Otherwise, the agreement is satisfactory enough to justify using this set of parameters for calculation of dual structure optimized for the most efficient stable efficiency.

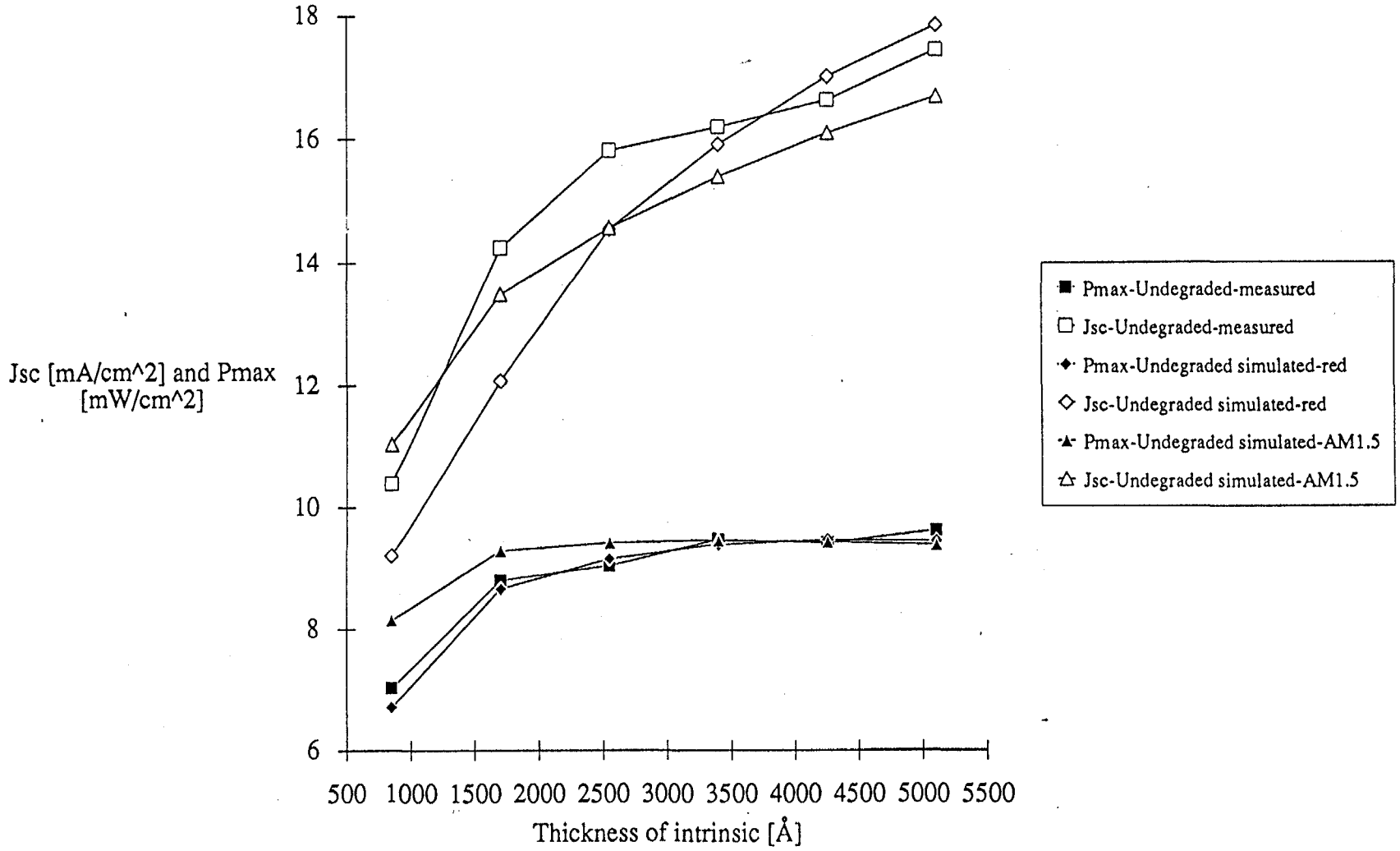

Fig. 46. Measured and calculated J_{sc} and P_{max} of single undegraded a-Si:H solar cell as a function of its thickness. Calculations were done for AM1.5 and amplified "red" spectra shown in Fig. 45.

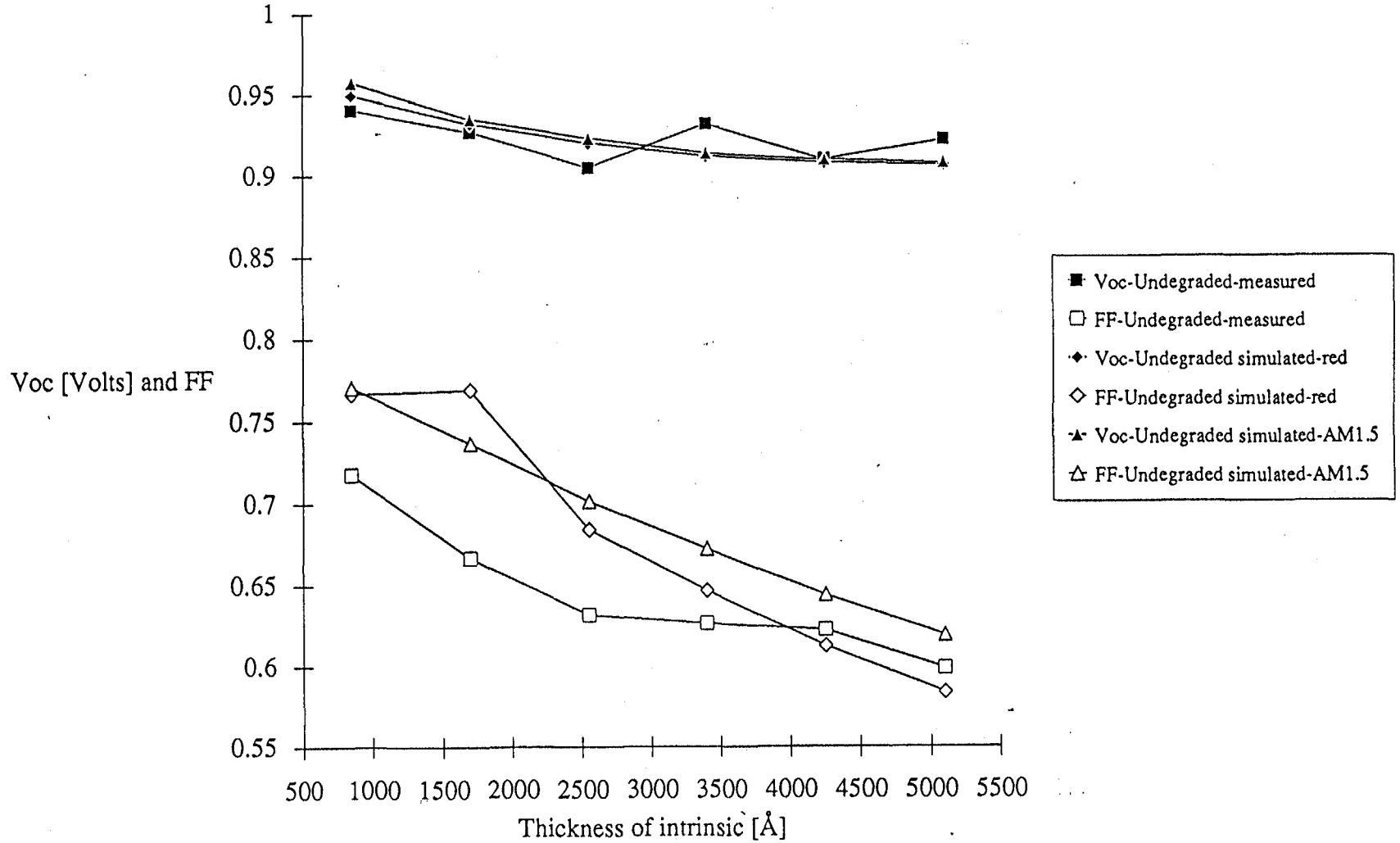

Fig. 47. Measured and calculated V_{oc} and FF of single-junction undegraded a-Si:H solar cell as a function of its thickness. Calculations were done for AM1.5 and amplified "red" spectra shown in Fig. 45.

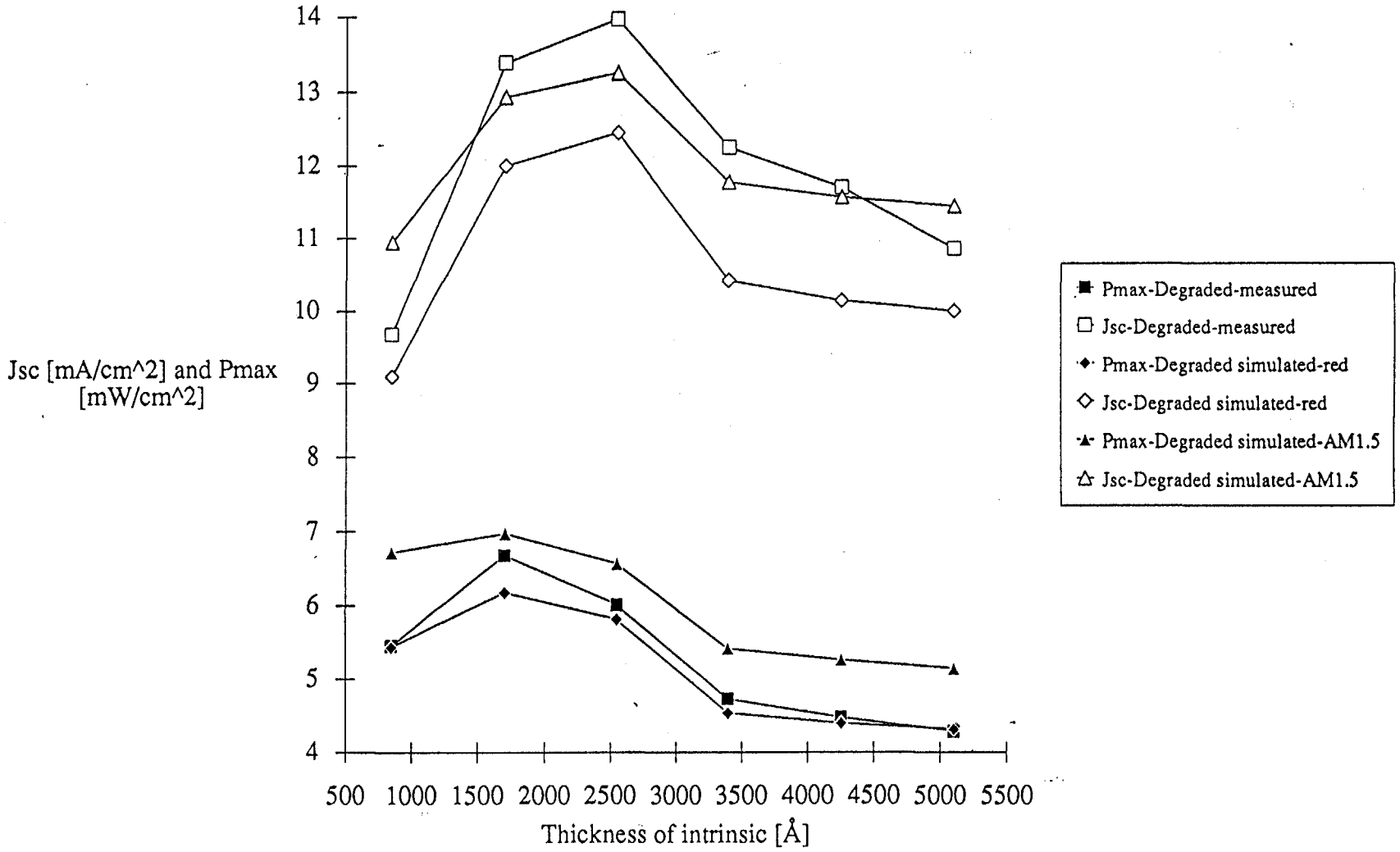

Fig. 48. Measured and calculated J_{sc} and P_{max} of single-junction degraded a-Si:H solar cell as a function of its thickness. Calculations were done for AM1.5 and amplfied "red" spectra shown in Fig. 45.

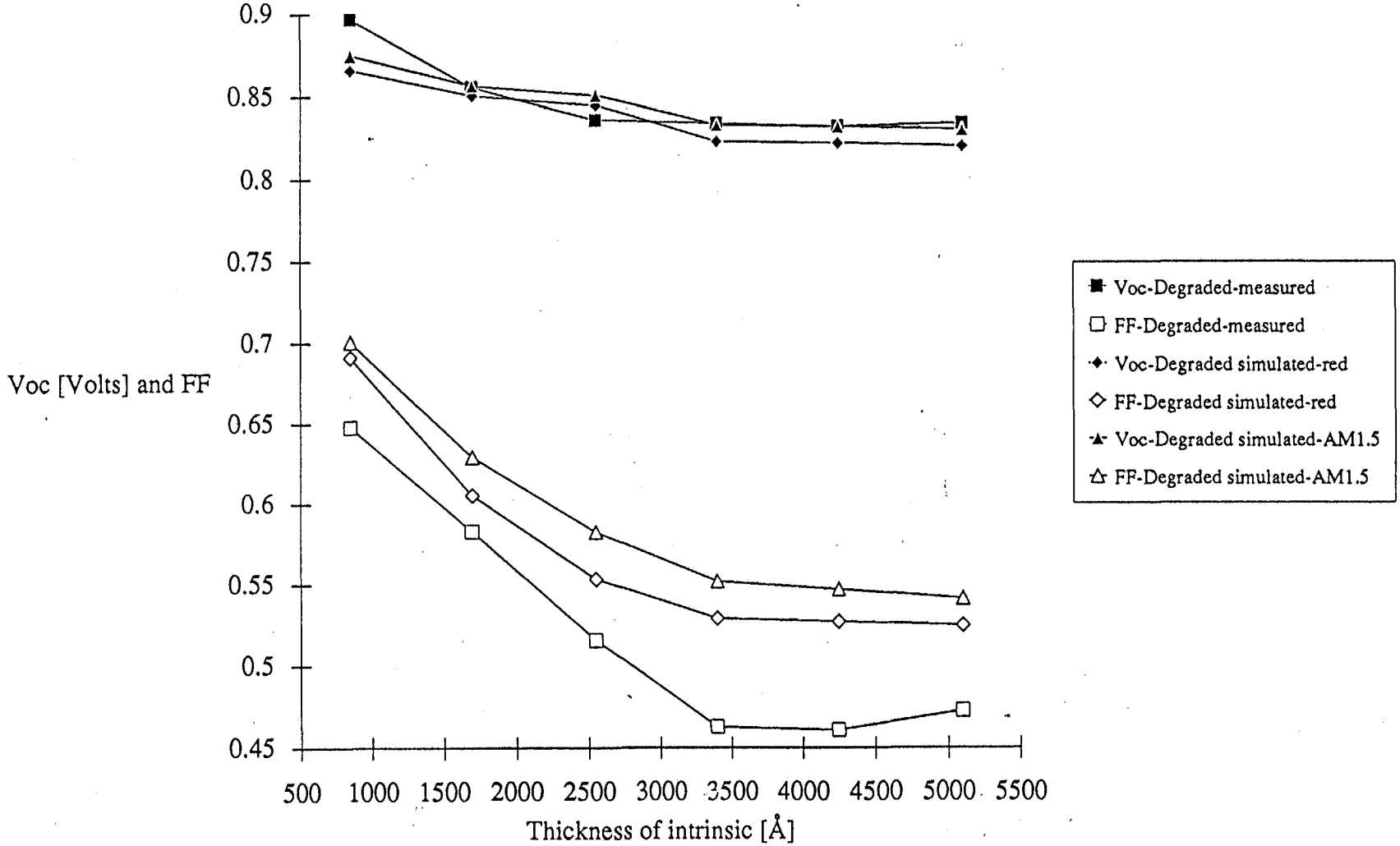

Fig. 49. Measured and calculated V_{oc} and FF of single-junction degraded a-Si:H solar cell as a function of its thickness. Calculations were done for AM1.5 and amplified "red" spectra shown in Fig. 45.

REFERENCES

1. SERI Annual Report (March 1987 - February 1988), Subcontract No. ZB-7-06003-4 (SERI/STR-211-3373).

2. A. Banerjee and S. Guha, J. Appl. Phys. 69, 1030 (1991).

3. SERI Semiannual Report (March - August 1988), Subcontract No. ZB-7-06003-4 (SERI/STR-211-3526).

4. H. R. Park, J. Z. Liu and S. Wagner, Appl. Phys. Lett. 55, 2658 (1989).

5. C. S. Hong and H. L. Hwang, J. Appl. Phys. 62, 1989 (1987).

6. Z. E. Smith, S. Wagner and B. W. Faughnam, Appl. Phys. Lett. 46, 1079 (1985).

7. A. Banerjee, S. Guha, A. Pawlikiewicz, D. Wolf and J. Yang, Int. Meeting. Stability of a-Si Materials and Solar Cells, Denver, Feb. 1991, AIP Conf. Proc. 234, to be published.

8. A. Pawlikiewicz and S. Guha, IEEE ED-37, 403 (1990).

Document Control Page	1. SERI Report No. SERI/TP-214-4453	2. NTIS Accession No. DE92001197	3. Recipient's Accession No.

4. Title and Subtitle

Research on Stable, High-Efficiency Amorphous Silicon Multijunction Modules

5. Publication Date

December 1991

6.

7. Author(s)

S. Guha

8. Performing Organization Rept. No.

9. Performing Organization Name and Address

United Solar Systems Corporation
1100 West Maple Road
Troy, Michigan 48084

10. Project/Task/Work Unit No.

PV141101

11. Contract (C) or Grant (G) No.

(C) ZM-1-19033-2

(G)

12. Sponsoring Organization Name and Address

National Renewable Energy Laboratory
1617 Cole Blvd.
Golden, Colorado 80401-3393

13. Type of Report & Period Covered

Technical Report

14.

15. Supplementary Notes

NREL Technical Monitor: W. Luft (303/231-1452)

16. Abstract (Limit: 200 words)

This report describes research to improve the understanding of amorphous silicon alloys and other relevant non-semiconductor materials for use in high-efficiency, large-area multijunction modules. The research produced an average subcell initial efficiency of 8.8% over a 1-ft^2 area using same-band-gap, dual-junction cells deposited over a ZnO/AlSi back reflector. An initial efficiency of 9.6% was achieved using a ZnO/Ag back reflector over smaller substrates. A sputtering machine will be built to deposit a ZnO/Ag back reflector over a 1-ft^2 area so that a higher efficiency can also be obtained on larger substrates. Calculations have been performed to optimize the grid pattern, bus bars, and cell interconnects on modules. With our present state of technology, we expect a difference of about 6% between the aperture-area and active-area efficiencies of modules. Preliminary experiments show a difference of about 8%. We can now predict the performance of single-junction cells after long-term light exposure at 50°C by exposing cells to short-term intense light at different temperatures. We find that single-junction cells deposited on a ZnO/Ag back reflector show the highest stabilized efficiency when the thickness of the intrinsic layers is about 2000 Å.

17. Document Analysis

a. Descriptors

photovoltaics ; multijunction modules ; high efficiency ; amorphous silicon ; solar cells

b. Identifiers/Open-Ended Terms

c. UC Categories

271

18. Availability Statement

National Technical Information Service
U.S. Department of Commerce
5285 Port Royal Road
Springfield, VA 22161

19. No. of Pages

85

20. Price

A05